N° nationale de Thèse : 2012ENSL0729

UNIVERSITÉ FRANCO ITALIENNE | UNIVERSITÀ ITALO FRANCESE

SCUOLA NORMALE SUPERIORE PISA

ENS DE LYON

Tesi
Corso di Perfezionamento in Chimica

Dipartimento di Chimica e Chimica Industriale

Thèse
École Doctorale de Chimie

Centre de Résonance Magnétique Nucléaire FRE 3008 CNRS/ENS Lyon/UCB Lyon 1

Titolo
Sviluppi metodologici per la cristallizzazione e l'analisi struttrale di proteine tramite Risonanza Magnetica Nucleare alle stato solido

Titre
Développements méthodologiques pour la cristallisation et l'analyse structurale de protéines par Résonance Magnétique Nucléaire en phase solide

Presentata e sostenuta pubblicamente il

Présentée et soutenue publiquement le

12/07/2012

Candidato

Candidat

Alessandro MARCHETTI

Correlatori
Prof. C. A. VERACINI

/

Co-Directeurs
Dr. G. PINTACUDA
Prof. L. EMSLEY

Sentito l'avviso di:

Après avis de :

Prof. H. OSCHKINAT
Prof. P. J. GRANDINETTI

Davanti alla commissione esaminatrice composta di:
Prof. C. A. VERACINI
Prof. A. FERRARA
Prof. H. OSCHKINAT

Devant la comission d'examen formée de :
Dr. G. PINTACUDA
Prof. L. EMSLEY
Prof. P. J. GRANDINETTI

vita brevis,

ars longa,

occasio praeceps,

experimentum periculosum,

iudicium difficile

Acknowledgments

No man is an island. I really wanted to write these acknowledgments personally to all of you to express my gratitude, but time is tyrant and forgive me if the only thing I can do is make a simple list. I will just say during this fascinating four years of stage and Ph.D in Lyon and in Pisa, I was given the opportunity to collaborate with excellent scientists and to meet numerous interesting people who supported me with their advice, knowledge, and friendship, creating during this period a friendly and motivating environment. Among all of these people, I would like to acknowledge particularly:

- Prof. Carlo Alberto Veracini, the Italian supervisor, for his great flexibility and human kindness; this cotutorship agreement has been possible primarily thanks to him;

- Dr Guido Pintacuda and Prof. Lyndon Emsley, the French supervisors, for providing excellent research conditions, for teaching me how to think thoroughly about scientific problems, for their inspiring guidance in many discussions, and for their precious advices in different circumstances. Thanks to their worlds but mainly thanks to their actions I have understood what is the true meaning of making research in an international environment;

- Dr Valentina Domenici, Dr Stefan Jehle, Dr Moreno Lelli, Dr. Józef Lewandowski, Prof José Antonio Marquez (in rigorous alphabetical order), because everything I know about liquid crystalline mesophases, biological solid-state NMR, solid-state NMR hardware, protein dynamics and crystallogenesis come from them; I thank them for their constant support and for answering kindly all my questions,

- the people in Lyon I have shared my cubicle with during all these years: Julien Sein, Clément Pointezau, Michele Felletti and Élodie Jobard; let me tell you, you were the best.

- all the past and present members of the group of Prof. Emsley for their availability and for creating a very stimulating and friendly atmosphere: Dr Élodie Salager, Dr Amy Louise Webber (and Alphie), Dr Paul Guery, Dr. Andrew J. Pell, Dr Gwendal Kervern, Dr. Laetitia Shintu, Dr Meghan Halse, Dr Aron Rossini, Dr Ségoléne Laage, Dr Marc Dumas, Dr Benjamin Blaise, Dr. Céline Domange, Dr Bénédicte Elena, Dr. Torsten Hermann, Dr Isak Shaik, Dr Jean-Nicolas Dumez, Emeline Barbet-Massin, Dr. Vincent Navratil.

- all the other past and present members of the group of Prof. Veracini: Dr Mario Cifelli and Sara Dolci and Dr Alberto Marini, may he rest in peace.
- all co-authors who I haven't already mentioned for these interesting collaborations;
- the Italian secretaries Elisabetta Terzuoli and Mario Landucci, together with the French secretaries Catherine Bernard, Valérie Fromentéze and Audrey Marchetti for their help with the administrative charges.
- the *Università Italo-francese* (*Università Franco-Italienne*) for its cotutorship mobility grant (Vinci 2009 - chapiter II) and Pascale Zaffina of the Bureau Scientifique of the French Embassy in Rome and Cécile Savoldelli (EGIDE - Délégation Régionale Rhône-Alpes) for the three months *Cycle III et cotutelle bourse d'Étude* in 2009.
- my *alma mater*, the Scuola Normale Superiore, for the financial support over the years.
- more in general, all my friends around the world, that have also provided critical reading of the manuscriptm for their useful suggestions. Giacomo, Samuele, Alessandro, Teresa... I wil always be there for you all.
- the referees that have corrected this manuscript, Prof. Oschkinat and Prof. Grandinetti, for the time they have spent reading it, despite their busy daily schedule. It is a big satisfaction to interact with people of such great expertise.
- Prof. Vincenzo Barone, as head of the Ph.D. programme in Chemistry at the Scuola Normale, for his great flexibilty over the years, that have made my life easier. I truly admire his pragmatism.
- my family, who was there everytime I needed it;

In summary, I wish to thank everyone who helped me complete this dissertation. Without your continued efforts and support, I would have not been able to bring my work to a successful completion. And, especially to all of you I will never see anymore, I wish you good luck with your lives.

Introduction

Bureaucratic Requirements

Cotutorship agreement

This Thesis fulfills the requirements requested by paragraph 2.3 of the cotutorship agreement and its following integration in the framework of paragraph 4.1 of the same agreement, both signed by the student, the cosupervisors and the Directors of the related Institutions in May 2009 and in May 2012, respectively.

Università Italo Francese / Université Franco Italienne

This Thesis fulfills the requirements requested by paragraphs 3 and 4 of the regulations of the *Bando Vinci 2009* of the *Università Italo Francese/Université Franco italienne*. Additional documents required for the validation of the granting will be sent to the secretariat together with the paper copy of this Thesis.

Software specifications

- **Operative systems** this thesis has been written on a **MAC OS** X Version 10.6.8;
- **Editing** this Thesis manuscript has been compiled with LaTeX using **TeXworks 2011** for MAC OS;
- **bibligraphy** the bibliography of this Thesis manuscript has been organized with **Mendeley Desktop** version 1.5.2
- **spectra** the spectra presented in Thesis manuscript have been created using **Bruker Topspin** version 3.1 and **Sparky** on **XQuartz** version 2.3.6
- **Images** the images reported on this Thesis manuscript have been produced using Adobe Illustrator CS3 (output formats: `jpg`, `png` and `pdf`);
- **images of protein structure** the images of protein strcutures reported in this Thesis have been produced using **UCSF Chimera**, production version 1.4.1.

English Summary

High-resolution solid-state NMR (ssNMR) has recently emerged as a powerful characterization technique for systems that cannot be investigated by solution NMR or X-ray crystallographic methods, and represents a subtle complementary technique for any atomic-scaled study. This is particularly true in structural biology. There exist nowadays well established protocols for sample preparation, resonance assignment and collection of structural restraints, that have paved the way to the first three-dimensional structure determinations at atomic resolution of biomolecules in the solid state, from microcrystalline samples to fibrils and membrane-associated systems.

Despite rapid uptake in the field of structural biology, however, these methods for structure determination are far from being routine, and several important problems remain however to be solved before ssNMR is applied to the study of challenging solid protein assemblies. Many methodological developments are still expected in this fast evolving field.

Most of the model systems used up-to-date for method development in biological solid-state NMR, are relatively small globular proteins, in the range of 50 to 80 residues (approximately 5.5 to 9.5 kDa). In order to extend the capabilities of ssNMR to larger substrates, the objectives of this thesis are twofold: a) to establish a new, large and more complex model system, and b) to develop new, sophisticated NMR experiments in order to improve the sensitivity and the resolution of the currently existing schemes for resonance assignment, which is one of the main barrier to progress to structural investigation in solid proteins.

The N-terminal domain of the ϵ subunit of *E. coli* DNA polymerase III (ϵ_{186}: 186 residues, 18 kDa) was selected as a target. This domain represents the catalytic core of the *E. coli* replisome, the large molecular machine that replicated DNA in bacteria.

In a first part, preparation conditions for solid-state NMR are obtained, notably in combination with automated screening processes for high-throughput protein crystallography, and almost complete resonance assignment is performed by the application of established experiments based on high-power rf irradiations and slow magic-angle spinning (MAS) at high magnetic fields.

In a second part, we explore the use of MAS at so-called ultra-fast spinning rates (60 kHz). We show that this makes possible the use of "totally low power" experiments. This yields an extraordinary increase in resolution and sensitivity, enabling the acquisition of selective cross-polarization (CP) transfers, through-bond correlations and ^{1}H-detected correlations. In particular, we demonstrate that narrow ^{1}H NMR line widths can be obtained for fully protonated protein samples in the solid state under ultra-fast magic-angle spinning for medium-size microcrystalline and non-crystalline proteins, without any need for dilution against a deuterated background. This provides extensive, robust and expeditious assignments of the backbone ^{1}H, ^{15}N, ^{13}Cα and ^{13}CO resonances of proteins in different aggregation states, without the need of deuteration.

The final part of this thesis concerns the study of thermotropic liquid crystals (LC or LX) phases of a de Vries smectogen, the (S)-hexyl-lactate derivative abbreviated as 9HL, selectively

deuterated in a phenyl moiety of the aromatic core. de Vries mesophases show a substantially constant layer spacing in the transition between smectic C and smectic A mesophases and are for this reason of great interest for the development of new ferroelectric (FLC) and antiferroelectric (AFLC) electrooptic devices. Our work is the first attempt to apply NMR to characterize the nature of the de Vries transition, discriminating among possible models. It is also one of the first examples in the scientific literature of application of high magnetic field (above 16 T) for the analysis of LX phases.

Keywords

NMR	*ultra-fast MAS, high field, proton detection, model systems*
HT-X	*crystallogenesis, high-throughput protein crystallization techniques*
Polymerase	*DNA polymerase III*
Liquid crystals	*smectic order, orientational distribution, de Vries smectogens*

Riassunto in Italiano

La risonanza magnetica nucleare allo stato solido (ssNMR) ad alta risoluzione è recentemente emersa come una potente tecnica di caratterizzazione per sistemi che non possono essere indagati tramite NMR in soluzione o metodi cristallografici a raggi X, e rappresenta una tecnica complementare di precisione per ogni studio di livello atomico. Questo fatto è particolarmente vero nel settore della biologia strutturale. Esistono oggigiorno protocolli ben consolidati per la preparazione di campioni, l'attribuzione delle risonanze e l'acquisizione di vincoli strutturali, che hanno aperto la via alla prime caratterizzazioni strutturali a livello atomico di biomolecole allo stato solido, da proteine microcristalline, alle fibrille a alle proteine di membrana. Nonostante la loro rapida adozione nel campo della biologia strutturale, questi metodi di determinazione strutturale sono ben lontani dall'essere routinari e molti problemi importanti rimangono da essere risolti prima che le tecniche ssNMR siano applicate allo studio di impegnativi compessi di proteine. Molti sviluppi metodologici sono ancora attesi in questo campo in forte evoluzione.

La maggioranza dei sistemi modelli impiegati allo stato attuale per lo sviluppo metodologico nell'NMR in stato solido sono proteine globulari relativamente piccole, che spaziano nel range dai 50 agli 80 residui (approsimativamente dai 5.5 ai 9.5 kDa). Al fine di estendere le potenzialità della ssNMR a substrati più grandi, questa tesi si pone due obiettivi: a) stabilire un nuovo sistema modello di grandi dimensioni e b) sviluppare nuovi e più sofisticati esperimenti NMR al fine di migliorare la sensibilità e la risoluzione degli attuali metodi per l'attribuzione di risonanze, una delle barriere principali al progresso dell'analisi di proteine in stato solido.

Il dominio N-terminale della subunità ϵ della DNA polymerase III di *E. coli* (ϵ_{186}: 186 residues, 18 kDa) è stato selezionato come target. Questo dominio rappresenta il nucleo catalitico del replisoma di *E. coli*, il grande macchinario molecolare che replica il DNA nei batteri. In primo luogo, sono state ottenute condizioni di preparazione per NMR in stato solido, specialmente in combinazione con processi automatici di *screening* ad alto rendimento per cristallografia di proteine, e un'attribuzione quasi completa del sistema di risonanze è stata ottenuta tramite l'applicazione di esperimenti basati su irraggiamento di rf ad alta potenza e basse frequenze di rotazione all'angolo magico (MAS) ad alti campi magnetici.

In secondo luogo, abbiamo esplorato l'utilizzo del MAS alla cosidetta alta frequenza (60 kHz). Abbiamo mostrato come sia possibile l'utilizzo di esperimenti a potenze "totalmente basse". Ciò comporta uno straordinario aumento in risoluzione e sensibilità, permettendo l'acquisizione di trasferimenti di polarizzazione selettivi, di correlazioni scalari attraverso i legami e di correlazioni acquisite al ^{1}H. In particolare, abbiamo dimostrato che larghezze di linea ^{1}H NMR sottili possono essere ottenute per campioni proteici interamente protonati allo stato solido sotto rotazioni ultrarapide all'angolo magico per prtoteine microcristalline e non-cristalline di media dimensione, senza alcuna necessità di diluizione in un ambiente deuterato. Questo permette un'assegnazione robusta e rapida delle risonanze ^{1}H, ^{15}N, ^{13}Cα e ^{13}CO della catena principale delle proteine in diversi stati di aggregazione senza ricorrere alla deuterazione.

La parte finale di questa tesi riguarda lo studio di fasi termotropiche liquido-cristalline (LC or

LX) di uno smettogeno de Vries, il derivato dell' (S)-esil-lattato abbreviato come 9HL, selettivamente deuterato in una porzione fenilica del *core* aromatico. Le mesofasi de Vries mostrano una distanza costante fra i piani nella transizione fra mesofase smettica C e smettica A e per questa ragione sono di grande interesse per lo sviluppo di nuovi apparecchi elettrottici ferroelectrici (FLC) e antiferroelectrici (AFLC). Il nostro lavoro rappresenta il primo tentativo di applicare la NMR per caratterizzare la natura delle transizioni de Vries discriminando fra i modelli possibili. È anche uno dei primi esempi nella letteratura scientifica di applicazione di alti campi magnetici (sopra i 16 T) per l'analisi di fasi liquido-cristalline.

Parole Chiave

RMN	*MAS ultra-rapido, alti campi, acquisizione al protone, sistemi modello*
HT-X	*cristallogenesi, tecniche di cristallizzazione di proteine ad alta efficienza*
Polymerase	*DNA polimerasi III*
Liquid crystals	*ordine smettico, distribuzione orientazionale, smettogeni de Vries*

Resumé en français

La RMN du solide à haute résolution (ssNMR) est récemment apparue comme une technique puissante de caractérisation des systèmes ne pouvant pas être étudiés par RMN du liquide ou par des méthodes cristallographiques aux rayons X. De pus, elle représente une technique complémentaire de haute précision pour toutes études de la matière à l'échelle atomique, de qui est particulièrement intéressant dans le domaine de la biologie structurale.

De nos jours des protocoles bien établies existent pour la préparation des échantillons, pour l'attribution de résonances ainsi que pour la determination des contraintes structurelles, ce qui a ouvert la voie aux premières déterminations de structures tridimensionnelles de biomolécules à l'état solide avec une résolution atomique pour des échantillons microcristallins ainsi que des fibrilles et des systèmes associés aux membranes cellulaires.

Malgré la diffusion rapide de cette méthode dans le domaine des biomolécules, ces applications sont loin d'être systématiques, et plusieurs problèmes importants restent cependant à résoudre avant que la RMN du solide soit prête à faire face à des applications complexes, comme l'assemblages des protéiques solides. Ainsi des nombreux développements méthodologiques sont encore attendus dans ce domaine en plein essort.

La plupart des systèmes modèles utilisés de nos jours pour le développement de méthodes RMN à l'état solide appliquées dans le domaine de la biologie correspondent à des protéines globulaires relativement petites, allant de 50 à 80 résidus (approximativement de 5.5 à 9.5 kDa). Afin d'étendre les capacités de la RMN en phase solide à des substrats plus grands, les objectifs de cette thèse sont de deux ordres: a) établir un nouveau système modèle, plus complexe et de plus grande dimension et b) développer de nouvelles expériences de RMN sophistiquées afin d'améliorer la sensibilité et la résolution des méthodes actuellement existantes pour l'attribution de résonances, une des principales limites au progrès de la caractérisation structurelle des protéines à l'état solide. Le domaine N-terminale de la ϵ, sous-unité de l'ADN polymérase III de *E. coli* (ϵ_{186}: 186 résidus, 18 kDa), a été choisi comme système cible. Ce domaine représente le cœur du domaine catalytique du réplisome, la grande machine moléculaire qui réplique l'ADN dans les bactéries.

Dans une première partie, les conditions de préparation de l'échantillon pour la RMN à l'état solide sont obtenus, notamment grâce aux processus de screening automatisés pour la cristallographie des protéines à haut débit, et l'attribution quasi exhaustive des résonances est effectuée par l'application des expériences bien établies basées sur les irradiations rf à haute puissance et sur la rotation à l'angle magique (MAS) à basse fréquence à hauts champs.

Dans une deuxième partie, nous étudions l'utilisation de vitesses à l'angle magique MAS "ultra-rapides" (60 kHz). Nous montrons que cela rend possible l'usage d'expériences aux puissances" completement faibles" affichant une augmentation extraordinaire de résolution et sensibilité, et permettant l'acquisition des transferts par polarisation croisée (CP), des corrélations entre les liaisons chimiques et des corrélations detectées par ^{1}H. En particulier, nous démontrons que des faibles largeurs de pics sur le spectres proton peuvent être obtenues pour des échantillons

de protéines microcristalline et non-cristallines entièrement protonée et de dimension moyennes à l'état solide, sous rotation ultra-rapide à l'angle magique, sans qu'une dilution dans un milieu deutéré soi nécessaire. Ainsi nous avons attribués, d'une façon robuste et rapide, les resonances ^{1}H ^{15}N, ^{13}Cα et ^{13}CO de la squelette des protéines dans différents états d'agrégation sans avoir recours a la deutération.

La dernière partie de cette thèse concerne l'étude de phases cristaux liquides thermotropes (LC ou LX) d'un smectogèn de Vries, le dérivé (S)-hexyl-lactate, abrégé 9HL, sélectivement deutéré dans un groupement phényle du noyau aromatique. Les mésophases de Vries sont organisées en couches d'espacement constant pendant la transition entre les mésophases smectique C et smectique A et sont pour cette raison d'un grand intérê t pour le développement de nouveaux appareils électrooptiques ferroélectriques (FLC) et antiferroélectrique (AFLC). Nos travaux répresentent la première tentative d'appliquer la RMN à la caractérisation de la transition de Vries et pour en différencier les modèles possibles. Il est également l'un des premiers exemples répertoriés dans la littérature scientifique de application d'un très haut champ magnétique (supérieur à 16 T) pour l'analyse des phases LX.

Mot-clés

NMR	*MAS ultra-rapides, hauts champs, détection au proton*
HT-X	*cristallogenèse, techniques de cristallographie des protéines à haut débit*
Polymerase	*ADN polymérase III*
Liquid crystals	*ordre smectique, distribution orientationelle, smectogènes de Vries*

Contents

Part I

Sample preparation and resonance assignment in biomolecular NMR

Chapter 1

Solid-state NMR in structural biology

1.1 Structural biology

Structural biology is the study of three-dimensional structures of molecules. A molecule cannot perform its function unless it can adopt its native structure and, along this principle, life is thus based on the ability of molecules to adopt their structure correctly. Of all types of molecules, proteins are the most elusive in doing just this. In his Nobel Lecture of 1972 Christian Anfinsen described how he came to the conclusion that all information a protein needs to fold into its native conformation lies within the amino acid sequence of this protein, a rule which is often called Anfinsen's dogma (also called the thermodynamic hypothesis, from his research on the folding of ribonuclease A) [1]. Around the same time, Cyrus Levinthal came to the conclusion that a protein could not possibly sample all possible conformations before finding its native folded state, as this would take longer than the present age of the universe [2], the so-called Levinthal paradox. The two findings combined suggested that protein folding must be a directed process. While extensive research has now led to a better understanding of protein folding, we are still not able to predict a protein structure from its sequence only. Thus, we still depend on experimental methods to obtain detailed models of protein structures.

Today, we know that most physiological processes involve the interaction of molecules within functional modules on different spatial and temporal scales. Increasingly accurate maps based on genetic, physical, and functional interaction data have revealed a higher level of molecular organization in which different molecular players and their spatiotemporal interactions are critical to biological functioning. The ability of biophysical techniques to determine conformations of individual molecules has greatly influenced our current view of reciprocal interactions among them, disclosing many aspects of chemical and biological processes (for example enzymatic function) as well as how to combat diseases related to their failure.

1.2 Techniques for structural determinations

Advances in structural biology (and more in general to our current view of chemical and biological processes in living beings) have been strongly supported by the success of two leading techniques: X-ray crystallography and solution NMR spectroscopy, which, until some years ago, were the only available experimental methods capable of producing high resolution protein structures within a limited timeframe. Both techniques have produced many thousands of protein and nucleic acid structures collected in the Protein Data Bank (www.pdb.org) which now (May 2012) contains 81750 entries. A third technique, electron microscopy (EM), is theoretically able to produce images on atomic scale, but, as protein specimens scatter relatively weakly and are sensitive to electronic beam damage, its resolution limit is modest.

The typical workflow leading to the determination of a protein structure from its sequence is sketched in figure 1.1, and is reviewed in the following paragraphs.

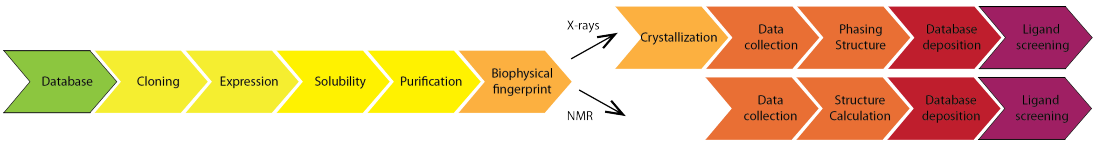

Figure 1.1: Protein structural determination workflow. A final step of ligand-screening, quite common in the pharmaceutical research, is also shown.

1.2.1 Protein production and purification

Protein production and purification are both non-deterministic steps and for each new target a successful procedure must be established by trial and error. The strategy adopted for cloning and expression depends on the donor organism, the available expression systems, and the number of targets. The choice of the system of expression host is a key question to be addressed. *E. coli* is the preferred one for the expression of recombinant protein, but many other systems (*S. cerevisiae* and *P. pastoris*, baculovirus/insect cell systems) have been explored for high-throughput approaches, which allow many samples to be processed in parallel [3]. The main goal is to overcome the poor yield and solubility problem that are commonly encountered since, based on data from the public structural genomics initiatives, 60-70 % of all targets of structural genomic projects fail to yield purified, soluble proteins; prokaryotic target proteins, for example, have a success rate of only approximately 30 % [4]. To improve the likelihood of expressing a target solubly and at acceptable levels, environmental parameters such as temperature, strain and mode of induction can be assayed and additionally, genetically encoded parameters such as vectors, tags for affinity chromatography (such as the hexa-histidine, glutathione S-transferase or maltose-binding protein) that can also increase the solubility [5], promoter and construct can be varied. Many projects invest a large amount of effort in designing multiple construct of a target gene using sequence alignment and bioinformatics tools, followed by PCR-based cloning and expression testing.

1.2.2 Protein X-ray crystallography

Since the beginning, determining X-ray structures has evolved into a highly specialized field and has become easier, faster and more automated (structures can now often be solved within a few hours), while the initial crystallisation step has remained a time consuming and erratic process, the most serious bottleneck in high-throughput protein-structure determination by diffraction methods. Most protein crystals obtained in early days of protein crystallography had been grown serendipitously by leaving a concentrated protein solution on the shelf or in the refrigerator. Today, despite advances in biomacromolecules crystallisation methodologies and the development of essential tools and reagents aiding crystal formation, it is still commonly accepted that all proteins behave individually and differ in their optimal crystallization conditions, which are found by sheer luck or with very tedious and time consuming procedures. *De novo* conditions for crystal growth for biological macromolecules are unpredictable: before the real crystallization experiments are performed and analyzed it is not possible to known the optimal factors under which any given protein will reliably produce suitable large, defect free and diffractable crystals. As a consequence of this fact, only 35% of purified proteins form objects resembling crystals and only 12% of sufficient quality to undergo X-ray analysis, most of them after a time-consuming refinement.

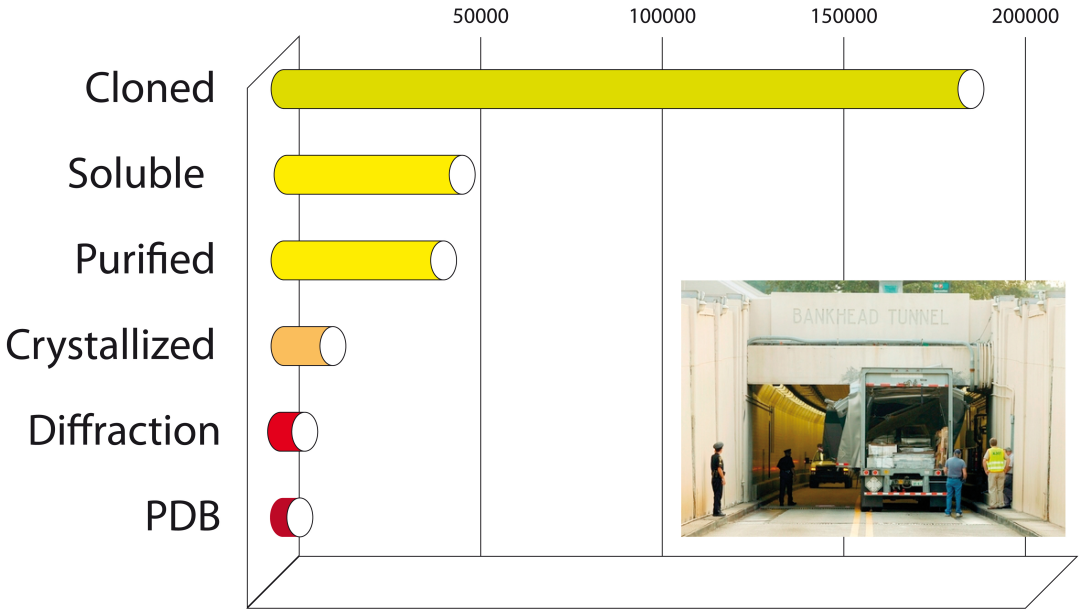

Figure 1.2: Major bottlenecks, i.e. rate- and throughput-limiting steps, in protein X-ray crystallography.

Existing guidelines for crystallizing proteins generally require substantial amount of protein and laboratory resources and that the protein crystallization process is still empirical, involving the challenging screening of a large number of crystallization conditions in a huge space of parameters (trial-and-error approach), and thus making the individual experience and know-how of the researcher the biggest factor in the ability to successfully produce protein crystals.

Given these difficulties it is understandable that structural biologists eagerly await any effort aimed to develop strategies to increase the success rate of protein crystallization.

Basically, the production of high diffractive crystallization crystals can be divided in two logical steps: screening of initial conditions and production of diffraction-quality single crystals (scaling-up).

Although published reports dealing with crystallization of specific proteins usually mention little or nothing about the screening for the best condition of crystallization, there are many aspects that a crystallographer should bear in mind, namely the feautures addresing the nature of the protein, a good bibilographic screening, the strategy of crystallization centered on the protein itself, the test on different adducts. Even when preliminary strategies have helped to reduce certain options, searching for diffraction-quality crystals involves the screening of a large and combinatorial number of variables, such as concentration and inclusion of specific additives and precipitants, temperature, pH, ionic strength, temperature. The total number of possible solution conditions to be tested is so great as to prohibit an exhaustive search.

Once large diffracting single crystals are obtained, collected X-ray data consist of structure factor amplitudes. However a critical component, namely the phase associated with each amplitude, cannot be recorded directly. In order to determine the structure, this phase information has to be recovered. There are three principal methods for determining the phases. Single/multiple isomorphous replacement (SIR/MIR) and single/multiple anomalous diffraction (SAD/MAD) are *ab initio* methods, for which no prior structural knowledge is required [6]. The molecular replacement (MR) method on the other hand relies on having available a structurally similar model of the target protein. Automation and high-throughput techniques are also finding their way into the subsequent steps of the structure determination pipeline: Multi-wavelength anomalous dispersion (MAD) (and its single-wavelength equivalent, SAD) using synchrotron radiation is now a routine method for solving crystal structures, and human intervention is continuously being reduced in subsequent computational steps [7, 8].

1.2.3 High-throughput and parallel screenings

As we mentioned in the previous paragraph, nowadays all these alternative approaches can be explored in a parallel or cyclical fashion. The parallel approach uses in theory more resources but thanks to the diffusion and implementation of low-volume robotic automatized methods the waste of time, labware and sample has drastically decreased in the past decade. The key advantage of parallel screening is the possibility of obtaining multiple successes or hits, incresing the flexibility of the process and the number of possible strategies. Finally, when a sufficiently broad protein expression or purification or crystallization screen fails to yield any success, this can be used to inform important project decisions, leading to either termination or selection of a significantly different approach [3, 7].

1.2.4 Biomolecular solution NMR

NMR is an extremely powerful tool that is able to report on the exact environment of each atom of a molecule, thus shedding light on its 3D structure. In addition, NMR is particularly suitable to monitor intermolecular interactions, and detects whether a molecule binds to a target protein or nucleic acid, and which parts of the molecules are interacting.

However, determination of 3D structures of large proteins or biological complexes by solution NMR methods contains a great deal of challenges, since the large molecular size of these molecules entails two dramatic effects on their NMR spectra. First, an increased crowding of resonances occurs, which can be partially alleviated with the combination of sophisticated isotope labeling and of elaborated multidimensional experiments. Second, and most importantly, a transverse relaxation rate, which gets faster with increasing molecular size, prevents efficient transfer of the magnetization (figure 1.3).

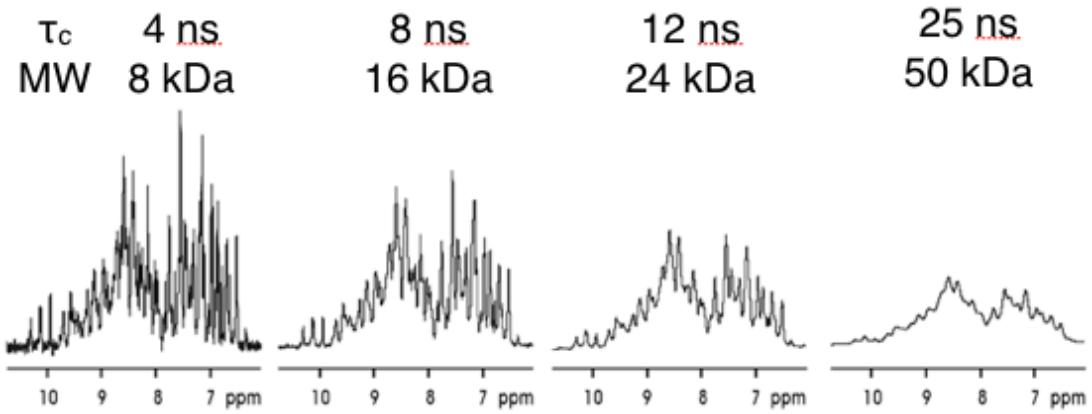

Figure 1.3: The tumbling time (τ_c) of proteins is an increasing function of the molecular weight (MW), with profound impact on the resolution, here illustrated in the case of ^{1}H NMR spectra.

Over the last past years, techniques have been introduced to attenuate the drawbacks connected to relaxation, like TROSY (Transverse Relaxation Optimized Spectroscopy), or to eliminate entire relaxation pathways, as for example by deuterium labeling. These techniques have helped in lifting the experimental limits of possible solution NMR targets, but have enabled access to large protein domains only in few favorable cases. In parallel, sophisticated computational protocols for solution NMR data analysis have recently emerged as valuable tools to solve the giant jigsaw puzzle created by large biological systems made up by thousands of little pieces (NMR signals) giving only clues about neighboring atoms and inter-domain arrangements. Notably, the limited experimental information available about conformational restraints for inter-domain interfaces imposes a substantial challenge for consistent re-construction of any complex molecular architecture.

Finally it is important to stress that, although X-ray crystallography and NMR look complementary, from the point of view of data processing and interpretation, determining a protein structure by X-ray crystallography is substantially less demanding and time-consuming than

X-ray	Solution NMR
types of samples	
Macroscopically ordered sample, well-diffracting crystals (high quality X-ray diffractograms - beyond 4.5 $\AA$ Bragg spacing)	Liquid samples, molecules tumbling sufficiently fast in solution and/or ligand-protein exchanges that take place on the medium to fast time scale. The maximum size of systems under study has been in the last decades addressed through different strategies.
limit sizes of systems	
Crystallization dynamics can become very slow (lower concentrations)	Line widths deteriorate substantially with increasing molecular weight
proton and protonless systems	
Empirical energy placement and neutron diffraction comparison are needed for determination of polar hydrogen positions	^{13}C direct detected protonless NMR spectroscopy is a powerful tool to characterize systems where ^{1}H signals are difficult to analyze, such as paramagnetic systems, unfolded proteins, systems where HN signals cannot be observed due to exchange broadening, and possibly molecules of large size.
conformational mobility	
While crystallographic techniques can provide information at a similar level of specificity, the resolution of a small population of an alternative conformation is difficult. B factors associated with increased conformational flexibility but conformational heterogeneity could lead to similar effects.	direct identification of the specific factor (example, cis-trans isomerism of a single proline residue) leading to the presence of multiple native forms of a protein in solution. NMR is uniquely well suited to the identification of this type of conformational heterogeneity. It is common to present NMR-derived structures as an ensemble of structures. Each structure in the ensemble is consistent with the experimental NMR data used to calculate it.

Table 1.1: Important topics and differences between solution NMR and X-ray crystallography as biophysical techniques.

determining a solution NMR structure. Automation of data-collection and processing has been fully implemented in X-ray crystallography while for NMR some softwares are still in the development stage. The steady advance of technology, largely geared to synchrotron beamlines, has dramatically increased the speed and ease of X-ray data collection over the past decades.

1.2.5 Biomolecular solid-state NMR

Even if progress in protein structure determination has been tremendous over the last years, traditional structural biology methods still show at present date important technical limitation: large classes of proteins cannot be investigated using both liquid state NMR or X-ray crystallography, either because the related proteins cannot be crystallized to a sufficient diffraction quality for X-ray diffraction, or they cannot be brought into a sufficiently concentrated solution, or they have inherent molecular weight limitations and are too large for liquid-state NMR. These aspects concern proteins (and related protein aggregates) containing predicted transmembrane regions, coiled-coil structures, or extended low-complexity sequences, that play a central role

in many scenarios of fundamental and clinical importance and take place in a more complex and dense cellular environment than previously envisioned. These include cellular response to outside stimuli, such as light or nutrients, intercellular communication and mediation of biological processes or the process of protein aggregation in the context of Alzheimer's or Parkinson's disease [9]. In this context, holistic structure-determination methods that can be applied in a complex molecular environment are of prime importance to understand these fundamental processes at atomic resolution and restore them in a pharmacological context.

aggreagtion states	**target systems**	**biophysical targets**
fully or partially immobilized biomolecules	small globular proteins	atomic level description
gels	intact viruses, RNAs, DNAs	long range constraints
cryo- and lyoprotected buffered glasses	insoluble fibrils	high MW
precipitates	liposomes	long range constraints
biomolecules dissolved in ordering mesophases	prions	collective dynamics unmatched by other biophysical techniques
nanocrystalline materials in contact with mother liquor	integral membrane proteins, hormone receptors, ion channels, energy transducers	(folding, misfolding, domain swapping)

Table 1.2: Main goals of modern biological solid-state NMR.

- **Membrane proteins.** One of the major challenges in structural biology is the resolution of membrane protein structures. The high portion of proteome represented by integral membrane proteins, for which 30 % of the proteinogenic genes code, is generally difficult to crystallize in functional form and mostly insoluble in water without detergents [10]; in facts, although small membrane and membrane-spanning (transmembrane) proteins below 50 kDa may be investigated using solution NMR, most of them have multiple domains and are frequently organised as large multimeric complexes of several hundred kDa of size, systems in which the restricted molecular motions result in broad NMR spectra. This is a key problem, since membrane receptors or channels frequently interact with ligands and are involved in a number of important physiological processes including selective transport, cellular communication and mediation of biological processes. Lipids associated with these proteins impede crystallization needed for X-ray crystallography and quench the rapid reorientation in solution that is a prerequisite for solution NMR spectroscopy. For the study of membrane proteins in any case the usage of detergents is often mandatory, and examples of ssNMR studies are present.

- **Amyloid fibrils and other disease-related protein aggregates.** Amyloid fibrils are highly organized filamentous structures resulting from the spontaneous self-assembly of polypeptide molecules that in their soluble forms can have a wide variety of secondary structures and functions. In these aggregates, many copies of the chain assemble into fila-

ments, typically 5-10 nm in diameter and few microns in length [11]. Although numerous peptides and proteins not directly related to diseases also can form amyloid-like fibrils in vitro, suggesting that amyloid fibril formation is a generic property of the polypeptide chain [12], current interest in the subject comes from their role as pathological hallmark of more than 20 protein deposition diseases including type II diabetes (in which they develop in Pancreas), Alzheimer's disease and the transmissible spongiform encephalopathies (in which they form plaques in the brain). The role of these aggregates in these diseases is not clear, and the mechanisms that contribute to cell death are not entirely known. It is thought that detailed atomic-resolution structural information about the individual peptide strands that make up the protofilaments would help explain why amyloid formation is a common property of polypeptide and would facilitate drug development, but despite the immense medical importance, it has proved difficult to obtain, because the intact fibrils are inherently insoluble and, although the fibrils are large multi-molecular assemblies, they lack complete 3D order and do not form diffraction-quality 3D crystals.

NMR techniques particularly designed for the study of solid-phase systems (solid-state NMR or ssNMR) can play an important role in current biophysics, acting as a promising complementary technique, by providing, similarly to solution NMR, exclusive structural and dynamic insights at atomic resolution in fully immobilized molecules that lack the macroscopic order required for X-ray diffraction and/or tumble too slowly, like many large biological assemblies.

In the case of biological macromolecules, anisotropic interactions encode important information about bond and plane orientations, and their measurement can result in a detailed structure determination. Traditionally, this is performed on static samples possessing a macroscopic orientation, such as single-crystals or membrane proteins, which can be aligned in lipid bilayers. The experiment consists in taking a series of spectra where the crystal or the bilayer is rotated stepwise about an axis perpendicular to the external field B_0. These spectra are combined in so called rotation patterns, displaying the resonance frequencies as a function of the rotation angle. In alternative, a single sample orientation can be investigated by means of more sophisticated 2D correlation experiments. On aligned helical membrane proteins, for example, an experiment where ^{1}H-^{15}N heteronuclear dipolar couplings are correlated with ^{15}N chemical shift (the so-called PISEMA experiment, Polarization Inversion Spin-Exchange at the Magic Angle) yields characteristic wheel-like patterns allowing to map the protein structure. For example, deuterium, phosphorus and carbon NMR have been widely used for the study of the structure and dynamics of biological membranes. The predominant source of line broadening for deuterium is the electric quadrupolar interaction while for phosphorus and carbon, the anisotropic chemical shift and the heteronuclear dipolar coupling with protons are both strong.

1.2.6 Microcrystalline samples

In the last decade, intense developments by several groups all over the world in the areas of NMR spectroscopy, biophysics, and molecular biology have significantly expanded the repertoire

of problems uniquely addressed by ssNMR, extending its application to sample lacking a global alignment.

In general, solid-state NMR spectra directly report on the structural heterogeneity of the sample. Although heterogeneity may be an advantage if intrinsically disordered systems have to be studied, in the case of globular microscopically well-ordered protein system it is more important to minimize it, since maximum spectral resolution is most easily achieved for samples showing high structural homogeneity with minimal inhomogeneous contributions to the ^{13}C and ^{15}N linewidths.

For large conformationally rich molecular systems, the most readily accessible solid form of solid preparation, lyophilized powder, however, yields insufficient chemical shift resolution [13]. This is simply a result of the well-known fact that chemical shifts are sensitive to molecular conformation, which results quite generally in ^{13}C linewidths of 1-2 ppm for samples that can be described as glassy. Although the proteins in a lyophilized powder might be properly folded, it is to be expected that the conformation of side chains will be quite variable. Each molecule then will have a slightly different shift for each chemically equivalent site because they are rendered magnetically inequivalent by this structural heterogeneity. Linewidths for lyophilized proteins are typically not narrow enough to provide for resolution of single sites by NMR spectroscopy.

In any case, under favorable circumstances lyophilized, rehydrated protein samples may yield satisfactory resolution. Significant effort has been expended on improving the resolution of ssNMR spectra for lyophilized samples by use of structure and hydration stabilizing additives. Enhanced resolution in the ^{31}P NMR spectrum has been observed for ligands bound to the enzyme 5-enolpyruvyl-shikimate-3-phosphate in lyophilized preparations protected by the addition of trehalose and polyethylene glycol (PEG) prior to lyophilization [13]. Trehalose has been used as a protectant against dehydration [14] since it was discovered that organisms adapted to very dry conditions contain high concentrations of this carbohydrate. The conformation and mobility of dehydrated proteins with and without these additives has been studied by ssNMR and by X-ray diffraction. For most proteins, keeping samples hydrated is found to do a better job of preserving native structure and retention of activity in the solid state, and provides higher resolution NMR spectra than lyophilization without such precautions. Unfortunately no procedure for preparing protein samples for ssNMR investigations had been discovered which results in resolution comparable to that obtained on crystalline material [15].

Resolution has been critically compared for SH3 samples prepared by lyophilization with and without rehydration or protection with PEG and sucrose, and precipitation with ammonium sulfate [32]. The hydrated microcrystalline precipitate yielded the best ^{13}C spectral resolution of the samples examined, with linewidths comparable to those typical of small crystalline model compounds. Even using multidimensional NMR methods, lyophilization has not been found to provide sufficiently narrow lines.

A revolution in this area was represented by the demonstration that nano-crystalline material far too small to be useful in X-ray diffraction studies is suitable for structural or other biophysical studies by ssNMR [15] (figure 1.4).

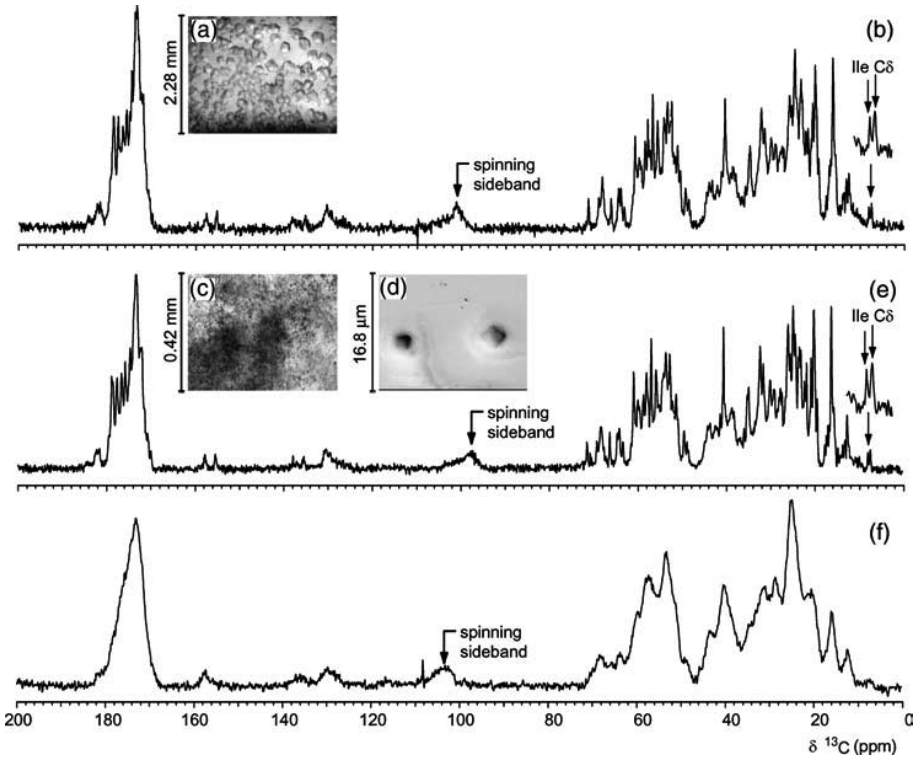

Figure 1.4: from [15] (a) Ubiquitin crystals grown in a sitting drop (approximately 200 μm across the widest point of an average crystal). (b) Solid state ^{13}C spectrum of a polycrystalline sample composed of crystals grown using the same conditions. (c) Nanocrystals produced using rapid batch crystallization with starting conditions as in the sitting drop well of (a). (d) An electron micrograph of the same sample, showing larger than average nanocrystals, have the same cubic morphology as the larger crystals. (e) The solid state ^{13}C NMR spectrum of the nanocrystals looks practically identical to that of the polycrystalline sample. (f) The ^{13}C solid state spectrum of lyophilized ubiquitin is poorly resolved, indicating structural heterogeneity in the sample.

Essential ingredient for the success of solid-state NMR experiments is therefore the presence in the sample (or in big part of it) of local order and a homogeneous environment, such as that of a microscopically well-ordered (structurally homogeneous) sample with minimal inhomogeneous contributions to the ^{13}C and ^{15}N line widths. Single crystals are not required, but the spectrum has to be characterized by the spectral dispersion and line widths of a well-folded, well-ordered protein. Many conditions discarded for X-ray crystallography are indeed possible matches for solid-state NMR.

It has been emphasized recently that apparently non-crystalline precipitated proteins used by ssNMR spectroscopists can, in some cases, be nano-crystalline; however, the relationship between medium-scale order or crystallinity and line-width remains to be clarified.

1.3 Example systems studied (2002-2012)

As in liquid-state NMR, sequential resonance assignment of the entire polypeptide chain forms the basis for the structural analysis of a solid protein. The breakthroughs in sample preparation, coupled to a number of advances in magic angle spinning (MAS) solid-state NMR instrumentation and methodology (see chapter 2), have led to a variety of strategies for the assignment of ^{13}C and ^{15}N resonances in uniformly labeled peptides and proteins.

The first partial resonance assignments were reported for the 76-residue protein ubiquitin [16, 17], the 58-residue peptide basic pancreatic trypsin inhibitor BPTI] [18] and the cyclic decapeptide antamanide [19], and the dimeric form of the 85-residue catabolite repression histidine containing protein Crh, that predominantly occurs in a monomeric form in solution [20].

The first protein for which nearly complete ^{13}C and ^{15}N sequential resonance assignments were obtained is the SH3 domain of α-spectrin (62 residues) [21].

In turn, the availability of resolved NMR correlations has paved the way to the first three-dimensional structure determinations at atomic resolution of biomolecules in the solid state. Similarly to solution NMR, it can be used to determine interatomic distances (both intramolecular and intermolecular), place constraints on backbone and side-chain torsion angles, and identify tertiary and quaternary contacts. In this way, full molecular models for insoluble and incompletely ordered solid material (both amorphous and non-crystalline) can be developed from solid-state NMR data, especially when supplemented by lower-resolution structural constraints from electron microscopy and other sources. In addition, solid-state NMR data can be used as experimental tests of various proposals and hypotheses regarding the mechanisms of enzymatic reactions [22].

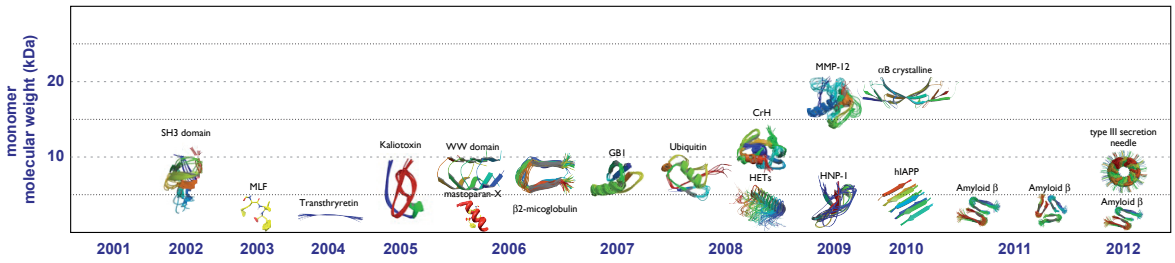

Figure 1.5: Protein structures determined by solid-state MAS NMR (2002-2012).

A major breakthrough in this field has been achieved in 2002 by Oschkinat and coworkers [23, 24], who were able to determine the first solid-state protein structure of the microcrystalline SH3 protein, by recording two-dimensional proton-driven spin diffusion (PDSD) spectra and by interpreting the cross peak intensities simply as qualitative upper bounds of distance restraint subsequently used in molecular modeling, in an analogous way as NOESY cross peak intensities are often used in solution NMR. In parallel, it has been demonstrated that conformational

restraints in solid proteins can be alternatively probed between ^{1}H spins. These are the so-called two-dimensional CHHC and NHHC experiments, which were successfully applied by Baldus and co-workers to determine the three-dimensional molecular structure of kaliotoxin [25].

Since, a series of high-resolution three-dimensional structures have been determined on solid microcrystalline proteins [26, 27, 28, 29, 30, 31] membrane bound-systems and fibril forming peptides (table 1.3 and figure 1.5) [32]. ssNMR spectroscopy has proved to be a precious technique to study dynamic processes, being capable to resolve detailed and important site-specific information about motions spanning a vast range of timescales ranging from ps to ms to seconds [33, 34, 35, 36, 37, 38, 39, 40]. It has been notably shown that rigid and more mobile polypeptide segments can been discriminated according to their different spectroscopic signature [41].

protein	PDB code	BMRB entry	oligomer size/state	production source	medium	ref
MICRO-CRYSTALLINE PROTEINS						
Spectrin SH3 domain	1M8M		7 kDa/1	Escherichia coli	-	Castellani et al. (2002)
Kaliotoxin	1XSW	6351	4 kDa/1	Escherichia coli		Lange et al. (2005)
Beta1 immunoglobulin binding domain of protein G (GB1)	2JU6 2JSV 2K0P 2KQ4 2KWD 2LGI	15156	6 kDa/1	Escherichia coli	-	Zhou et al. (2007) Franks et al. (2008) Robustelli et al. (2008) Nieuwkoop et al. (2009) Nieuwkoop and Rienstra (2010) Wylie et al. (2011)
Crh domain swapped dimer	2RLZ	5757	19 kDa/2	Escherichia coli	-	Loquet et al. (2008)
Ubiquitin	2JZZ 2L3Z		9 kDa/1	Escherichia coli	-	Manolikas et al. (2008) Huber et al. (2011)
MMP-12	2K9C 2KRJ	7415	17 kDa/1	Escherichia coli	-	Balayssac et al. (2008) Bertini et al. (2010)
PRECIPITATED PROTEINS						
Alpha-beta crystallin	2KLR	16391	40 kDa/2	Escherichia coli	-	Jehle et al. (2010)

protein	PDB code	BMRB entry	oligomer size/state	production source	medium	ref
PROTEINS FORMING FIBRILS						
Transthyretin fibrils	1RVS		1 kDa/1	synthetic	-	Jaroniec et al. (2004)
Amyloid protofilaments of beta2-microglobulin fragment	2E8D	10202	10 kDa/4	Escherichia coli	-	Iwata et al. (2006)
WWT domain of CA 150	2NNT		18 kDa/4	Escherichia coli	-	Ferguson et al. (2006)
Beta-amyloid protein 40	2LMN 2LMO 2LMP 2LMQ	18127	52 kDa/12 78 kDa/18	synthetic	-	Petkova et al. (2006) Paravastu et al. (2008)
Amyloid fibrils of the HET-s (218-289) prion	2RNM 2KJ3 2LBU	11028 11064	43 kDa/5	Escherichia coli	-	Wasmer et al. (2008) Van Melckebeke et al. (2010) Schutz et al. (2011)
Fragment of the human islet amyloid polypeptide (hIAPP)	2KIB	20074	6 kDa/8	synthetic	-	Nielsen et al. (2009)
Type-III Secretion System Needle	2LPZ	18276	257 kDa/29	Escherichia coli	-	Loquet et al. (2012)

protein	PDB code	BMRB entry	oligomer size/state	production source	medium	ref
MEMBRANE PROTEINS IN MEMBRANES						
Influenza M2 channel residues 22-46	2KAD 2KQT	16020 16612	11 kDa/4	synthetic	lipids	Cady et al. (2009) Cady et al. (2010)
Integral membrane domain of the mercury transporter Mer F	2LJ2	17914	6 kDa/1	Escherichia coli	DMPC	Das et al. (2012)
Protegrin-1	1ZY6		4 kDa/2	synthetic	POPC	Mani et al. (2006)
Mastoparan	2CZP	10001	2 kDa	Escherichia coli	DPPC:DPPG=4:1	Todokoro et al. (2006)
Human Phospholamban	2KYV		30 kDa/5	Escherichia coli	DPC and lipids	Verardi et al. (2011)
MICROCRYSTALLINE MEMBRANE PROTEINS						
Human alpha-defensin HNP-1	2KHT	16254	3 kDa/1	Escherichia coli	-	Zhang et al. (2009)
DsbB-DsbA complex	2LEG	17710	42 kDa/1	Escherichia coli	-	Tang et al. (2011)

Table 1.3: Protein structures determined by solid-state MAS NMR (2002-2012).

Chapter 2

Biomolecular solid-state NMR The bases

Nuclear Magnetic Resonance probes the interaction of microscopic, nuclear magnetic moments (such as ^{1}H, ^{13}C or ^{15}N spins) with a static magnetic field (B_0) and an external radio frequency (rf) field. Detection of nuclear magnetic resonance signals was first reported in 1946 [42, 43], and applications of NMR to probe the properties of matter have significantly advanced ever since, from solid-state physics to chemistry and biology. NMR spectroscopy has grown into an indispensable tool of chemical analysis, giving important contributions to our present molecular-level understanding of structure and dynamics of biological and synthetic (both organic and inorganic) systems. It is commonly used for a wide range of applications from the characterization of synthetic products to the study of molecular structures of systems such as catalysts, polymers, and proteins [44].

Although in modern chemistry laboratories most NMR experiments are performed on liquid-state samples, since the pioneering demonstration of cross-polarization ^{13}C NMR spectra of solid adamantane and benzene, solid-state NMR spectroscopy (ssNMR) has been alive and well. Much of the success of solid-state NMR spectroscopy is due to the evolution of a variety of techniques for studying internuclear distances, anisotropy, torsion angles, atomic orientations, spin diffusion, molecular dynamics, and exchange processes, while maintaining the analytical high resolution and sensitivity that constitute the hallmarks of practically useful NMR experiments in chemistry.

The role of solid-state NMR as biophysical technique is definitely recent. Since NMR has become a standard method for the characterization of three-dimensional (3D) structure and dynamics of proteins that undergo fast molecular reorientations, biomolecular applications of NMR spectroscopy have been often merely associated with soluble molecules (or magnetic resonance imaging). However, since the late 1970s, solid-state NMRspectroscopy has demonstrated its ability to provide atomic-level insight into complex biomolecular systems ranging from lipid bilayers to complex biomaterials. In the last decade, progress in the areas of NMR spectroscopy, biophysics, and molecular biology have significantly expanded the repertoire of ssNMR spectroscopy for biomolecular studies.

This expansion of solid-state techniques has occurred in recent years thanks to combined biological progress (sample preparation), technical progress (probe design, magnet technology, higher MAS spin rate), and methodological progress (new rf irradiation schemes). Steadily ongoing methodological developments combined with tremendous engineering advances in probe and spectrometer hardware, along with notably increased magnetic field strengths, have paved the way for studying the structure and dynamics of solid chemical and biological samples at atomic resolution, spanning a broad atlas of structures ranging from materials to protein aggregates or membrane proteins. The outcome of this impressive advancement is the possibility to characterize larger range of systems in many areas of modern structural biology.

This chapter presents an outline of the past developments, the recent progress, the current basics approaches and the future methodological challenges of solid-state NMR spectroscopy, namely techniques such as magic-angle spinning (MAS), cross-polarization, multiple-pulse sequences, homo- and heteronuclear decoupling and recoupling techniques for the sequential correlation of resonances, the detection of tertiary contacts and the characterization of torsion angles, These developments have enabled dramatic advances in the rate of data acquisition, quality of data obtained, as well as enhanced abilities to interpret the data in terms of molecular structure and function. Numerous excellent review articles have appeared in the past few years showing how the tools of solid-state NMR spectroscopy can be applied to solving specific problems [45, 44, 46] to which we suggest to refer for a wider perspective.

2.1 Spin interactions

Atomic nuclei are characterized by four properties: mass, electric charge, magnetism and spin. Nuclei with a spin quantum number unequal to zero possess a quantum-mechanical property that is called nuclear spin. In an external magnetic field B_0, a nuclear spin behaves like a tiny magnet and precesses with frequencies that depend on the local interactions and environment.

Physical interactions of nuclei with non-zero magnetic moments are quantum mechanically described by distinct terms in the Hamiltonian operator, which encompasses all the information of the spin system under exam and the environment with which this spin system interacts.

In general, for a system of nuclear spins $S = 1/2$, solid-state NMR experiments may be described by the Hamiltonian:

$$\hat{H}(t) = \hat{H}_0 + \hat{H}_{cs} + \hat{H}_J + \hat{H}_D \tag{2.1.1}$$

where the first term describes the Zeeman interaction with the external field, and the latter three terms describe the chemical shift (cs), scalar coupling (J), and dipole-dipole coupling (D). We do not consider here the fourth term of the Hamiltonian, $\hat{H}_Q$, related to the quadrupolar interaction, which is peculiar of nuclei with a non spherical distribution of charge ($S > 1/2$), although we will focus on it in Chapter 6.

Position and intensities of adsorption lines of NMR spectra derive from transitions between energetic levels, given by the quantum energies eigenvalues of the Schroedinger equation in which the spin Hamiltonian appears. The chemical shift is determined by the molecular environment while the nuclear spin dipole-dipole couplings are determined by the relative positions of the active nuclei so that both corresponding Hamiltonians are dependent on the orientation of the molecule with respect to the stationary magnetic field. This means that the resonance frequency of a given nucleus within a particular molecule depends on the orientation of the molecule. Figure 2.1 illustrates how the resonance frequency of a ^{13}C nucleus in a carboxyl group and a ^{15}N nucleus in an amide group vary for three particular orientations of a molecule with respect to the static magnetic field B_0.

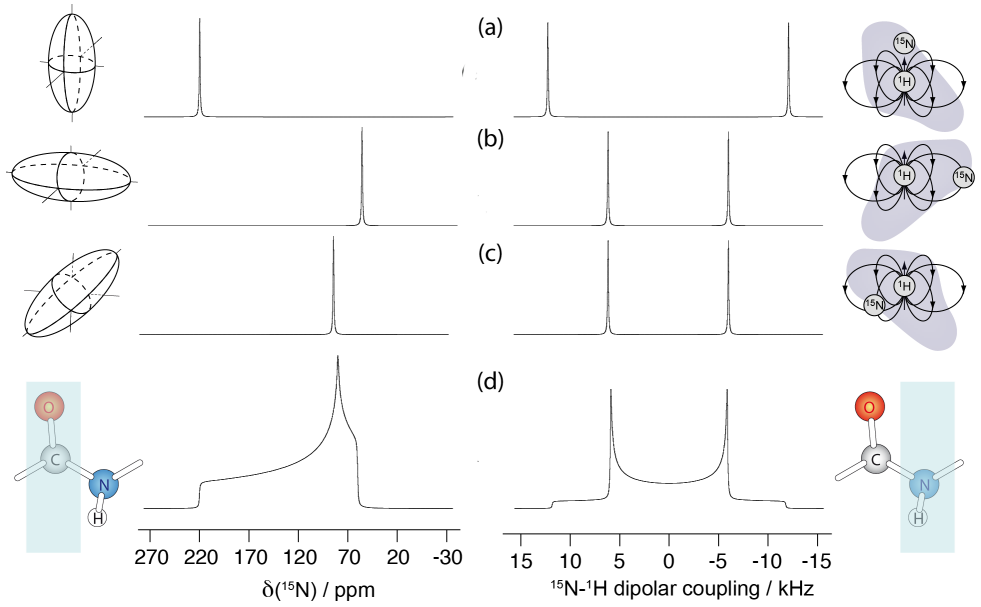

Figure 2.1: Numerical simulation of the NMR spectrum for three particular sample orientations (a-c) and for a static powder pattern (d) of a ^{13}C carbonyl chemical shielding tensor (left, δ_{iso} = 120 ppm, δ_{aniso} = 100 ppm, η= 0.2) and of an amide ^{1}H-^{15}N dipolar coupling tensor (right, $b_{HN}/2\pi$ = 10 kHz).

In solution, the isotropic tumbling of molecules averages out nuclear spin interactions that depend on molecular orientation, yielding spectra of sharp, separate peaks. On the contrary, in the solid state, or in materials that are solid-like in the sense that their internal molecular and atomic motions are highly restricted compared with the motions in isotropic phases, the nuclear spin interactions are typically governed by anisotropic (orientation-dependent) components in addition to the isotropic (orientation-independent) components well-known in liquid-state NMR.

In solid samples whose molecules or crystalites are randomly oriented ("powder" samples), all possible crystallite orientations are present simultaneously, and the NMR spectrum is the result of a sum over the uniform distribution of all these molecular orientations. The typical narrow isotropic resonances observed in liquid-state NMR (linewidths in the Hz range) are

interaction	**value**	**kind of nucleus**
^{1}H - ^{1}H dipolar coupling	60 kHz	CH_3 group
^{13}C - ^{1}H dipolar coupling	23 kHz	directly bonded CH pair
^{15}N - ^{1}H dipolar coupling	11 kHz	directly bonded NH pair
^{13}C - ^{13}C dipolar coupling	3 kHz	directly bonded CC pair
^{13}C - ^{15}N dipolar coupling	1 kHz	directly bonded CN pair
^{13}C chemical shift anisotropy	100 ppm	carbonyl
	10-20 ppm	aliphatic
^{15}N chemical shift anisotropy	100 ppm	amide N

Table 2.1: Value of the most common anisotropic interactions encountered in biomolecular solid-state NMR.

turned into the so-called "powder patterns" of solid phase NMR (linewidths up to hundreds of kHz, see table 2.1). Figure 2.1 illustrates the typical shape of powder patterns corresponding to a carbonyl chemical shielding tensor and to an amide ^{1}H-^{15}N dipolar coupling tensor. This kind of NMR spectra with broad peaks provide little information, or information that is difficult to deconvolve.

On one hand, the major task in solid-state NMR is to manipulate the spatial and spin parts of the complicated Hamiltonian in Eq. 2.1.1 in order to recover, out of the powder pattern, the typical narrow isotropic resonances known from liquid-state NMR for expanded spin systems, from which there is no resolution left in the solid state. On the other hand, the challenge is to maintain (or to reintroduce) sufficient spectral information for structure determination and/or for specific transfer of coherence/polarization among spins.

2.2 Magic-angle spinning (MAS)

Magic angle spinning (MAS) is a widespread method for increasing resolution in solid-state NMR and consists of rotating the sample rapidly about an axis tilted by an angle $\beta_m = cos^{-1}(1/\sqrt{3}) = 54.7°$ (the magic angle) with respect to the main magnetic field.

Depending on the spinning speed used and the magnitude of the anisotropic interactions, it is possible to increase resolution by averaging out chemical shift anisotropies and through-space dipolar couplings. As is apparent from figure 2.2, under MAS the static lineshape breaks into a family of sharp bands, spaced by the spinning frequency ("sideband pattern"). The center of gravity of the spin powder lineshape is the isotropic chemical shift, which is the same quantity observed in solution-state experiments, revealing the isotropic chemical shifts in centerbands and sequestering the details of the shift tensor into the relative intensities of the spinning sidebands. As the MAS rate ν_R is increased such that it exceeds the magnitude of the anisotropic interactions (i.e. becomes larger than the static linewidth), the signal is increasingly concentrated in the centerband position, and eventually the NMR spectrum reduces to the isotropic spectrum.

This effect of MAS on an anisotropic chemical shielding tensor is illustrated in figure 2.2,

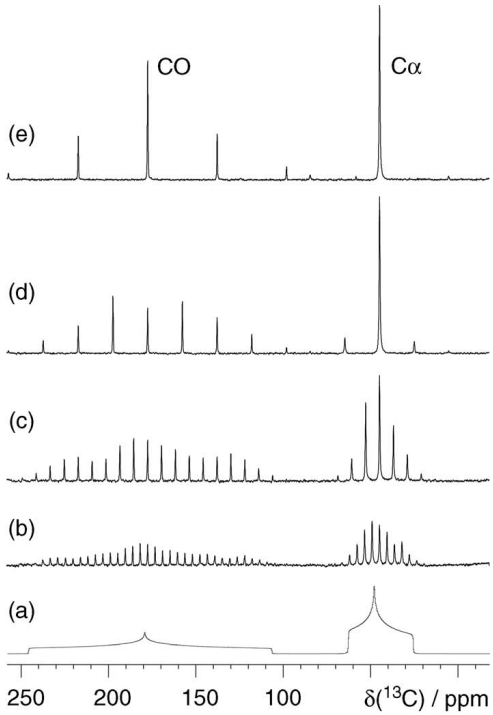

Figure 2.2: Simulated spectra Glycine. (a) The solid-state NMR spectrum of a static sample is shown, while from (b) to (e) the rotor frequency is increased. For slow MAS (b), spinning sidebands appear at multiples of the rotation frequency ω_r, while at fast MAS (e), the isotropic chemical shift is observed and the chemical shift anisotropy is averaged out.

showing the simulated static powder ^{13}C spectrum of a uniformly ^{13}C-labeled glycine powder sample along with spectra recorded using MAS with spinning frequencies of 1 and 10 kHz.

Complete averaging of dipolar interactions by MAS is only possible for the so-called inhomogeneous interactions such as the chemical shift and heteronuclear dipolar couplings. For homogeneous interactions such as proton homonuclear dipolar couplings, noncommuting parts of the Hamiltonian prevent this averaging unless the spinning speed is far in excess of the width of the powder spectrum. Because of their large gyromagnetic ratio, protons build a network of large dipolar couplings. On the one hand, this feature results in good sensitivity due to the large population differences, but on the other hand, it leads to significant line broadening. Effective ^{1}H-^{1}H dipolar couplings are in the range of 100 kHz, and even at high spinning speeds it is thus difficult to resolve individual ^{1}H resonances

As a result, solid state NMR has focused on the detection of rare nuclei such as ^{13}C and ^{15}N. Due to their low gyromagnetic ratio and low natural abundance, they have relatively weak dipolar couplings that can be averaged out with moderate spinning speeds and high power decoupling. However, these two factors also lead to low signal intensities as compared to protons.

2.3 Cross Polarization (CP)

The larger polarisation of protons can, however, be exploited to enhance the sensitivity of the low-γ nuclei, by transfer to the low γ nuclei via cross polarisation (CP) technique, developed by Hartmann and Hahn. CP employs double-resonance irradiation of the system such that a low γ dilute spin S (^{13}C or ^{15}N) derives an initial magnetization state from the larger Boltzmann population of a network of abundant spins I (typically ^{1}Hs) that are in close proximity via the heteronuclear dipolar coupling interaction[47]

In the case of a static sample, this phenomenon is driven by simultaneous, on-resonance rf irradiations, which spin lock both nuclear spins. In a doubly rotating frame, a CP process is then driven by flip-flop (zero quantum (ZQ)) transitions where both dipolar coupled spins change their magnetic quantum numbers in an energy conserving process. Energy matching is achieved when the nutation frequencies $\nu_1^I = \gamma_I B_1^I$ and $\nu_1^S = \gamma_S B_1^S$ caused by the rf fields are equalized for both spin types, thus fulfilling the so-called Hartmann-Hahn condition:

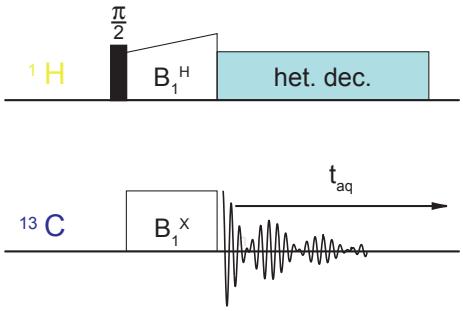

Figure 2.3: Schematic of a CP experiment.

$$\gamma_I B_1^I = \gamma_S B_1^S \tag{2.3.1}$$

Under MAS, the Hartmann-Hahn condition is split into sidebands separated by the rotation frequency:

$$\gamma_I B_1^I = \gamma_S B_1^S \pm n\nu_R \tag{2.3.2}$$

where $n = 1, 2$. In addition, cross-polarization under MAS can also occur through a second mechanism, which involves the double-quantum (DQ) part of the heteronuclear dipolar coupling (flip-flip transitions), and leads to a set of new matching conditions:

$$\gamma_I B_1^I = -\gamma_S B_1^S \pm n\nu_R \tag{2.3.3}$$

By CP, the amount of bulk magnetization of the dilute spin S is increased by a factor γ_I/γ_S, thus directly improving the signal intensity. A further benefit of the CP experiment is that the repetition delay between successive acquisitions of ^{13}C or ^{15}N signal is now determined by the T_1 relaxation time of ^{1}Hs, which is generally faster, such that many measurements of the FID can be acquired over a shorter experimental time.

2.4 Heteronuclear ^{1}H decoupling

MAS removes the orientational dependence of this interaction and successfully narrows linewidths for comparably small couplings. However, due to limitations on the spin rates that can be achieved, it is often not possible to fully average large anisotropic interactions (e.g. the ^{13}C-^{1}H dipole coupling) with spinning alone. As a result, it is often also necessary to apply decoupling irradiation (e.g. high-power proton decoupling) as part of the NMR pulse sequence to average the spin component of the coupling Hamiltonian. This entails applying a high-amplitude radio frequency field (B_1) at the Larmor frequency of the protons. This causes the ^{1}H spins to precess around the applied field so that, over an integer number of cycles and at long times, the average dipolar coupling reduces to zero. In practice, the strength of this rf field must exceed not only the heteronuclear carbon-proton coupling, but must also exceed the homonuclear proton-proton coupling. This ensures that the effective rf field term dominates the Hamiltonian so that the above picture holds true.

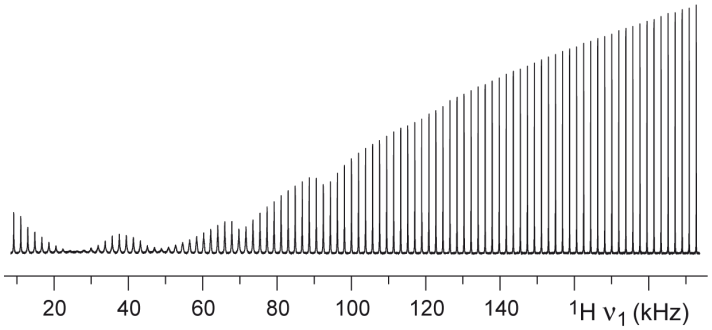

Figure 2.4: Intensity of the ^{13}C resonance in 2-(^{13}C)-L-alanine in a CP experiment at 25 kHz MAS under CW ^{1}H decoupling, as a function of the decoupling rf-field strength. Data acquired on a Bruker Avance III spectrometer operating at a proton frequency of 500 MHz equipped with a double-resonance 1.3 mm CP-MAS probe.

When applied in the form of a single continuous wave of rf irradiation, the efficiency of the decoupling increases with the field strength. However, both MAS and rf irradiation introduce a specific periodicity to the dipolar Hamiltonian, such that at certain ν_R, ν_1 conditions the effects interfere destructively to destroy (or enhance) the averaging effect. This phenomenon is illustrated in figure 2.4 on the ^{13}C line of 2-[^{13}C]-labeled alanine under MAS. For example, the heteronuclear dipolar coupling is reintroduced at the so-called "rotational resonances", when $\nu_1 = n\,\nu_R$ ($n = 1, 2$), with a resulting increase in the ^{13}C linewidth.

Many decoupling schemes have been developed to greatly increase the efficiency of line-narrowing across a range of rotation frequencies, generally where the irradiation is divided into blocks of pulses of varying phase. Heteronuclear decoupling schemes widely used in biomolecular studies are the TPPM (two-pulse phase-modulated decoupling) [36], and SPINAL-64 [37] (small phase incremental alternation) sequences, which are generally applied at ν_1 (^{1}H) = 80-100 kHz and for MAS spinning frequencies ν_R = 10-30 kHz.

2.5 Dipolar recoupling

The main effect of MAS is not only the suppression of unwanted line broadening. Since the term describing dipolar interactions becomes zero under fast MAS, dipolar interactions are partially cancelled out as well. This removal helps to narrow the ^{13}C or ^{15}N resonances, but also discards structural information contained in the anisotropic terms of the Hamiltonian.

In order to recover this information, useful for the structural characterization of a target substrate, the art is to, in a controlled manner, quench the MAS averaging for selected components of the Hamiltonian (e.g., a specific dipole-dipole interaction) in certain parts of the experiment by interference with rf irradiation. This phenomenon is referred to as dipolar recoupling.

A large number of pulse sequences has been developed over the last 20 years to provide efficient homonuclear recoupling under different experimental conditions. A first set of techniques, the so-called "first-order recoupling", prevent MAS averaging of dipolar coupling. RFDR (Radio-Frequency DRiven dipolar Recoupling), HORROR (double-quantum homonuclear rotary resonance), DREAM (dipolar recoupling enhanced by amplitude modulation) are some examples of first-order recoupling. These schemes are particularly useful to allow magnetisation transfer among neighbouring nuclei, but they are incapable of transferring magnetisation over long distances. Polarisation transfer mediated by weak dipolar interactions characteristics of long distances are cut off in the presence of strongly-coupled nuclei present at shorter distances. This phenomenon is commonly referred to as dipolar truncation. This drawback prevents the use of these methods for the identification of a complete spin-system, or for detection of long distance contacts that are important for structural determination. A second set of techniques, named "second-order recoupling" allow to alleviate the effect of dipolar truncation by generating an effective hamiltonian which contains homonuclear or heteronulcear dipolar coupling terms. The most popular is the PDSD scheme (proton-driven spin diffusion), which allows a coherent polarisation exchange between coupled ^{13}C spins in the presence of dipolar couplings to the ^{1}H bath which provide the energy necessary for the transfer. PDSD has allowed the first determination of a 3D structure of a protein in the solid-state (SH3 selectively labelled). Other schemes are DARR (Dipolar Assisted Rotational Resonance), MIRROR (mixed rotational and rotary resonance), PAR (proton assisted recoupling) and PARIS-xy (phase-alternated recoupling irradiation scheme). The biophysical applications of MAS experiments have expanded greatly with the development of several dipolar recoupling methods that reintroduce and measure specific dipolar interactions to obtain structural information.

2.6 Multidimensional techniques

Multidimensional NMR methods, in which the signal is plotted as a function or two or more frequency variables, have introduced a versatile and flexible approach in modern liquid and solid state NMR. Depending on the sample and its spin system, and how the spectrum is acquired, multidimensional spectra have many purposes: they can improve resolution and assignment of

resonances in complex NMR spectra aiding the interpretation of 1D spectra, provide additional constraints on molecular structure, provide information about time-dependent process within the sample.

A 2D NMR spectrum is obtained using rf pulse sequences divided in four periods, called preparation, evolution (or t_1), mixing and detection (or t_2). Preparation and mixing period have fixed duration and pulse structure. Free-induction decay signals are recorded during the detection period as a function of t_2 and the process is repeated for many values of t_1. the full data set, a function of two time variable, is Fourier-transformed to yield a spectrum that is function of two frequencies variables. Higher-dimensional spectra are obtained by introducing additional evolution and mixing periods.

Combined with uniform isotopic enrichment of ^{13}C or ^{15}N, these methods facilitate sequential assignments for the resonances in proteins. Numerous such methods have been demonstrated on model peptides [19, 48] and proteins [16, 48, 18, 21, 17], showning that 2D and 3D ssNMR can pull apart the myriad of resonances encountered in a protein, just as in solution NMR. Backbone and side chain ^{13}C, ^{15}N, and recently even ^{1}H resonances, can be correlated and assigned in multidimensional experiments as the first step in the structure determination of an entire protein in the solid state by NMR. However, in order to perform reliable assignments, the spectral resolution must be high enough to provide for a high percentage of resolvable single sites. Single site resolution for a majority of the expected resonances in 2D NMR spectra has only been demonstrated for small proteins in microcrystalline form: bovine pancreatic trypsin inhibitor [18] and the SH3 domain from α-spectrin [21].

2.7 Protein resonance assignment

Before a structural characterization in a multiply labeled sample can proceed, the observed signals must be identified. Assignment is the procedure in which each signal in a NMR spectrum is associated to each nuclei of the protein chain. Any investigation of a protein by NMR spectroscopy thus starts with the resonance assignment of the individual sites of the system.

Resonance assignment of a protein NMR spectrum is generally comprised of two steps: the identification of characteristic amino acid side chain patterns ("spin-system indentification") and the sequential connection of the different spin-systems along the protein backbone ("sequential" or "inter-residue connectivity").

In solution, these processes are accomplished in experiments where polarization transfers between directly bonded nuclei are driven by the J-couplings, and are performed using either radio-frequency pulses (INEPT) techniques, or spin-locking rf fields in Hartmann-Hahn methods. In fully protonated biosolids under moderate MAS, the efficiency of such correlation experiments is usually limited because of the long evolution delays necessary for creating and refocusing coherences between neighboring spins.

2.7.1 Spin-system identification

Resonance assignment in solid-state NMR usually begins with intraresidue homonuclear (^{13}C,^{13}C) correlation experiments that allow identification of different amino acid types based on their characteristic chemical shift correlation patterns.

Characteristic intra-residue (^{13}C,^{13}C) spin system patterns of side chains of individual residues are identified following a similar procedure to the one well established for liquid state NMR [49], using the characteristic signal patterns of homonuclear correlation spectra and the typical chemical shifts as reported in the BMRB [50].

- **Methyl-containing residues**
  Ala, Leu, Val ,Iso are readily identified by the typical chemical shift patterns, and multiple-bond cross signals involving their methyl group(s) in isolated regions of the spectrum.

- **Aspartic acid** and **Asparagine**
  Asp and Asn resonances may be easily identified using the Cγ-Cβ and Cγ-Cα cross signals.

- **Glycines** Gly are recognized by their isolated C'-Cα cross-signals.

- **Glutammates** and **Glutammines** Glu Cδ are isolated at the low field end of the spectrum around 185 ppm. The Gln Cδ chemical shifts are observed more upfield (around 180 ppm) and less isolated due to spectral overlap with backbone CO signals.

- **Aromatic residues** Phe, His and Tyr are identified by the typical chemical shift of their Cα-Cγ and Cβ-Cγ cross signals. In His-tagged systems, cross peak signals between aromatic carbons could show weak intensity and be partly obscured by aromatic resonances from the non-ordered 6xHis tag residues.

- **Serines** and **Threonines** These residues are rapidly identified due to the characteristic chemical shifts of both Thr/Ser(Cα) and Thr/Ser(Cβ) at the downfield limit of the aliphatic range of the spectrum.

- **Prolines** Pro are identified by their unique Cα-Cδ correlations.

2.7.2 Sequential correlations

Carbon-carbon correlations can be related to nearest neighbor ^{15}N spins in triple-resonance experiments. A key method in this regard is the SPECIFIC double cross-polarization (DCP) experiment, which yields sequential assignments by providing distinct N-CO and N-Cα transfers along the protein backbone. This experiment depends on the possibility of directing dipolar coherence transfer between N and C spins, based on the difference in the chemical shifts of the carbon resonances. For example, selective polarization transfer from backbone ^{15}N to ^{13}Cα carbon atoms can, in conjunction with subsequent (^{13}C,^{13}C) recoupling steps, be used to complete heteronuclear ^{15}N/^{13}C intraresidue spectral assignments.

The connectivity between adjacent polypeptide residues (interresidue assignment) can be established by directing the $^{15}N/^{13}C$ transfer from the backbone ^{15}N resonance to the nearest neighbor carbonyl group (i.e. of the previous residue). Sequential connectivities can thus be determined from the inspection of experiments where ^{15}N-$^{13}C\alpha$ and ^{15}N-$^{13}C\beta$ cross peaks are obtained via the combination of either intraresidue (NCA) or interresidue (NCOCA) ^{15}N-$^{13}C\alpha$ transfer. Due to the small chemical shift dispersion of ^{13}C NMR signals, a further homonuclear broad-band magnetization transfer to sidechain ^{13}Cs (NCOCX and NCACX) is often mandatory (see Figure 2.5).

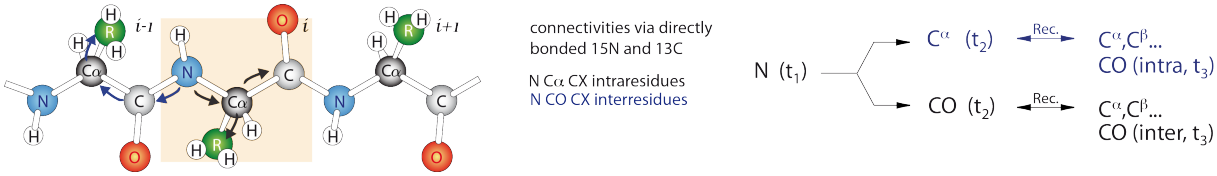

Figure 2.5: Spin polarization transfer pathways in carbon-detected 3D triple-resonance experiments for backbone and side-chain resonance assignment. Blue arrows and black arrows represent interresidual and intraresidual magnetization transfers, respectively.

Pulse sequences with typical pulses and delays, as well as example NCA and NCOCA experiments are illustrated in figure 2.6 on a microcrystalline fully-(^{15}N,^{13}C)-labeled sample of the B1 domain of protein G (GB1).

Each protein sequence presents several potential starting points for sequential assignments. These are generally pairs of residues with typical chemical shifts, or residues that are easy to identify due to their low abundance in the sequence. An unequivocal assignment solution can be found for several pairs. For others, the number of possible solutions can be reduced by continuing the assignment towards the N-or C-terminus.

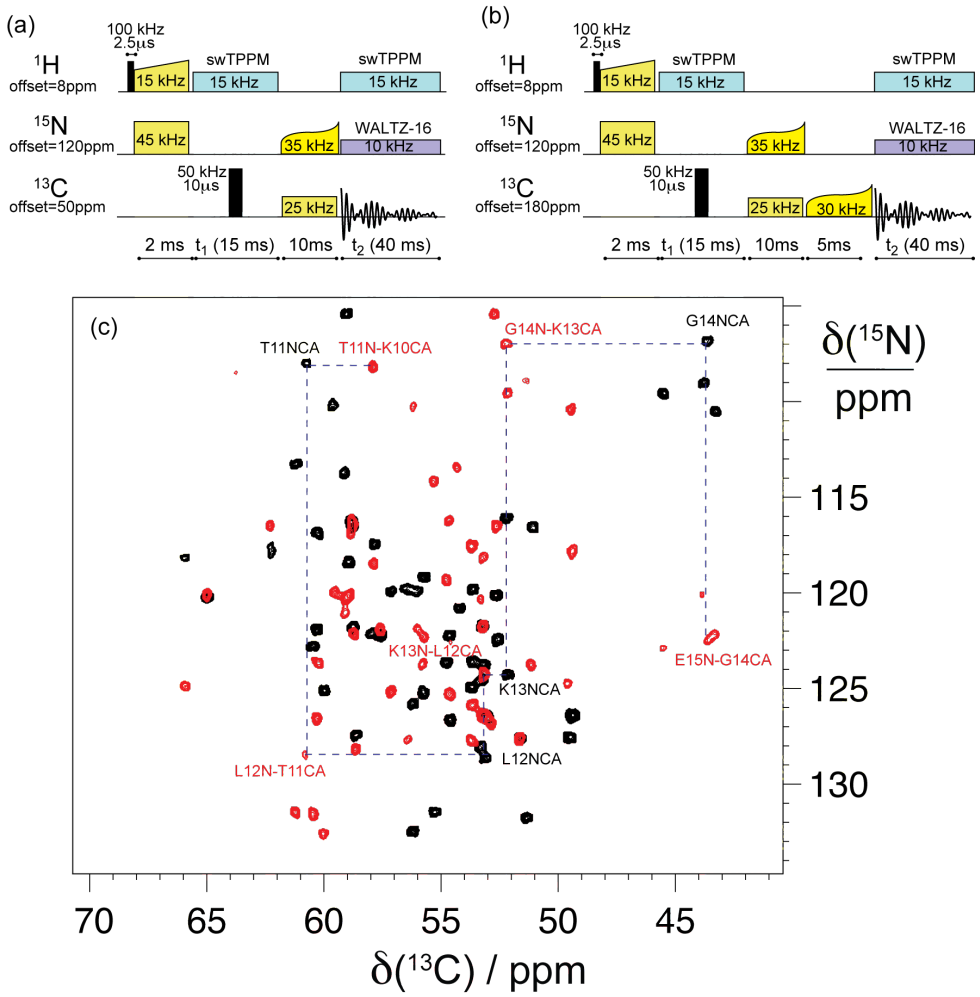

Figure 2.6: Pulse sequences and two-dimensional NCA (amide nitrogen to Cα carbon correlations, black) and NcoCA (amide nitrogen to preceding Cα carbon correlations, red) spectra of a microcrystalline sample of the B1 domain of protein G demonstrate the resolution and assignments now possible for small solid proteins. Dashed blue lines indicate sequential walks. Experiments were performed on a Bruker Avance III spectrometer operating at a proton frequency of 1000 MHz, and equipped with a triple-resonance 1.3 mm CP-MAS probe.

Chapter 3

The ϵ_{186} subunit of DNA polymerase III from *Escherichia coli*

Most of the globular model systems like SH3, GB1 and ubiquitin, used up-to-date for method development in biological solid-state NMR, are relatively small, in the range of 50 to 80 residues. In order to deal with bigger system, the N-terminal domain of the ϵ subunit of *E. coli* DNA polymerase III (ϵ_{186}: 186 residues, 18 kDa) has been selected as an interesting candidate to become a new model system in our lab. This protein has in fact many advantages: there are precise protocols for over-expression and purification in minimal labeled medium, published single-crystal X-ray structures are available, and it has proven to be stable over several months of experimental sessions. In addition, ϵ_{186} is a metalloenzyme, with paramagnetic Mn(II) or diamagnetic Mg(II) as cofactors and well-characterized metal binding pockets, which makes it a good candidate for the implementation of paramagnetic solid-state NMR techniques. The system can also be used for a complete biophysical characterization, studying its dynamics and its interactions with other polymerase subunits. The investigation of protein-protein interactions is a challenge for modern structural biology and one of the potential frontier of solid-state NMR. This chapter focuses on the first necessary steps towards this scenario: development of a simple and fast crystallization protocol (batch crystallization) and complete resonance assignment.

3.1 DNA replication: the replisome

DNA replication or DNA synthesis is the process of copying a double-stranded DNA molecule. This process is universal and paramount to all life as we know it. It proceeds in distinct stages, from initiation to elongation and finally to termination. Each stage of this process is mediated by multiple stable or transient interactions between protein subunits and DNA strands involving a subset of 30 or so different replication proteins of which the functions that are more or less conserved [51].

In particular, the elongation phase occurs within a large nucleoprotein assembly called replisome, a complex molecular machine which have never been isolated intact from cells and it is

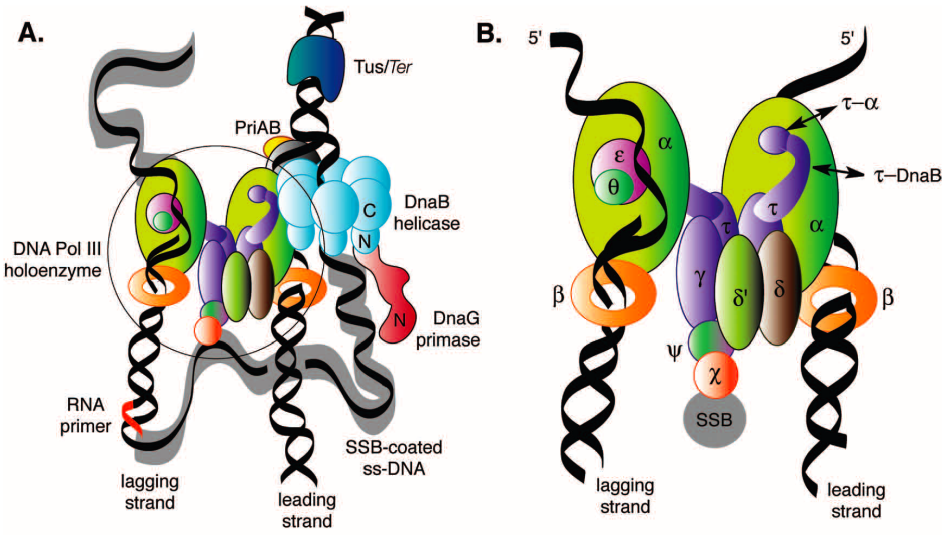

Figure 3.1: Schematic composition of replisome protein-protein and protein-nucleic acid interactions in the *E. coli* replisome (left), and in the replicase, the asymmetric dimer of the DNA polymerase III holoenzyme (right) [51].

made up of a number of subcomponents that each provide a specific function during the process of replication. The replisome faces special challenges as it makes new DNA at rates that can approach 1,000 nucleotides per second.

The mechanisms by which organisms faithfully replicate their DNA are of considerable interest. Fidelity of DNA replication is determined by three processes: base selection by a DNA polymerase, editing of polymerase errors by an associated 3' $\rightarrow$ 5' exonuclease and DNA repair. DNA polymerase can add free nucleotides to only the 3' end of the newly forming strand. This results in elongation of the new strand in a 5'-3' direction.

3.2 *E. coli* DNA polymerase III core

In *E. coli*, a Gram-negative rod-shaped bacterium, replication processes are performed by the replicative DNA polymerase III (Pol III) holoenzyme, with an error frequency of 10^{-10} per base pair replicated.

Since its discovery nearly 25 years ago, the *Escherichia coli* DNA polymerase III (pol III) holoenzyme (HE) has been studied extensively both genetically and biochemically as a model replication machine. Mechanistic studies have made extensive use of the *Escherichia coli* proteins, in part because they are separately isolable in large quantities from overproducing strains, and in vitro initiation, elongation and termination reactions have been faithfully reconstituted using defined DNA templates.

The 10 different protein subunits of the holoenzyme function in cooperation with other replication proteins to carry out the duplication of the entire *E. coli* chromosome with astonishing

efficiency, processivity, and fidelity. The Pol III holoenzyme is comprised of a core of three subunits (α, ϵ, θ) and seven accessory subunits that together contribute to its extraordinary efficiency, processivity, and fidelity.

The large 130 kDa α subunit includes the polymerase active site. The ϵ subunit (28 kDa), encoded by the *dnaQ* gene [52, 53], is the subunit providing the 3'-exonucleolytic activity for this enzyme. The separation of the polymerase and exonuclease activities of pol III between different subunits is in contrast to many DNA polymerases where both activities are present on a single polypeptide chain.

ϵ is composed of two domain: an N-terminal domain containing the proofreading exonuclease subunit (residues 1-186, ϵ_{186}) and a C-terminal domain required for binding to the polymerase (α) subunit (residues 187-243).

Both forms catalyzed the hydrolysis of the 5'-p-nitrophenyl ester of TMP (pNP-TMP) with similar values to those of ϵ_{186} itself of k_{cat} and K_M (spectrophotometric assay for measurement of the activity of the ϵ proofreading exonuclease).

The function of the 9 kDa θ subunit is unknown, but it has been hypothesized to enhance the 3'-5' exonucleolytic proofreading activity of ϵ.

3.3 X-ray structure of ϵ_{186}

The ϵ subunit is a binuclear metalloenzyme that works with either Mn^{2+} or Mg^{2+} in its active site. Crystal structures of ϵ_{186} have been solved by Hamdan *et al.* both at pH 5.8 (PDB entry 1J54) and pH 8.5 (PDB entry 1J53) [53, 54]. The structure at higher pH is shown in figure 3.2.

In all the deposited structures, electron density is continuous from R7 through G180, the first 5 and last 6 residues being disordered. Both structures are similar to that seen in all other structurally characterized DNA polymerase proofreading domains: for the pH-dependent variations in the structure of the active site, there was no significant difference between structures at two pHs. The subunit is folded into a α/β structure with an open, twisted β-sheet of five strands. The active site of ϵ_{186} in the crystal structure contains two divalent metal ions that both participate in substrate binding as well as its hydrolysis; it is located in a large cavity on one side of the central sheet, surrounded by two loops containing α-helices, the first one includes α_1 and α_2, while the second one includes the three C-terminal helices α_5, α_6, α_7. The exonuclease active site is formed primarily by negatively charged residues D12, E14, D103, D167. H162 is serving as a base deprotonating water, whose proton is accepted by E14. The resulting hydroxyl species serves as a nucleophile during exonuclease activity. The two Mn^{2+} sites can be occupied by a single Ln^{3+} ion, which allow a possible use in solid of paramagnetic constraint to analyze the interaction of the subunits in the replisome [55]. In solution lanthanide ions can readily be exchanged in the ϵ_{186}-θ complex and are alternative NMR strategy that competes with site-directed mutagenesis in speed, yet provides an accurate 3D representation of the protein-protein complex [55].

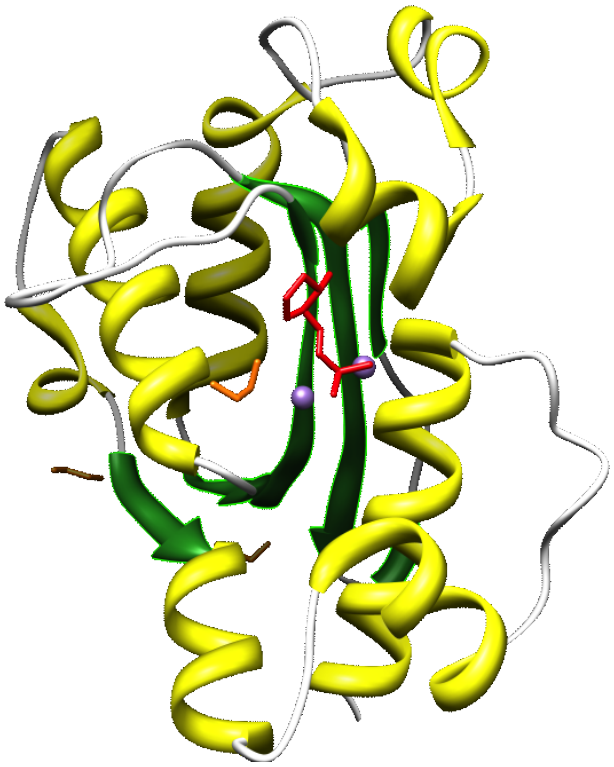

Figure 3.2: Ribbon representation of the X-ray structure *E. coli* ϵ_{186} (PDB code: 1J53)[54]. Crystals were grown at pH 5.8 in the presence of $MnCl_2$ and TMP, a product of its reaction.

3.4 Crystallization protocols

Doubly ^{13}C,^{15}N-labelled ϵ_{186} was expressed and purified in prof. Dixon's laboratory (University of Wollongong, Australia), according to an established protocol [55]. Sample immobilization is a key step to record highly resolved solid-state NMR spectra. As reported by Martin *et al.* [15], homogeneous nano- or microcrystalline preparations can be obtained by batch precipitation under the conditions obtained from screening for X-ray crystallography. Interestingly, some proteins precipitate in nano- or microcrystalline form, but crystals, large enough for X-ray diffraction cannot be obtained, and subsequent structure determination by X-ray crystallography is not possible. These systems are interesting targets for solid-state NMR in case solution NMR is not an option due to high molecular weight ($>$ 50 kDa) or multimerization. However, crystallization conditions found during screening may not be ideal for solid-state NMR measurements, for example because of high salt concentrations. In this chapter, aspects of sample preparation for solid-state NMR will be discussed. Furthermore a screening scheme will be proposed consisting of conditions which yield crystallization (or precipitation) of proteins in buffers suitable for NMR measurements.

3.4.1 Salt content and heating

Although state of the art NMR instrumentation is expected to extend the range of studies to more delicate systems ultimately, ssNMR probes have not historically been designed to perform optimally with protein samples at high ionic strength. Dielectric loading and electrical conductivity of the mother liquor surrounding the protein and/or the dielectric properties of the protein itself can severely compromise probe performance and reduce sample lifetime [56]. The application of high power ^{1}H decoupling exacerbates the problem. For example, figure 2.4 shows the intensity of the 2-(^{13}C)-L-alanine carbon signal under continuous wave (CW) heteronuclear decoupling as a function of the decoupling rf-field strength. The efficiency of the dipolar averaging is generally proportional to the amplitude of the decoupling field, i.e., the corresponding nutation frequency $\nu_1 = \omega_1/2\pi$ in kHz. Typically, this corresponds to a 100-300 W proton irradiation throughout the acquisition periods of the FID. The strong electrical fields associated with this rf irradiation can result in temperature jumps of greater than 50°C. Even if microcrystals proved to be stable up to temperatures of about 30-40°C (without rf irradiation), long high power pulse trains simultaneously applied on different channels can result in reversible signal loss even at lower temperatures. Moreover, irreversible degradation has been observed due to "sample cooking" during application of long (> 50 ms) and intense rf irradiation (> 100 kHz) during solid-state NMR experiments. These issues limit the experimental lifetime of protein samples for solid-state NMR and compromise biological relevance and/or spectroscopic resolution and sensitivity. It is worth to mention, that these effects are much more significant at high magnetic field strengths in combination with high salt content in the sample. Performing experiments under such conditions can cause rapid sample deterioration, and can reduce resolution due to temperature gradients across the sample. These effects can be minimized by lowering the temperature, the decoupling field or adopting special designed probes, for example, the development of low inductance coils that result in less electric field penetration in the sample and therefore less sample heating. Likewise, sample preparation and in particular precipitation of proteins for solid-state NMR from buffers with low ionic strength would contribute to overcome the hurdle of sample heating and degradation. ϵ_{186} for example can be crystallized employing precipitation buffer containing ca. 600 mM total salt but low salt conditions could be found for sample preparation employing screening schemes described in the next paragraph.

3.4.2 Screening for ssNMR

Schemes from traditional X-ray screening need to be adapted in order to screen for precipitation conditions suitable for solid-state NMR measurements. Two parallel strategies were followed to determine precipitation conditions for ϵ_{186} at low salt.

A first strategy was to manually screen for NaCl concentration. ϵ_{186} was crystallized by using low salt concentration in the sample buffer and subsequent 1:1 mixing with a solution containing the precipitant (PEG2K, PEG6K, PEG8K or MPD). The NaCl concentration in the reservoir solution was empirically optimized to around 0.2 M NaCl on 4 μL hanging drops in

Linbro plates (Hampton). Since the optimum concentration depends on drop size, up-scaling to 200-400 μL sitting drops required readjustment of of the NaCl concentration in the reservoir solution to around 3 M. Final conditions are reported in table 3.1

ϵ_{186} - pH 5.5 $\leftrightarrow$ 6.5		
	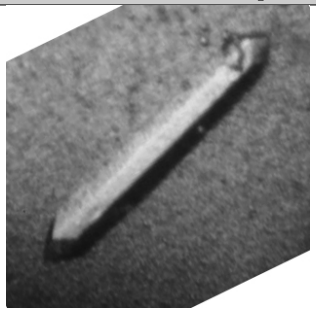	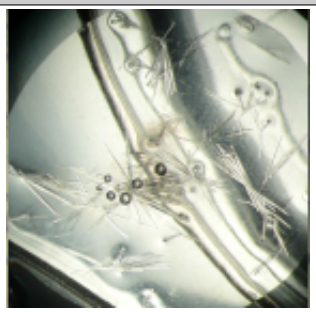
	Literature	**manual screening**
Source:	*J. Struct. Biol.*, **131**: 164-169 (2000)	24-plate screening
method:	hanging drop	hanging drop
temperature:	277 K	277 K
mixing:	3 μL + 3 μL	255 μL + 255 μL
protein:	11.5 mg/mL protein 50 mM Na · HEPES, pH 7.5, 2 mM DTT 5 mM TMP, 5 mM $MgSO_4$	11.5 mg/mL protein 50 mM Na · HEPES, pH 7.5, 2 mM DTT 5 mM TMP, 5 mM $MgSO_4$
precipitant:	20% PEG8K 100mM cacodylate (pH 5.8)	20% PEG8K 100mM cacodylate (pH 6.0)
reservoir:	precipitant	1 mL 3 M NaCl
crystal shape:	tetragonal prism	needle-shaped
crystal size:	0.2 mm x 0.2 mm x 1.0 mm	< 100 μm
time:	2-3 weeks	2-3 weeks
test:	X-ray (1.8 Å)	^{13}C NMR

Table 3.1: Refinement of the crystallization protocol for ϵ_{186} at pH 5.5-6.5. The form of ϵ_{186} at lower pH reported in PDB (1J54) is obtained in the literature by vapour diffusion method. This method is adjusted for lower salt content (right column). Although the PDB entry reports *Structure*, **10**: 535-546 (2002) as reference, the protocol is cited in that article only indirectly by an external reference.

In parallel, in collaboration with the EMBL Grenoble high-throughput crystallography (HTX) facility, we established automated screening processes in small volume batches linked to computer-based planning, execution and archiving was used to test multiple sample preparation conditions.

This allowed trying more complex matrix screening sets, so as to sample as as many experimental parameters (range of buffer, pH, additive and precipitant variables) as possible within the multi dimensional space of crystallization conditions, and explore regions which may be considerably away from the known or published crystallization conditions. Commercial low-volume high-density plates were used (Hampton Research or Qiagen). In particular, screening schemes were attempted by buffering the protein near its isoelectric point, and using different salts in the reservoir combined with varying amounts of PEG or other organic precipitants.

After setting up screening experiments, the outcomes were digitally recorded at pre-scheduled

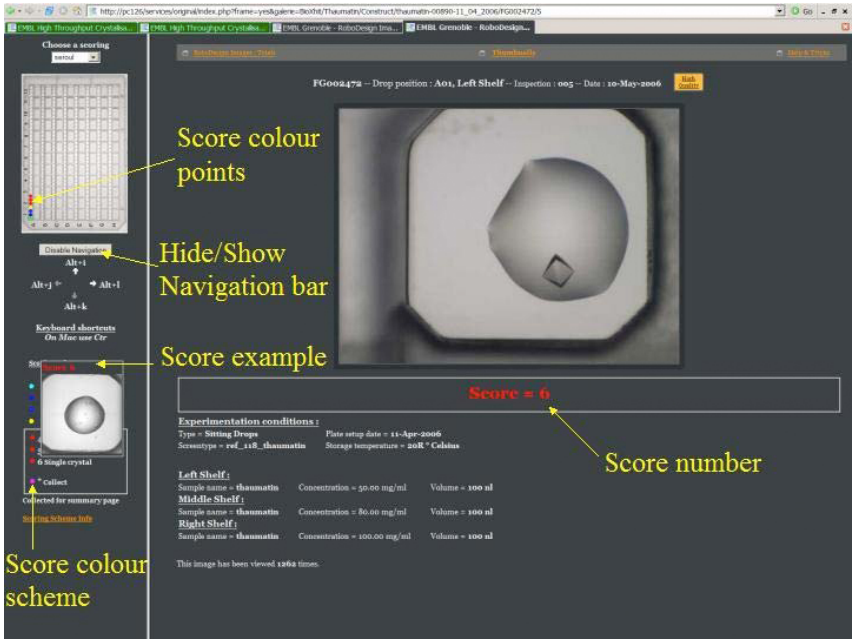

Figure 3.3: The HTX-EMBL interface for crystallization condition scoring.

intervals, usually one day after the addition of protein and weekly thereafter for a period of four-six weeks.

This technology permitted a fully automated and unattended inspection of well-plates by microscopic investigation coupled with camera detection at a rate of thousands per hour; images were stored on multiple hard drives and archived on offline media. Outcomes were reviewed to identify combinations of proteins and cocktails that demonstrate a propensity to microcrystallize.

The method yielded precipitation conditions at high pH, as displayed in table 3.2. After the screening for crystallization conditions, scaling up was performed by precipitation to produce samples for solid-state NMR, which were directly centrifuged into the NMR rotor.

The precipitation procedure was performed in close combination with the acquisition of standard NMR spectra, where the linewidth of the resonances will report on the quality/suitability of a given preparation. Our final preparation yielded well resolved ^{13}C-^{13}C spectra with line width at half height of approximately 73 Hz for the resolved Cδ resonance (Ile 104), including a J-coupling constant of 35 Hz typical for aliphatic carbons. ^{13}C linewidths of less than 100 Hz are needed for proceed with more complex NMR investigations (assignment and individuation of structural constraints, see below).

ϵ_{186} - pH 8.0 ↔ 9.0		
	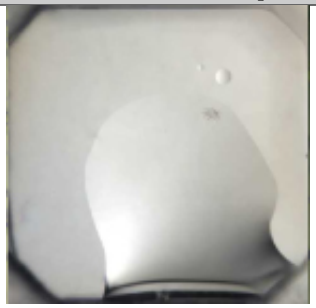	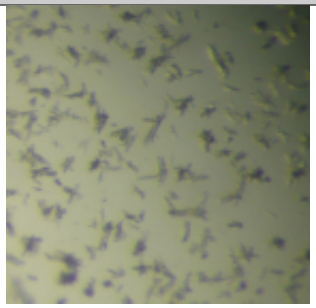
	HTX test	**manual screening**
Source:	FZ021703 -F07	24-plate screening
method:	sitting drop	sitting drop
temperature:	277 K	277 K
mixing:	100 nL + 100 nL	255 μL + 255 μL
protein:	11.5 mg/mL protein 50 mM Na · HEPES, pH 7.5, 2 mM DTT 5 mM TMP, 5 mM $MgSO_4$	11.5 mg/mL protein 50 mM Na · HEPES, pH 7.5, 2 mM DTT 5 mM TMP, 5 mM $MgSO_4$
precipitant:	20% PEG8K 100mM CHES (pH 9.5)	20% PEG8K 50mM CHES (pH 9.0)
reservoir:	8 μL precipitant	1 mL 3 M NaCl
crystal shape:	needle-shaped	needle-shaped
crystal size:		< 100 μm
time:	2-3 weeks	1 day
test:	X-ray (7 Å)	^{13}C NMR

Table 3.2: Refinement of the crystallization protocol for ϵ_{186} at pH 8-9. The form of ϵ_{186} at higher pH reported in PDB (1J53) is obtained in the literature by soaking low pH crystals three times into drops of 0.1 M HEPES, pH 8.5, 40% (w/v) polyethylene glycol (PEG8K), 2.5 mM $MnSO_4$, and 2.5 mM TMP.

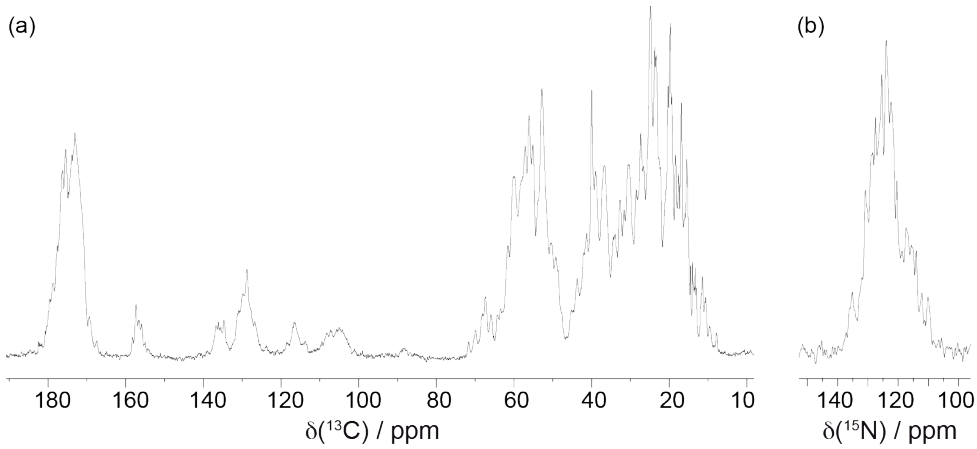

Figure 3.4: 1D ^{13}C and ^{15}N spectra acquired on microcrystalline ϵ_{186}, pH 9 (1.3mm rotor, 60 kHz MAS, 800 MHz Bruker spectrometer).

3.5 Resonance assignment

The strategy followed for ^{13}C and ^{15}N resonance assignment is summarized in table 3.3. It was based on 2D and 3D ^{13}C-detected spectra acquired on a triple-resonance 3.2mm probe.

	Non-sequential 2D check spectra quality, verify heating calibration verify axes calibrations, optimize CP building block		sequential 3D (backbone walks)
Preliminary	2D C-C short mixing number isolated spin systems (T)	2D NCO 2D NCA spin systems with anomalous/isolated 15N (P, G)	NCACX NCOCX short recoupling consecutive residues
Refinement	2D C-C long mixing complete spin systems (I,V) neighboring residues	TEDOR	NCACX NCOCX long recoupling secondary strcuture

Table 3.3: Spectra acquired for the complete ^{13}C and ^{15}N resonance assignment of microcrystalline ϵ_{186}, pH 6.0, 3.2mm rotor.

3.5.1 Spin-system identification

An extract of the 2D ^{13}C-^{13}C PDSD spectrum recorded with 15 ms mixing time at 700 MHz is shown in figure 3.5. From this map, spin patterns for most aminoacid types can be identified: examples involving Ile, Ala, Leu, Val, Pro, Ser and Thr are indicated in the figure.

Alanines (Ala), leucines (Leu), valines (Val), and isoleucines (Ile) were readily identified by the typical chemical shift patterns, and multiple-bond cross signals involving their methyl group(s) in isolated regions of the spectrum. Glycine (Gly) resonances were identified by their typical isolated CO-Cα cross signals in the carbonyl region (not shown here). Resonances relating to the proline residues (Pro) were easily observed due to the characteristic Cα-Cδ chemical shift pattern. The characteristic Cβ chemical shifts at the downfield limit of the aliphatic spectrum allowed for a straightforward identification of the complete set of serines (Ser) and of the twelve threonine (Thr) residues. Glutamic acid (Glu) resonances were in turn easily identified using the Cβ-Cδ cross signals. The aromatic residues phenylalanine (Phe), tyrosine (Tyr) and histidine (His) could be identified by the typical chemical shifts of their Cα-Cγ and Cβ-Cγ cross signals. The other residues appear in crowded regions in 2D ^{13}C-^{13}C spectra, and were identified and assigned using 3D ^{15}N-edited experiments, as described in the following sections.

3.5.2 Sequential assignment

As described in section 2.7.2, sequential connectivities can be determined from the inspection of experiments where ^{15}N-^{13}C cross peaks are obtained via the combination of either intraresidue

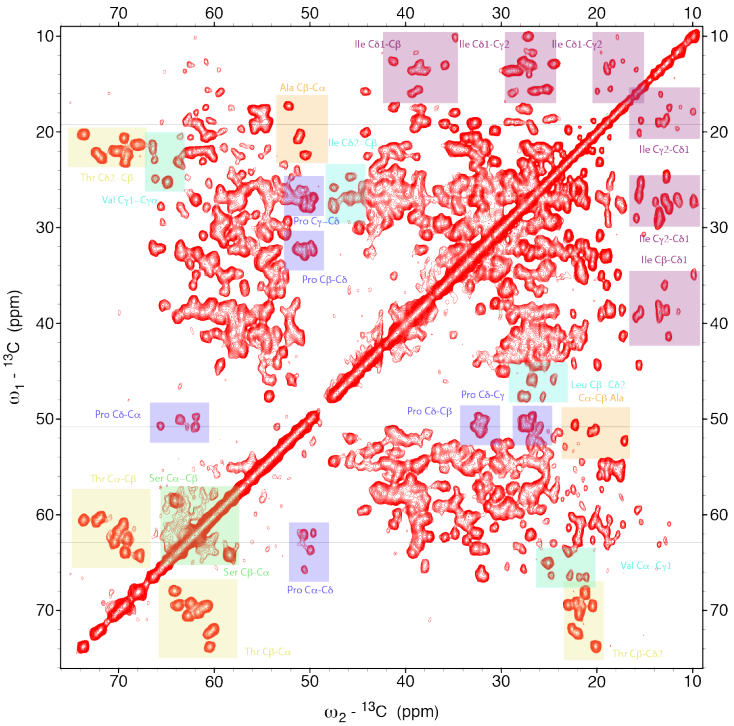

Figure 3.5: Contour plot of a ^{13}C-^{13}C PDSD spectrum (15 ms mixing time). Microcrystalline ϵ_{186}, pH 6.0, 3.2mm rotor.

(NCACX) or interresidue (NCOCX) ^{15}N-^{13}C transfers. The alignment of strips from these spectra yields a sequential walk, from which backbone resonances can be readily assigned.

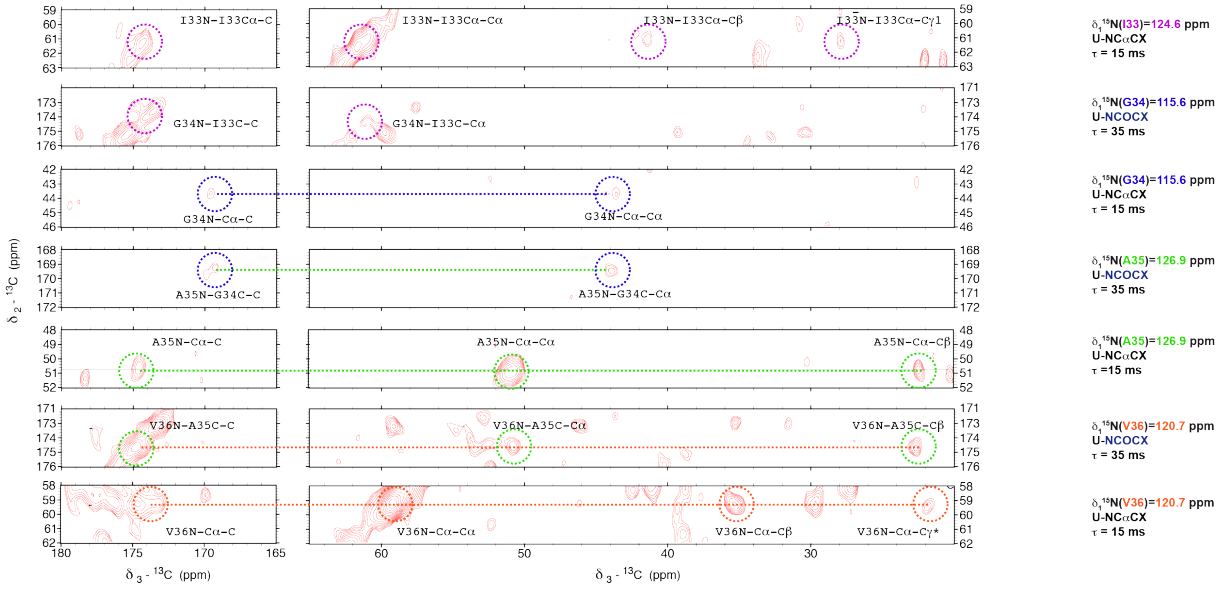

Figure 3.6: Strips from 3D NCOCX and NCACX spectra (35 and 15ms PDSD mixing times, respectively). Microcrystalline ϵ_{186}, pH 6.0, 3.2mm rotor.

An illustrative example of the sequential walk strategies is presented for the β-sheet section I33-G34-A35-V36 in figure 3.6. The sequential walk starts at δ^{15}N(I33) at 124.6 ppm and $\delta^{13}C\alpha$(I33) at 61.0 ppm obtained from the NCACX spectrum. The whole spin system of I33 present in the homonuclear correlation spectrum is confirmed, namely δ^{13}CO(I33) at 174.2 ppm, $\delta^{13}C\beta$(I33) at 41.3, $\delta^{13}C\gamma_1$(I33) at 27.6. In the NCOCX spectrum at the δ^{13}CO(I33) resonance of 174.2 ppm, the spin system of $(i-1)$th residue I33 can be identified at the δ^{15}N resonance at 115.6 ppm corresponding to the ith residue G34. In turn, the characteristic spin pattern of G34 can be identified in NCACX and NCOCX slices extracted at δ^{15}N(G34) ($\delta^{13}C\alpha$(G34) at 43.41 ppm and δ^{13}CO(G34) at 169.5 ppm).

Moving upwards in the chain, the same Cα and CO resonances are found in the NCOCX plane extracted at the δ^{15}N(A35) resonance at 126.9 ppm, confirming the sequential connectivity. The NCACX spectrum then shows the complete spin system of A35 (i.e. $\delta^{13}C\alpha$(A35) at 50.68 ppm and $\delta^{13}C\beta$(A35) at 22.36 ppm, previously identified in the PDSD spectrum) at the δ^{15}N(A35) at 126.9 ppm. These ^{13}C resonances are used to get the amide resonances of the $(i+1)$th aminoacid from the NCOCX 3D spectra, i.e. δ^{15}N(V36) at 120.7 ppm, which is in turn used to obtain the spin system resonances of V36 from NCACX spectrum, namely $\delta^{13}C\alpha$(V36) at 59.30, $\delta^{13}C\beta$(V36) at 35.25 ppm.

A second set of 3D spectra with long mixing times were then recorded in order to confirm the sequential assignment through the detection of long-range sequential ^{13}C-^{13}C contacts. These contacts may in addition yield important proximities defining secondary structure elements.

Representative strips are shown in figure 3.7. In this case the focus is on the A80 spin system, part of the α-helical region starting from T78 and ending at R91. Slices of both 3D spectra with short (35 ms) and long (80 ms) recoupling blocks are shown, namely at δ^{15}N(A80) = 117.0 ppm (NCACX) and δ^{15}N(E81) = 117.1 ppm (HNCOCX) respectively. In the NCACX spectra measured with long mixing time, an additional correlation corresponding to magnetization transfer to the (i+4)th residue in the chain can be found, namely $\delta^{13}C\alpha$(D84) = 55.93 ppm. Similarly, a cross peak can be seen in the NCOCX spectrum, corresponding to magnetization transfer to adiacent residue E81.

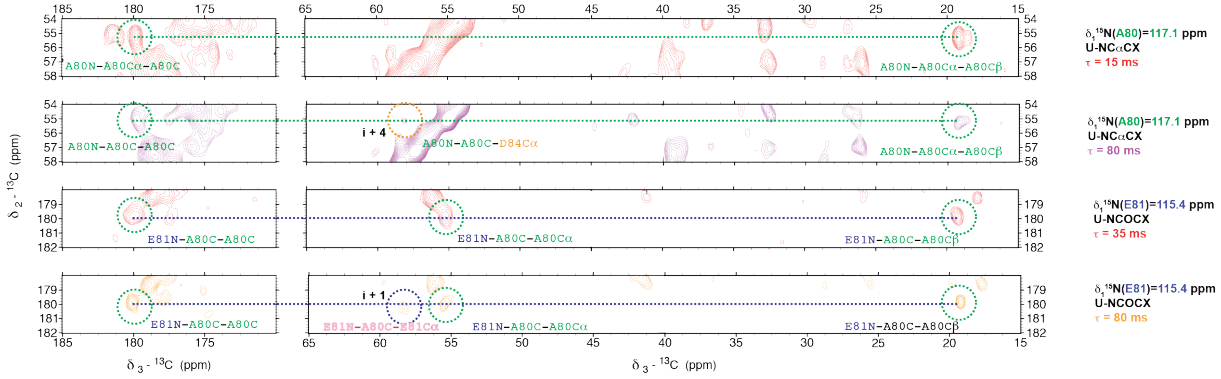

Figure 3.7: Comparison between 3D NCOCX/NCACX with short (35ms, in red) and long (80ms, in orange and purple respectively) PDSD mixing times.Microcrystalline ϵ_{186}, pH 6.0, 3.2mm rotor.

3.5.3 Assignment summary

The above procedure yielded assignment of 150 out of 186 residues (80%). As displayed in figure 4.15, unassigned residues reside in the unstructured termini and in regions which show high B-factors in the X-ray structure.

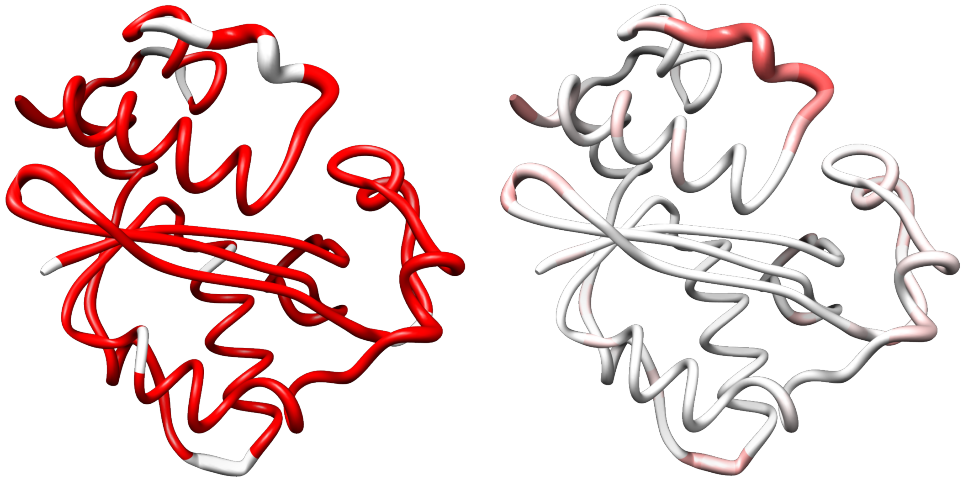

Figure 3.8: Cartoons of the X-ray single crystal structure of ϵ_{186} (PDB code 1J53), colored according to B-factors (left, from white to red for increasing B-factor), and by assigned residues (right, unassigned residues in white).

3.6 Conclusions

We have developed N-terminal domain of the ϵ subunit of *E. coli* DNA polymerase III (ϵ_{186}: 186 residues, 18 kDa) as a new model system for solid-state NMR.

Known crystallization conditions for ϵ_{186} were modified in order to decrease salt concentration in the mother liquor of the final sample. Solid-state NMR spectra of large proteins suffer particularly from resolution, and long acquisition times during 3D NCACX and NCOCX experiments are indispensable for the acquisition of resolved spectra. To this end, we have established screening methods adapted from X-ray crystallography protocols and suitable for obtaining high-resolution solid-state correlations. We have identified two distinct crystallization protocols for ϵ_{186} at pH 6.0 and 9.0, decreasing the final total salt concentration in the mother liquor from $\simeq$600 mM to $\simeq$100 mM.

Crystallization conditions at low salt were a key point for the application of ^{1}3C detected assignment strategies. One advantage of ^{13}C based assignment strategies at moderate MAS rates of 10 to 20 kHz is the application of spin diffusion for ^{13}C-^{13}C mixing in 2D ^{13}C-^{13}C and 3D ^{15}N-^{13}C-^{13}C experiments in which also amino acid side chains and especially structurally relevant methyl and aromatic carbons can be assigned.

The availability of an almost complete resonance assignment opens the way to a site-specific biophysical characterization of *E. coli* DNA polymerase. For example His 162 in the catalytic site of ϵ_{186} catalyzes the release of a hydroxyl species that serves as nucleophile. The protonation state of His 162 at pH 5.8 and 9 mimics the catalytic action of this residue, and in future studies the resonance assignment of His 162 could be used to develop methods for the analysis of histidine catalyzed enzymatic hydrolization.

Chapter 4

Solid-state NMR under ultra-fast MAS

Technical developments have played a mayor role in extending the applicability of solid-state NMR techniques to more and more challenging substrates, improving instrumental stability, sensitivity, and resolution.

In parallel, the development of MAS probes capable of achieving so-called fast (>30 kHz) and ultra-fast (>50 kHz) spinning rates has been revolutionizing this field [29, 57, 58, 59, 60, 61, 62], opening up several new perspectives in the analysis of a larger range of systems.

	outer diameter	inner diameter	volume	mass	max MAS rate
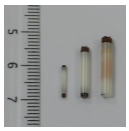	1.3 mm	0.9 mm	1.7 μL	1-4 mg	70 kHz
	2.5 mm	1.3 mm	8 μL	7-12 mg	35 kHz
	3.2 mm	2.2 mm	14 μL	15-20 mg	24 kHz

Table 4.1: Bruker rotor sizes and maximum MAS rates for solid-state NMR [63].

4.1 Decoupling during fast MAS

We have shown in figure 2.4 the intensity of the 2-(^{13}C)-L-alanine carbon signal under continuous wave (CW) heteronuclear decoupling as a function of the decoupling rf field strength. The efficiency of the dipolar averaging is generally proportional to the amplitude of the decoupling field, i.e., the corresponding nutation frequency $\nu_1 = \omega_1/2\pi$ in kHz. Under ultra-fast MAS, heteronuclear decoupling is efficiently performed with low-power irradiation [64, 65]. Long coherence lifetimes and highly resolved spectra can therefore be obtained without the negative effects of strong rf fields, even without the need for extensive deuteration.

This enables both an increase in resolution, by allowing longer acquisition times in direct and indirect dimensions of multidimensional correlations, and in sensitivity, by shortening the

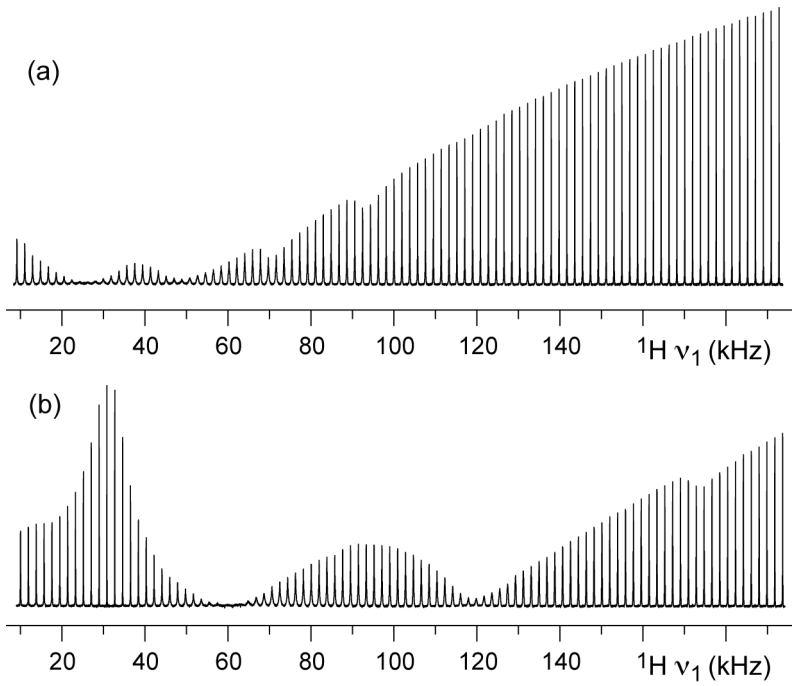

Figure 4.1: Intensity of the ^{13}C resonance in 2-(^{13}C)-L-alanine in a CP experiment at at (a) 25 and (b) 60 kHz MAS under CW ^{1}H decoupling, as a function of the decoupling rf-field strength. Data acquired on a Bruker Avance III spectrometer operating at a proton frequency of 500 MHz equipped with a double-resonance 1.3 mm CP-MAS probe.

interscan delays, without unwanted heating and subsequent deterioration of the sample [66]. In paramagnetic molecules, or in paramagnetically doped samples, combined with the short ^{1}H T_1s, this allows the repetition rate of the experiments to be significantly shortened, resulting in impressive sensitivity gains [67, 68]. An increase in the MAS rate has enabled the first acquisitions of resolved ^{1}H-detected spectra with high sensitivity, not only in perdeuterated molecules, but also in fully protonated substrates [69, 70, 71].

4.2 Selective cross-polarization (CP) in low-power experiments

All of the solid-state NMR studies on uniformly ^{13}C- and ^{15}N-labeled proteins rely on 2D or 3D homonuclear and heteronuclear experiments correlating ^{13}C, ^{15}N resonances. These experiments provide both the assignment of the resonances, and the constraints for the structural or dynamical determination [72].

Precise control of coherence transfer between groups of spins is essential in these studies to obtain unambiguous correlations. For example, in the quest for controlled transfers, a series of one-bond correlation experiments have been developed using J-coupling between neighboring nuclei [73, 74, 75, 76, 77, 78, 70, 79]. Another key method is the band-selective SPECIFIC-CP (spectrally induced filtering in combination with cross-polarization) experiment, which yields

sequential assignments by providing distinct N-CO and N-CA transfers along the protein backbone [80]. This experiment depends on the possibility on directing dipolar coherence transfer between N and C spins, based on the difference in the chemical shifts of the carbon resonances.

Analogs of the SPECIFIC-CP experiments for homonuclear ^{13}C correlations have so far only been proposed using selective pulses combined with phase-cycled z-filters after a broadband cross-polarization (CP) to remove undesired polarization from portions of the ^{13}C spectrum [81].

In the following, we demonstrate an approach that allows simple, band-selective ^{1}H-^{13}C CP. In turn, this enables the rapid acquisition of directed homonuclear ^{13}C-^{13}C 2D correlations with high sensitivity. This is demonstrated with the acquisition of a high-resolution aliphatic correlation of a microcrystalline sample of the paramagnetic, oxidized form of human superoxide dismutase (SOD) [82], and with the acquisition of a high-resolution CO-Cα correlation for the protein domain GB1 [35].

At conventional MAS frequencies, ^{1}H-^{13}C CP is intrinsically broadband, with the whole proton bath being in contact with all the carbons [83, 84]. Selective transfer would require low-power irradiation on ^{13}C resonances. Low power CP has indeed been considered with success in solution NMR [85]. In solids, due to the overlap of several broad zero-quantum (ZQ) and double-quantum (DQ) Hartman-Hahn matching conditions [86, 87, 58], low-power irradiation entails a substantial price in the transfer efficiency.

Ultra-fast (>60 kHz) MAS rates enter a regime where homonuclear ^{1}H-^{1}H couplings are efficiently averaged [66] and DQ and ZQ matching conditions become well spaced. In this regime, broadband CP could be achieved using low rf amplitudes [58].

In most CP studies until now, with spinning rates up to 30 kHz, the best CP transfers have always been obtained with high-power ^{1}H irradiation. Low-power schemes performed poorly in this regime, although fields of a few kHz should in principle be sufficient to lock ^{1}H and ^{13}C magnetization and drive the polarization transfer process. On the contrary, at the high rotation frequencies used in the experiments presented, comparable transfer efficiencies are found for the high-power regime and for the low-power n=1 DQ CP condition.

Figure 4.2 (a) shows this for the classic case where the rf fields are significantly larger that the rotor frequency. Only ZQ transitions are observed in the CP profile. If weak rf fields are used with slow (here 10 kHz) spinning, overlapping ZQ and DQ transitions would lead to partial cancellation of the transferred polarization, and the overall efficiency would be reduced.

This behavior changes substantially in the ultra-fast MAS regime. Here, first the Hartman-Hahn matchings are considerably sharper and, second, their spacing is substantially larger. As shown in figure 4.2 (b), this allows overlap of ZQ and DQ transitions to be easily avoided for both high and low values of ω_1^H.

As a result, ultra-fast MAS rates allow efficient low-power CP experiments using low power on both channels, as verified by the experiments shown in [58]. This situation is now reminiscent of the CP behavior observed at moderate spinning speeds on low-gamma nuclei such as ^{15}N-^{13}C pairs [80].

Here we show that band-selective ^{1}H-^{13}C CP transfer can be achieved using either ZQ or

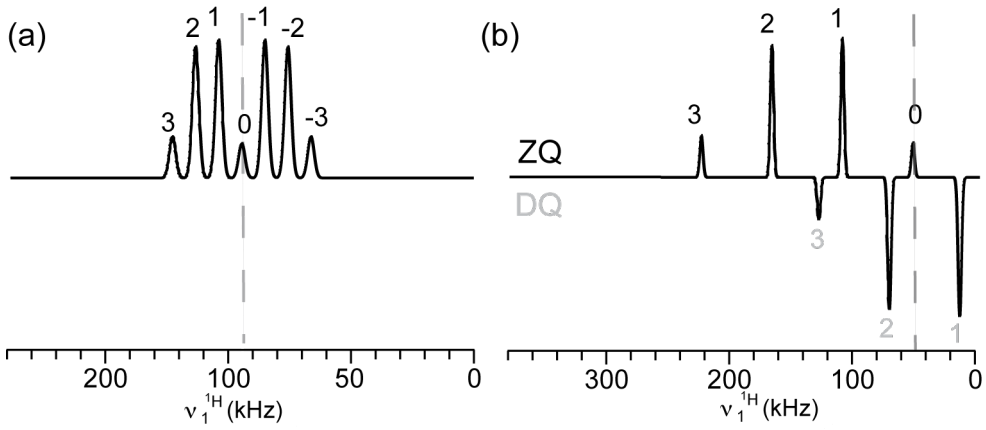

Figure 4.2: Schematic explanation of cross-polarization occurring under low spinning speed at high irradiation fields (a) or under ultra-fast MAS at low fields (b).

DQ matching conditions if careful attention is paid to the choice of rf field amplitudes and ^{13}C carrier. In particular, if the carrier is placed on the CO or the aliphatic ^{13}C regions, and the matching condition is chosen so that the ^{13}C amplitude is smaller than the frequency differences, then perfectly selective CP is achieved with no loss in sensitivity.

Figure 4.3 shows an investigation of optimal conditions for band-selective ^{1}H-^{13}C CP to the carbonyl and aliphatic carbons of fully-(^{15}N,^{13}C)-labeled, oxidized human SOD. Figure 4.3(a) shows the HH profiles obtained by varying the proton rf-field strength $\omega_H/2\pi$ from 130 to 5 kHz while keeping the carbon field amplitude fixed either at low ($\omega_C/2\pi$= 14 kHz) or at relatively high values ($\omega_C/2\pi$= 100 kHz). In each profile, ZQ and DQ Hartmann-Hahn conditions show positive and negative intensity, respectively, as previously shown [86]. Figure 4.3(b-e) compares the whole ^{13}C spectra of SOD recorded for the low carbon field DQ condition at 60 kHz MAS with ordinary broadband, ZQ CP spectra. Highly specific ^{1}H-^{13}C CP transfers to the CO or to the ^{13}C aliphatic could be recorded with carbon and proton fields of 15 and 45 kHz, and a carbon carrier placed at 176 and 40 ppm, respectively. Finally, the selectivity does not involve a compromise in sensitivity. On the contrary, in the broadband scheme, spin diffusion and dipolar truncation effects yield less efficient CP for carbonyl, which experience a relatively weak dipolar coupling to protons. For these nuclei, the low power conditions bring a substantial enhancement of intensity (in this case, there is a factor of about 2 in the integral of the CO region between figure 4.3(d) and (b), as the polarization transfer does not suffer from the simultaneous CP process occurring to the aliphatic carbons.

Capitalizing on these effects, figure 4.4 shows the application of the band-selective ^{1}H-^{13}C CP scheme implemented as part of 2D homonuclear ^{13}C-^{13}C correlation experiments on micro-crystalline protein samples. Here, long experimental times are routinely required for sampling the large spectral widths that include all the carbon resonances, while much of the information is often contained in small regions of the spectrum (CO-Cα, or C^{aliph}-C^{aliph}). The selectivity pro-

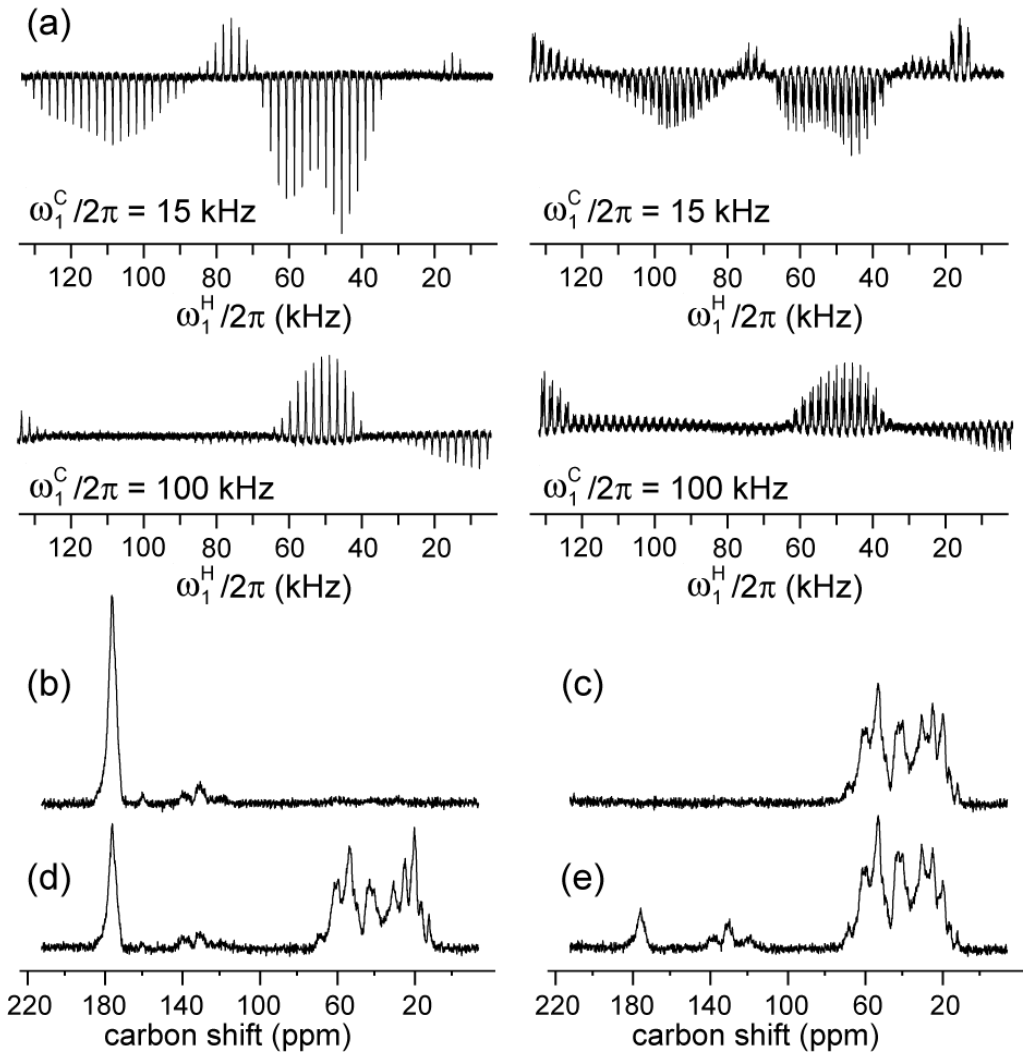

Figure 4.3: ^{13}C spectra of (^{15}N,^{13}C)-labeled SOD recorded at 60 kHz MAS. (a) Matching profiles for specific (upper panels) and broadband (lower panels) CP. Intensity of the CO carbon signal (left panels) and of the aliphatic carbon signals (right panels) at variable proton rf-field strength. In the two upper panels, the carbon rf-field strength $\omega_{1C}/2\pi$ is 15 kHz and the ^{13}C carrier Ω_C is 176 (right) and 40 ppm (left), respectively. In the two lower panels, the ^{13}C rf-field strength $\omega_{1C}/2\pi$ is 100 kHz, and the ^{13}C carrier is placed at 100 ppm. (b-e) Comparison between a specific CP transfer to CO carbons (b, Ω_C= 176 ppm, $\omega_C/2\pi$= 14 kHz, $\omega_H/2\pi$ = 46 kHz, 1.5 ms contact time), a specific CP to aliphatic carbons (c, Ω_C= 35 ppm, $\omega_C/2\pi$= 14 kHz, $\omega_H/2\pi$ = 46 kHz, 1.35 ms contact time), and two conventional non-selective, high-power CPs (d-e, Ω_C= 100 ppm, $\omega_C/2\pi$= 100 kHz, $\omega_H/2\pi$=40 kHz, 4.9 ms and 750 μs contact times to yield a maximum CO and aliphatic ^{13}C signal, respectively). All experiments were performed on a Bruker Avance III spectrometer operating at a proton frequency of 900 MHz, and equipped with a double-resonance 1.3 mm CP-MAS probe.

vided by the low-power CP scheme allows reducing the spectral width in the indirect dimension without the drawbacks connected to folding.

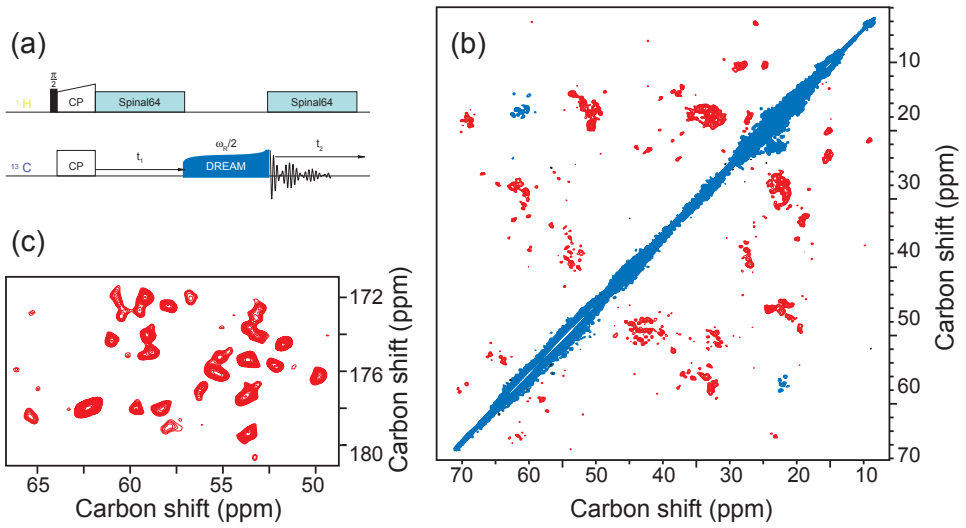

Figure 4.4: (a) Band-selective DREAM pulse sequence. (b-c) DREAM [88] correlation spectra at 60 kHz MAS: (b) C^{aliph}-C^{aliph} spectrum of paramagnetic SOD (the CO region is empty) (CP on aliphatic carbons, Ω_C = 35 ppm, $\omega_{1_{13C}}/2\pi$ = 14 kHz, $\omega_{1_H}/2\pi$ = 46 kHz, contact time 1500 μs, mixing time 5 ms, 384 scans, 0.5 s interscan delay, 300 t_1 increments, t_{1MAX}=10 ms, t_{2MAX}=20 ms, total time = 17 h) and (c) CO-Cα spectrum of GB1 (CP on carbonyls, Ω_C = 176 ppm during CP and 105 ppm during the rest of the experiment, $\omega_{1_{13C}}/2\pi$ = 14 kHz, $\omega_{1_H}/2\pi$ = 46 kHz, contact time 350 μs, mixing time 5ms, 192 scans, 2 s interscan delay, 80 t_1 increments, t_{1MAX}=10 ms, t_{2MAX}=20 ms, total time = 8.5 h). XiX proton-decoupling [89, 67] (ω_{1_H}= 13 kHz, τ_p= 70 μs) was used in direct and indirect acquisition. Under these conditions we predominantly see one bond tranfers. The two microcrystalline samples each containing about 1 mg of the ^{13}C, ^{15}N-labeled proteins were prepared as previously described [82, 35], and directly centrifuged into the NMR rotor.

Figure 4.4(b) shows a C^{aliph}-C^{aliph}-selective DREAM experiment performed on SOD. The DREAM scheme described previously [88] was preceded by an aliphatic-selective ^{1}H-^{13}C CP. Notably, in addition to the selectivity of the transfer, the low powers used for both CP and ^{1}H decoupling allow a reduction in the probe duty cycle and limits sample heating. This in turn enables the use of fast recycle delays if the ^{1}H T_1s are suitably short [58, 90]. Figure 4.4(c) shows the CO-Cα selective DREAM experiment performed on fully-(^{15}N,^{13}C)-labeled GB1. Here, the narrow CO indirect dimension can be sampled with only a few t1 increments in a particularly short time. This is, for example, extremely useful in experiments to quickly screen protein preparations in solids in the same way that ^{1}H,^{15}N-HSQC experiments are used in liquids.

4.3 Through-bond transfers

Under ultra-fast MAS, heteronuclear decoupling is efficiently performed with low-power irradiation and long coherence lifetimes can be obtained without the negative effects of strong radio-frequency (rf) fields. In this context, the exploitation of J-transfer based correlation experiments [91, 70, 92, 93, 78, 94, 95, 79, 96, 97].where long evolution delays are necessary for creating and refocusing coherences between neighboring spins, becomes increasingly pertinent [98].

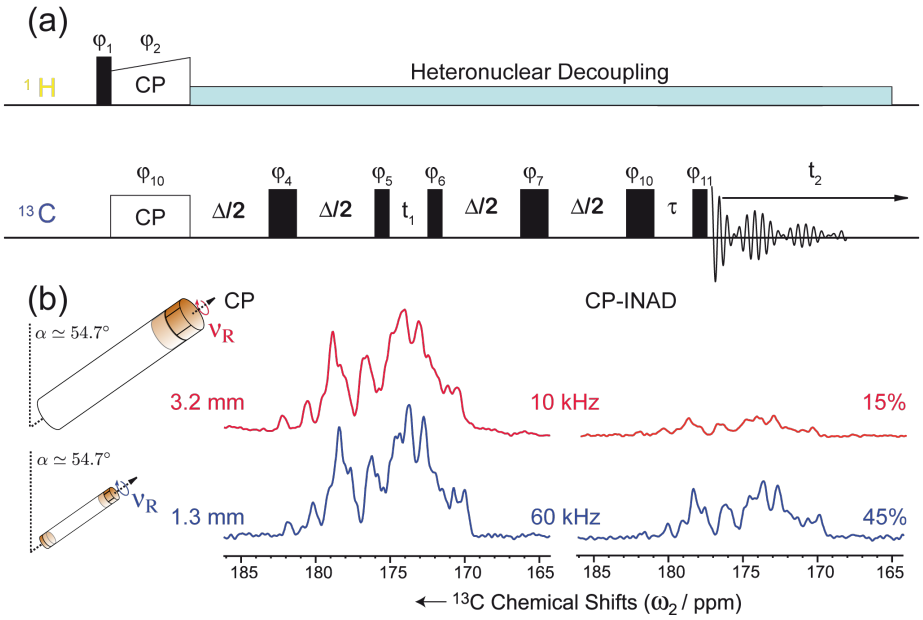

Figure 4.5: (a) Pulse sequence for the DQ-INADEQUATE experiment, and (b) efficiency of the DQ-INADEQUATE experiment (right) as compared to CP (left) for microcrystalline GB1 at ν_R=10 kHz MAS (high-power -80 kHz- SPINAL-64 decoupling [37]) and ν_R=60 kHz MAS (low-power -15 kHz- slpTPPM decoupling [36]). Percentages refer to relative peak heights.

Figure 4.6 (a) demonstrates how J-scalar transfer efficiency grows at ultra-fast MAS as a result of the longer coherence lifetimes. This figure compares the performance of cross-polarization (CP) transfers to CP-refocused-INADEQUATE experiments [33, 34] for the CO resonances of the microcrystalline protein domain GB1 [35]. A significant increase of the coherence lifetimes of both the CO and Cα spins is observed moving from 10 kHz MAS (e.g. coherence lifetimes T_2' of 12.8 ms for the CO spins under 80 kHz SPINAL-64 [37] decoupling), to 60 kHz MAS under low-power decoupling (e.g. coherence lifetimes T_2' of 86 ms for the CO spins under 15 kHz swept low-power TPPM (slpTPPM) decoupling42). Consequently, the efficiency of the through-bond transfers is significantly increased from 15 to 45%, thus rendering this kind of experiment a competitive alternative to dipolar-based schemes not only in perdeuterated molecules [38], but also in fully protonated substrates.

In parallel, resolution is also a key barrier to opening the door to solid-state NMR towards increasingly complex biological samples. A variety of J-decoupling techniques have recently been

proposed to remove the scalar splitting between neighboring ^{13}C spins [39, 99], which significantly affect the spectral resolution in fully ^{13}C-labelled systems [71, 94, 99, 100, 101, 102, 103]. Here we introduce a new experiment which simultaneously improves the performance of through-bond transfers and accomplishes virtual homonuclear J-decoupling. As illustrated in figure 4.6 (a), this is achieved by incorporating the S^{3}E scheme [39, 40, 103] (Spin State Selective Excitation) into the INADEQUATE after the evolution of the DQ coherences.

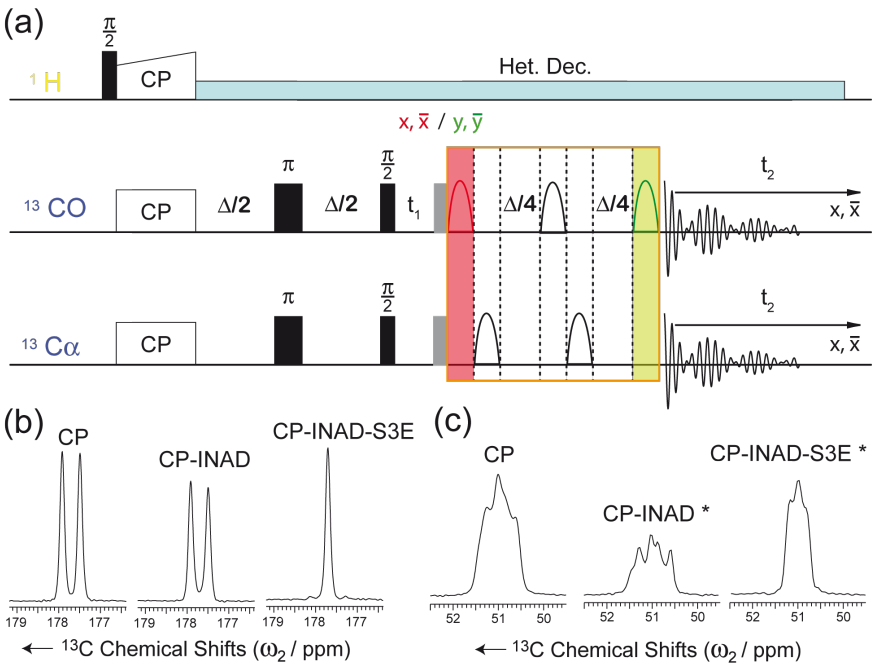

Figure 4.6: (a) Pulse sequence for the band-selective refocused INADEQUATE-S^{3}E experiment. The bell shapes represent the band-selective π pulses and the delta $\Delta/4$ is set to 1/8J. For each t_1 increment, two FIDs are recorded, with a CO selective π pulse placed either at the end (in green) or at the beginning (in red) of the refocusing block, together with a suitable phase cycle of the second $\pi/2$ hard pulse (grey rectangle) and the receiver. (b-c) Relative efficiency of CP (left), INADEQUATE (center), and INADEQUATE-S^{3}E (right) recorded on CO (b) and Cα (c) resonances of fully ^{13}C-labeled L-Alanine, at 60 kHz MAS and low-power slpTPPM decoupling ($\omega_1^H/2\pi \simeq \nu_R/4$=13.6 kHz according to pulse calibration). The Cα INADEQUATE signals ($\star$) were extracted from selective 2D INADEQUATE experiments, so that only CO magnetization was excited at the CP step.

This block allows recovery of in-phase signals efficiently by partial inter-conversion between in-phase and antiphase components, without the need of complete refocusing of antiphase coherences. This requires half of the time (1/4J i.e. 4.5 ms for a $J_{COCA} = 55$ Hz) of the reconversion block for corresponding refocused INADEQUATE, minimizing the duration of the pulse sequence and the relative losses due to transverse decay. Additionally, it provides the two individual doublet components separately, which can then be combined into a single, more intense signal simultaneously removing the J-splitting and increasing the overall signal to noise by a further

factor 1.4 [40]. It is noteworthy that, in contrast to the previous implementation in NCO or NCA experiments, where the S^3E element was appended to the end of the pulse sequence [103], the S^3E block here replaces the conventional refocusing periods of the INADEQUATE experiments. This pulse scheme represents therefore the shortest in-phase J-based correlation experiment designed so far, which results in minimal loss of sensitivity through transverse dephasing. Finally, this scheme mutually decouples the two spins from each other, leading to an increase of resolution and sensitivity on both spins. As illustrated in figure 4.6 (c and d) for [U-^{13}C]-L-Alanine, sensitivity gains (as measured by the relative peak heights) of factors of 1.4 (CO) and 2.0 (Cα) are observed when the S^3E block is used instead of the conventional refocusing period in an INADEQUATE experiment. Interestingly, in this new experiment, the CO peak height after the through-bond transfer is actually more intense than that of each component of the doublet acquired straight after CP.

The scheme lends itself beautifully to the investigation of large biological solids at high-fields and ultra-fast MAS. Figure 4.7 shows the carbonyl region of a 2D INADEQUATE-S^3E experiment recorded on microcrystalline oxidized superoxide dismutase (SOD), a dimeric paramagnetic enzyme of 32 kDa [82] recorded with 60 kHz MAS on an 850 MHz spectrometer. As a consequence of the shorter refocusing period, for most of the signals the sensitivity gain exceeds the limit of 1.4, provided by the simple combination of the two doublet components: the incorporation of the S^3E block yields a gain both in resolution, removing all the 55 Hz one-bond J_{COCA} couplings, and in sensitivity, up to a factor 1.8. This is illustrated by the traces in figure 4.7 (b). Notably, conventional refocused INADEQUATE spectra of comparable S/N, with dramatically reduced resolution, can typically be acquired under slow MAS, in over double the time with a 10-fold larger amount of sample.

Beside providing an unambiguous identification of resonances, through-bond correlation methods in solids are tools to investigate structural disorder [98]. The higher resolution provided by the S^3E implementation of the INADEQUATE experiment under ultra-fast MAS is a new tool to highlight this same kind of effect in a microcrystalline protein, and to potentially observe the detailed structure of the correlation peaks in analogy to disordered organic solids. The corresponding spectrum recorded on a well-defined polymorph of microcrystalline protein domain GB1 (form A)56 indeed displays lineshapes with peculiar fine structures, which are the signature of correlated distributions of isotropic shift frequencies associated with slight static structural disorder around each crystallographically equivalent molecule. In addition, as compared to the inhomogeneouly broadened signal, in this spectrum, individual cross sections feature increased resolution (figure 4.8), with a further narrowing of the linewidth.

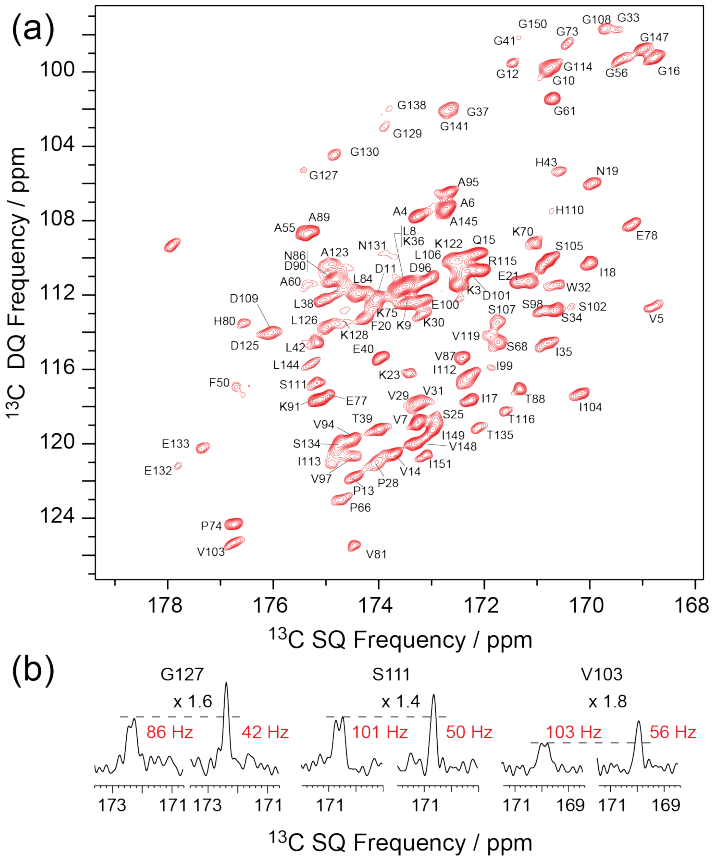

Figure 4.7: (a) Carbonyl region of a band-selective INADEQUATE-S^{3}E recorded at ν_R=60 kHz MAS on dimeric oxidized SOD. (b) Traces of 2D INADEQUATE spectra acquired using the conventional refocusing period (left) and the S^{3}E block (right). The gains in sensitivity are respectively 1.6, 1.4 and 1.8.

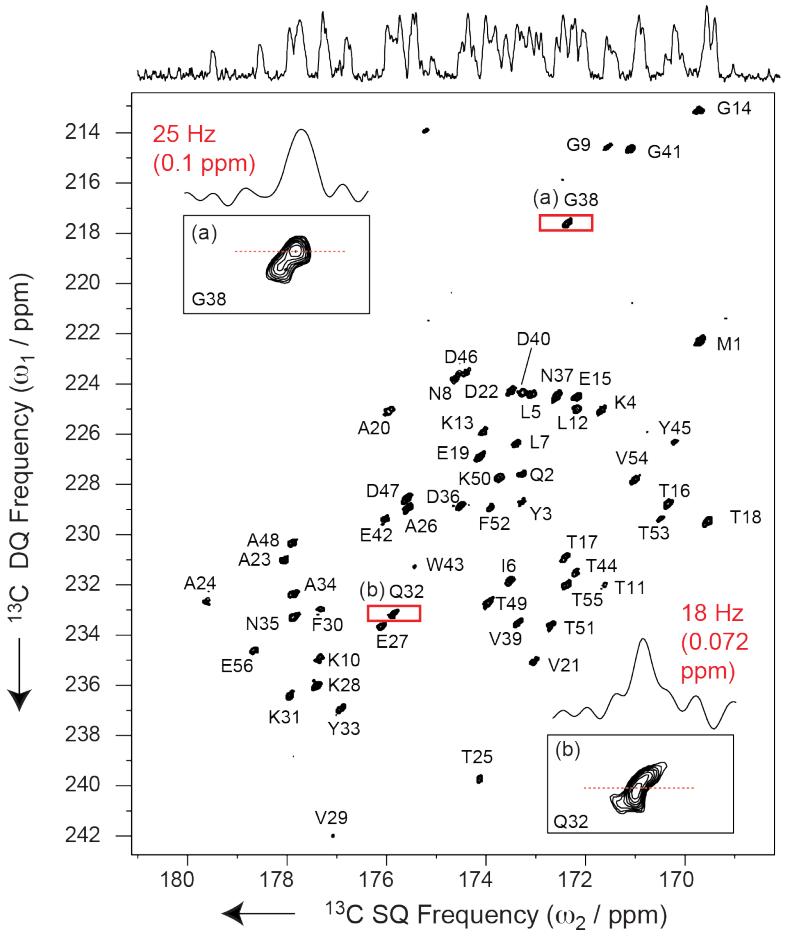

Figure 4.8: Carbonyl region of a band-selective INADEQUATE-S^{3}E spectrum of microcrystalline GB140 recorded at ν_R=60 kHz MAS on a 1000 MHz Bruker Avance III spectrometer.

4.4 ^{1}H detection in fully-protonated proteins

Solution-state structural investigations of proteins traditionally use the detection of protons, which, with their high gyromagnetic ratio, usually provide the best possible sensitivity [104, 105], whereas for fully-protonated samples in the solid state the large homonuclear ^{1}H dipolar couplings result in linewidths that are prohibitive to constructive use. For this reason, solid-state NMR studies of biomolecules are traditionally performed by directly detecting ^{13}C which has lower sensitivity due to the smaller gyromagnetic ratio, but significantly higher resolution.

The use of perdeuterated proteins has very recently opened the way to highly sensitive proton-detected solid-state NMR experiments by weakening the dipolar interactions between protons [104, 105]. At moderate MAS rates, amide sites must be only partially re-protonated (typically using back-exchange levels of 10-30%) to accomplish acceptable dilution of the proton bath and yield well-resolved ^{1}H spectra [106, 107].

The potential advantage of higher sensitivity is thus compromised to gain resolution, and this renders the determination of internuclear distances impractical, with few exceptions [108, 109, 57]. We have recently shown how this problem can be completely overcome by using 100% re-protonation of exchangeable sites, without loss of resolution, if perdeuteration is combined with ultra-fast MAS (60 kHz) at high magnetic fields. Well-resolved "fingerprint" spectra may then be acquired rapidly [110, 111], enabling faster resonance assignment and the detection of a range of structurally important parameters [110, 112].

Complete deuteration of proteins, however, requires laborious and expensive expression protocols, which affect the production yields and are not viable at all for some expression systems [113, 114]. In addition, the subsequent re-protonation of exchangeable sites in the interior of the protein depends on transient unfolding of the protein, which is not feasible for proteins that unfold irreversibly. Clearly, protonated proteins are the ideal targets, to improve sensitivity, provide a generally viable assignment strategy and measure ^{1}H-^{1}H distances. Measuring ^{1}H-detected spectra on protonated proteins in the solid state has only been reported for one small model protein (GB1, 56 residues) in microcrystalline form [57]. In this pioneering work, Rienstra and coworkers used ^{1}H-detection schemes to obtain fast assignments of backbone amide and HA protons with the prior knowledge of ^{15}N and ^{13}C backbone shifts.

Here we show that the use of high magnetic fields and ultra-fast MAS allows narrow ^{1}H line widths to be achieved from significantly larger fully-protonated proteins even in a non-crystalline precipitate, without any need for dilution in a deuterated background. We demonstrate that this provides a route to the extensive, robust and expeditious assignment of the backbone ^{1}H, ^{15}N, ^{13}CA and ^{13}CO resonances based on ^{1}H detection of fully protonated medium-sized proteins. Pulse sequences for these ^{1}H-detected correlations are shown in figure 4.9.

Figure 4.10 shows the ^{1}H-detected dipolar HN correlation of two [^{13}C,^{15}N]-labeled and fully-protonated protein domains from the E. coli DNA replisome [51] acquired at high magnetic field (800 MHz) under ultra-fast MAS (60 kHz). The first sample is a microcrystalline form of ϵ_{186} (20 kDa) [54] and the second is a gel-like precipitate of the tetrameric single-stranded DNA-binding

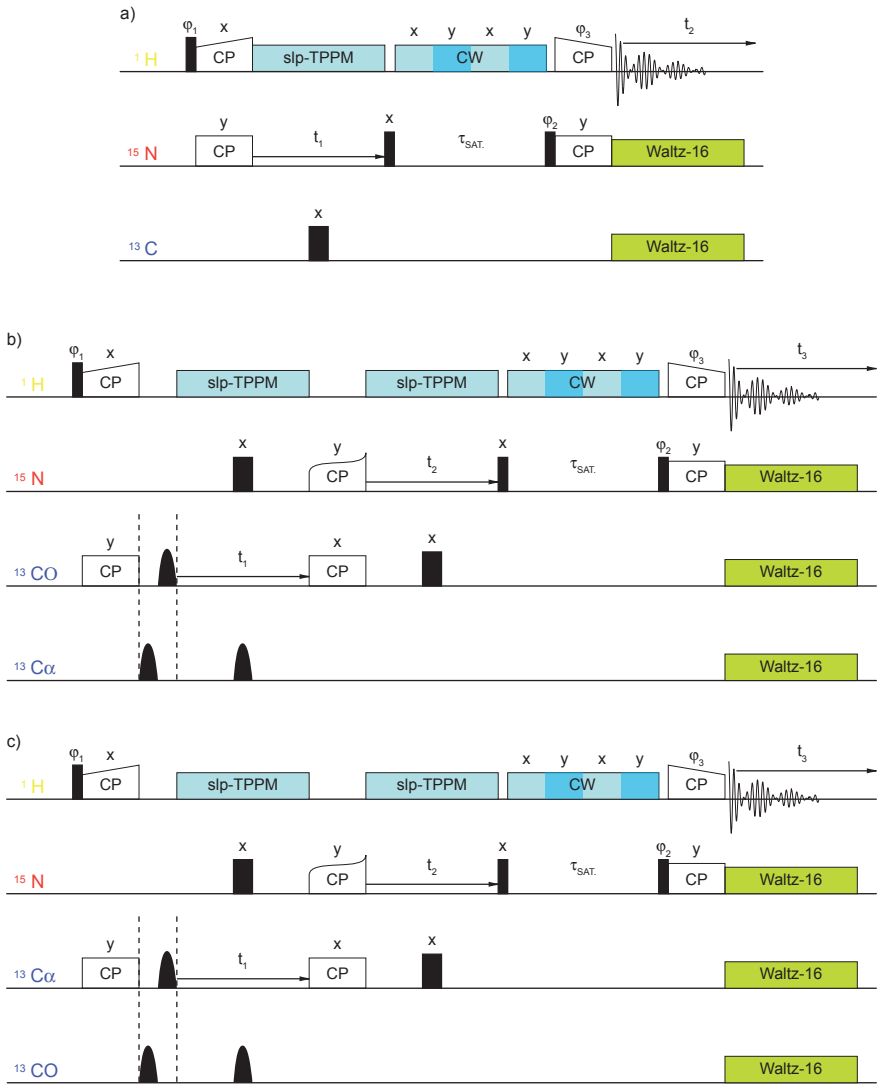

Figure 4.9: Pulse sequences used in proton-detected experiments. (a) HN correlation, in which both magnetization transfer steps are accomplished using cross-polarization; b) 3D (H)CONH; (c) (H)CANH. Narrow and broad black rectangles indicate 90° and 180° pulses respectively, the bell shapes represent band selective π-pulses. For CP steps between ^{1}H and ^{15}N or between ^{1}H and ^{13}C, linearly ramped pulses were applied on the ^{1}H channel. Tangentially ramped pulses [51] were applied to ^{15}N during CP from ^{13}C. The phase cycle φ_1 was {y,-y}, φ_2 was {x,x,-x,-x}, φ_3 was {4*y,4*-y}; the receiver phase cycle was {y,-y,-y,y,-y,y,y,-y}.

protein (SSB, 4 x 18 kDa) [115]. While the ^{1}H resonances have, as expected, significantly shorter coherence lifetimes than in deuterated analogs (T_2' values of 1.5 vs 10 ms), the actual apparent line widths are typically only about two-fold larger (225 ± 75 Hz). Notably, both spectra display similar ^{1}H line widths, despite their different molecular weight and aggregation state. This level of resolution is not sufficient to yield a fully resolved fingerprint spectrum in 2D, but we show

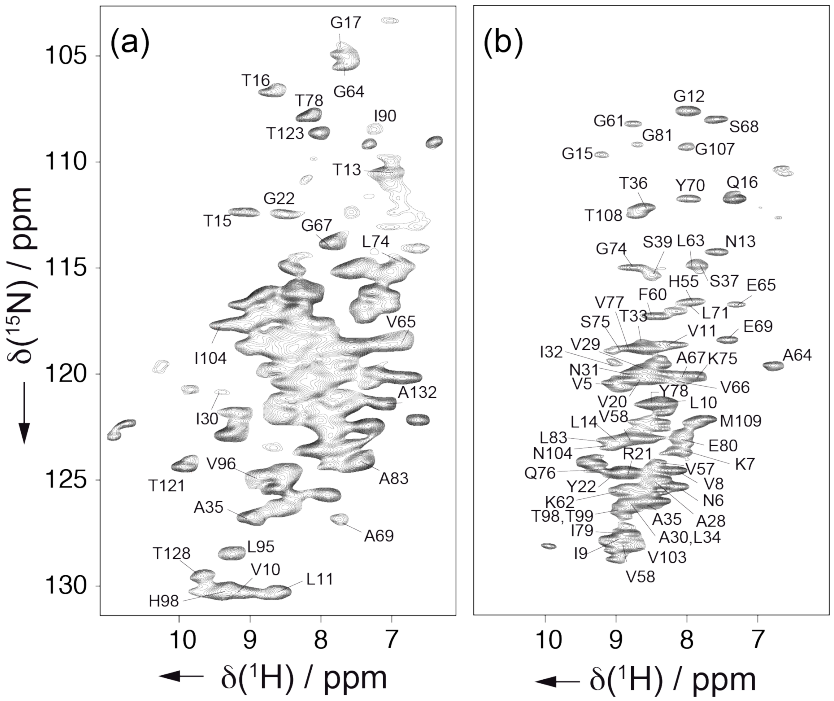

Figure 4.10: (a-b) Proton-detected HN correlation spectra. (a) [^{13}C,^{15}N]-ϵ_{186} from E. coli DNA polymerase III and (b) E. coli [^{13}C,^{15}N]-SSB, at a ^{1}H NMR frequency of 800 MHz and 60 kHz MAS. The pulse sequence for these ^{1}H-detected correlations is shown in figure 4.9 (a).

here that all the protein resonances can be resolved when the ^{1}H-^{15}N correlation experiment is coupled to a third ^{13}C dimension, and that the larger ^{1}H line widths do not render the 3D experiments unfeasible.

Figure 4.11 shows ^{15}N-^{13}CO and ^{15}N-^{13}CA projections of 3D (H)CANH and (H)CONH correlations. As we saw in the previous section, CPs become efficient under low-power irradiation on the ^{1}H channel, and a typical matching at 60 kHz MAS is 10-20 kHz on ^{1}H, with 40-50 kHz on ^{13}C. Usually, under these conditions, at high-field, if the offset is placed on the CO or the aliphatic ^{13}C regions, and the matching condition is chosen so that the ^{13}C amplitude is smaller than the frequency differences, the CP transfer is perfectly selective to a specific part of the carbon spectrum. Overall, these spectra yield correlations where the amide ^{1}H and ^{15}N shifts of residue i are correlated to either the ^{13}CO of the preceding residue (i-1), or the ^{13}CA shifts of the same residue i. These 3D spectra combine favorable line widths of ^{15}N and ^{13}C in the indirect dimensions and sensitive ^{1}H detection, and can be acquired in remarkably short experimental times (17-34 hours). 132 CANH and 133 CONH correlations were observed for ϵ_{186}, and 71 CANH and 66 CONH signals for SSB. In both samples, the detected signals represent more than 85% of residues located in the structured regions of the proteins. Conversely, no signals were observed for the intrinsically disordered C-terminal domain of SSB (residues 112-178) [115] or in loops with high B-factors in the crystal structures (e.g. residues 1-8, 152-162 in ϵ_{186}, and

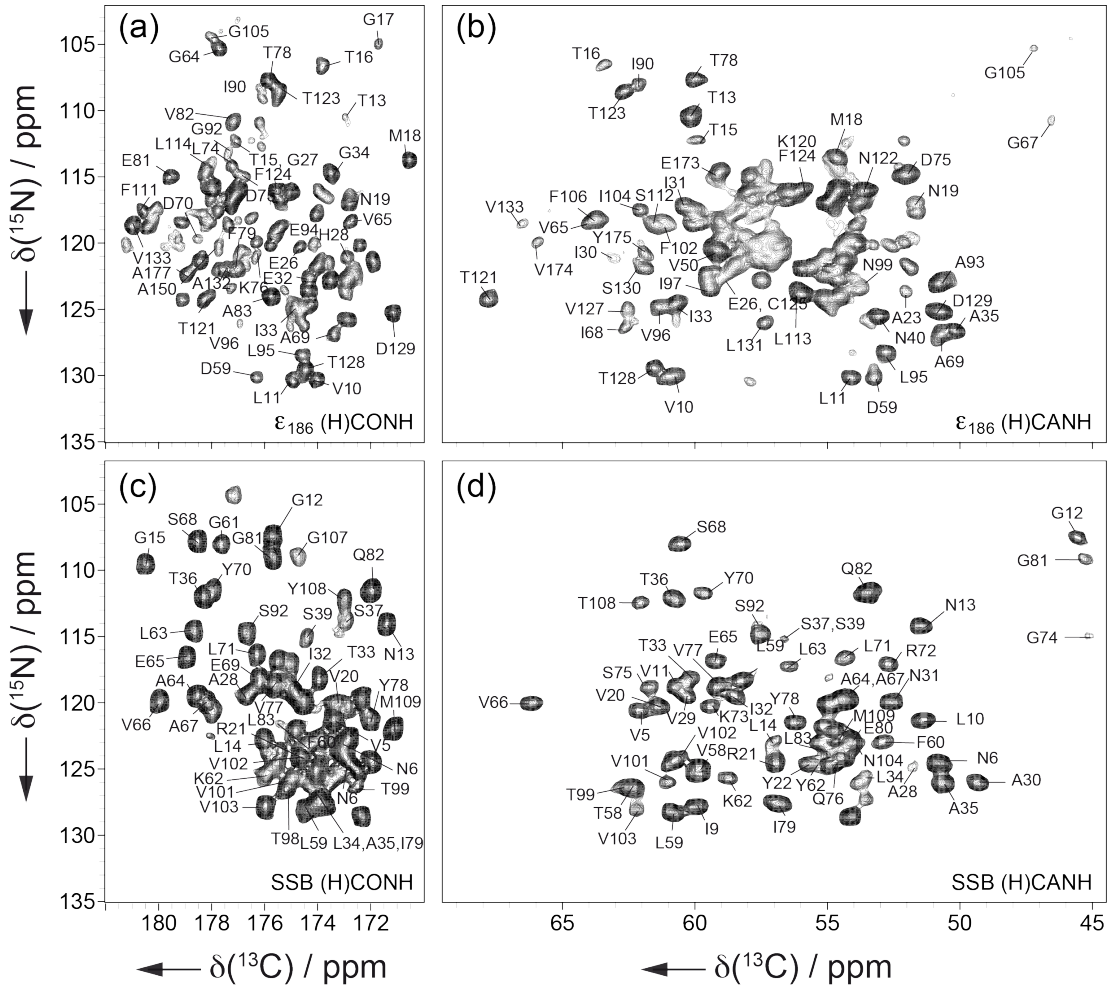

Figure 4.11: Proton-detected correlation spectra of [^{13}C,^{15}N]-ϵ_{186} (a-b) and [^{13}C,^{15}N]-SSB (c-d), recorded on a 800 MHz NMR spectrometer at 60 kHz MAS. (a) and (c) show assigned ^{13}C-^{15}N projections of 3D (H)CONH spectra, while (b) and (d) show corresponding projections of 3D (H)CANH spectra. Pulse sequences for these ^{1}H-detected correlations are shown in figure 4.9 (b) and (c) respectively.

22-27, 40-49, 86-90 in SSB [115].

4.5 ^{1}H-detected 3D experiment for sequential resonance assignment in fully-protonated proteins

Similar to the solution-state case, the resolving power of the ^{1}H dimension can be further exploited for sequential resonance assignment. Here, two additional 3D experiments were employed, which combine the HN dipolar correlation module with ^{13}C-^{13}C through-bond (scalar) transfers, providing complementary pairs of inter- and intra-residue CO/CANH correlations (figure 4.12).

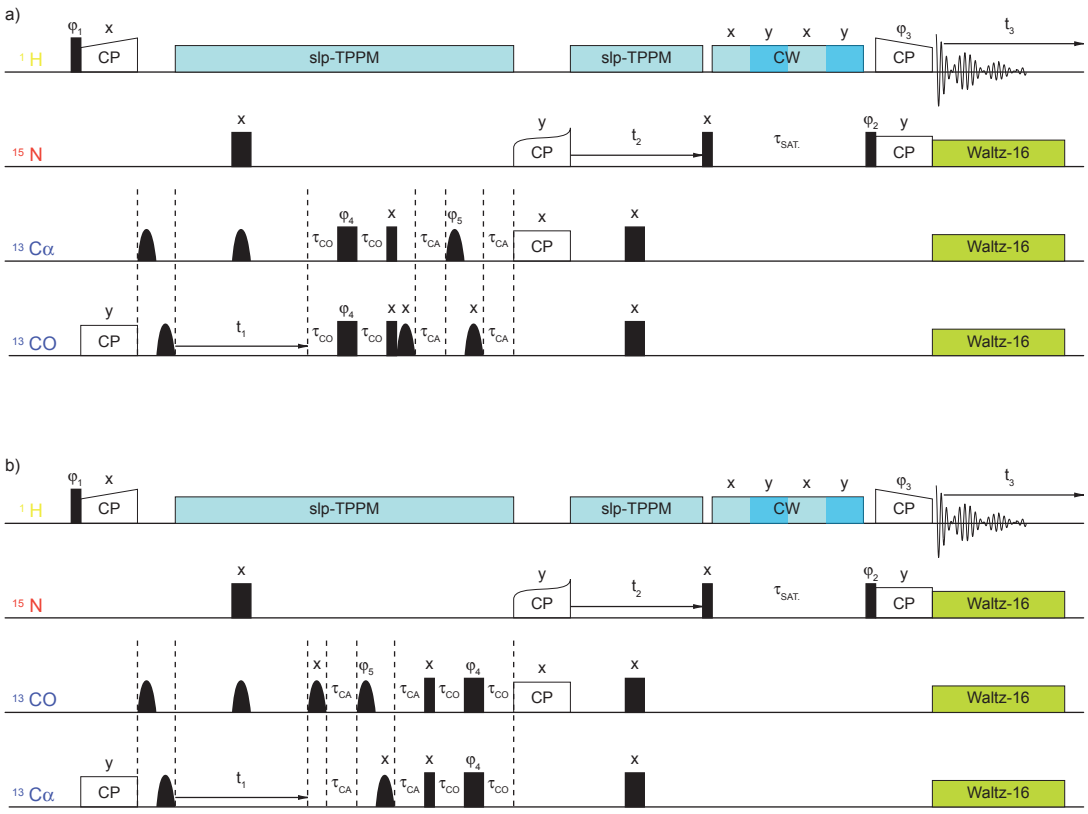

Figure 4.12: Pulse sequences used for proton-detected inter-residue correlations. (a) 3D (H)CO(CA)NH; (b) 3D (H)CA(CO)NH. Narrow and broad black rectangles indicate 90° and 180° pulses respectively, the bell shapes represent band selective π-pulses, and the delays τ_{CO} and τ_{CA} were set to 4 and 3 ms, respectively (close to the 4.7 ms optimal for $J_{COCA} = 53$ Hz). For CP steps between ^{1}H and ^{15}N or between ^{1}H and ^{13}C, linearly ramped pulses were applied on the ^{1}H channel. Tangentially ramped pulses [116] were applied to ^{15}N during CP from ^{13}C. The phase cycle φ_1 was {y,-y}, φ_2 was {x,x,-x,-x}, φ_3 was {4*y,4*-y}, φ_4 was {4*x,4*y}, φ_5 was {8*x,8*y} and φ_6 was {4*x,4*y,4*-x,4*-y}; the receiver phase cycle was {y,-y,-y,y,-y,y,y,-y,-y,y,y,-y,y,-y,-y,y}.

These (H)CO(CA)NH and (H)CA(CO)NH sequences were developed in the context of resonance assignment of fully-deuterated 100% back-exchanged samples [110] and yield maps where the amide ^{1}H and ^{15}N shifts of residue i are correlated to either the ^{13}CO of the same residue or to the ^{13}CA of the preceding residue, respectively. Long coherence lifetimes are key to successful J-based correlation experiments [33, 93]. Our present data show that fully protonated samples feature remarkably long ^{13}C and ^{15}N coherence lifetimes, of the order of 40 ms for ^{13}CO and ^{15}N (i.e. comparable to those typically observed in deuterated, 100% back-exchanged preparations), and about 12.5 ms for ^{13}CA [117, 118]. Therefore, the through-bond INEPT block has a transfer efficiency of about 30% between the Cα and CO spins even in these fully protonated samples, and thus provides a competitive alternative to dipolar-based methods under ultra-fast

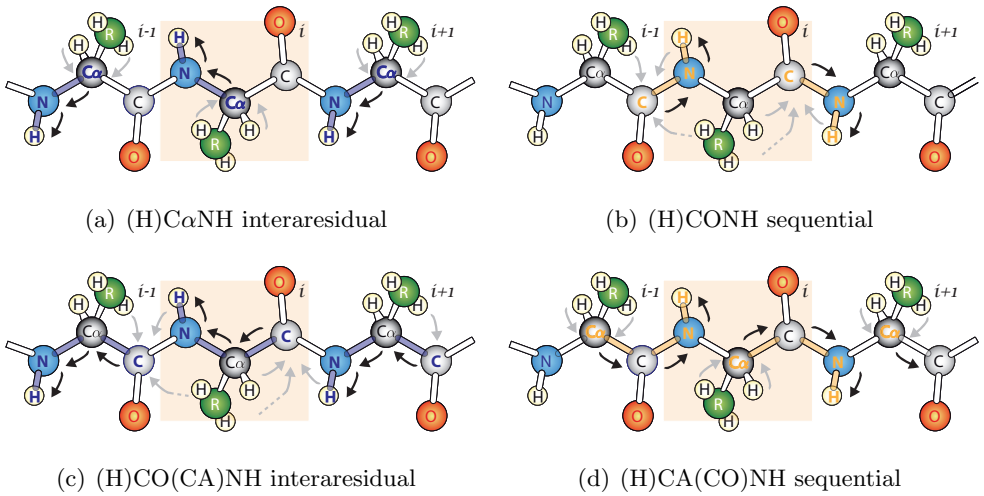

(a) (H)CαNH interaresidual

(b) (H)CONH sequential

(c) (H)CO(CA)NH interaresidual

(d) (H)CA(CO)NH sequential

Figure 4.13: Spin polarization transfer pathways in the four 3D triple-resonance proton-detected experiments. Grey arrows represent magnetization transfer from proton batch, black arrow backbone transfers, intraresidual transfers are shown in dark blue, sequential transfers in orange. the i-th peptide unit of the chain is highlighted with an orange background.

MAS.

The alignment of strips from these spectra (figure 4.14) yields a sequential walk, from which backbone resonances can be readily assigned. Different from the corresponding ^{13}C-detected experiments, assignment ambiguities are removed by the use of two common chemical shifts of the ^{1}H(i) and ^{15}N(i) nuclei for strip alignment, in complete analogy to the strategies adopted in solution-state NMR. Notably, the measurement time necessary to acquire the complete set of experiments for the backbone assignment was only about one week per sample, using about 3 mg of protein. ^{1}H, ^{15}N, ^{13}CO and ^{13}CA shifts for a total of 132 residues (out of 168 non-proline residues) were assigned in this way for ϵ_{186}, including residues in the central β-sheet, α-helices and in loops, demonstrating that the success of the assignment strategy is not dependent on local topology. Similarly, 83 out of 110 non-proline residues were assigned for the ssDNA-binding domain of SSB. Notably, this yields an assignment independently from previously available solution data, which is often a prerequisite for the study of solid molecules of this size [82, 103]. In this case, the procedure yielded a de novo assignment for a protein where no solution data were previously available.

4.6 Conclusions

We have demonstrated that the use of MAS at so-called ultra-fast spinning speeds in Solid-State NMR experiments makes possible the use of "totally low power" experiments. This is notably a way to reduce the duty cycle of the probe and, above all, to dramatically reduce unwanted heating which can lead to deterioration of the sample. Furthermore, it provided that

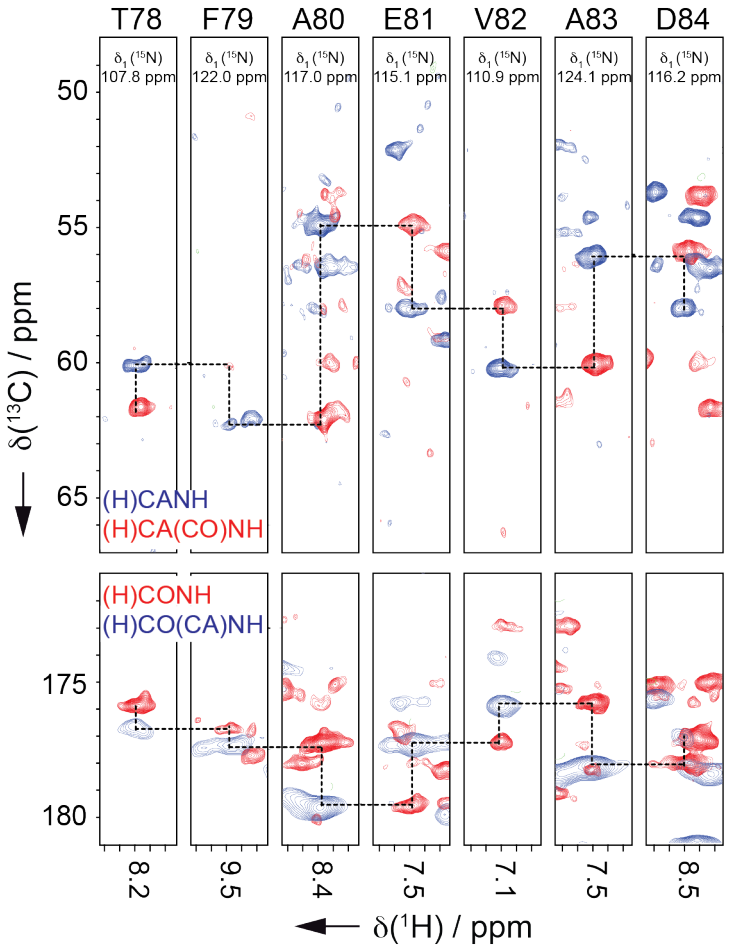

Figure 4.14: Representative strips from proton-detected assignment of [^{13}C,^{15}N]-ϵ_{186} under 60 kHz MAS: (H)CANH, (H)CA(CO)NH (blue and red contours, respectively, in the upper panel), (H)CONH, (H)CO(CA)NH (red and blue contours, respectively, in the lower panel). Sequential correlations are marked by dashed lines.

relaxation times are short enough, the recycling delay in the experiment can be reduced with a spectacular gain in overall sensitivity per unit time. Here this effect was demonstrated with a paramagnetic metalloprotein sample, ensuring short T_1s. However, paramagnetic doping could make similar experiments possible on diamagnetic samples [90].

Moreover, we have introduced a method to selectively orient polarization from the whole proton bath to a specific part of the carbon spectra, without any loss of sensitivity for the aliphatic signals and with a gain for carbonyls, which are more difficult to polarize with conventional CP. This ^{1}H-^{13}C SPECIFIC-CP technique may advantageously be combined with 2D correlation experiments to reduce experimental times by sampling selectively the bandwidths which contain information. The fact that it may result in totally low rf-field experiments makes it an ideal choice for the study of biological molecules, and we thus expect this to become a building block in many correlation methods used for either assignment or structure determination in solid

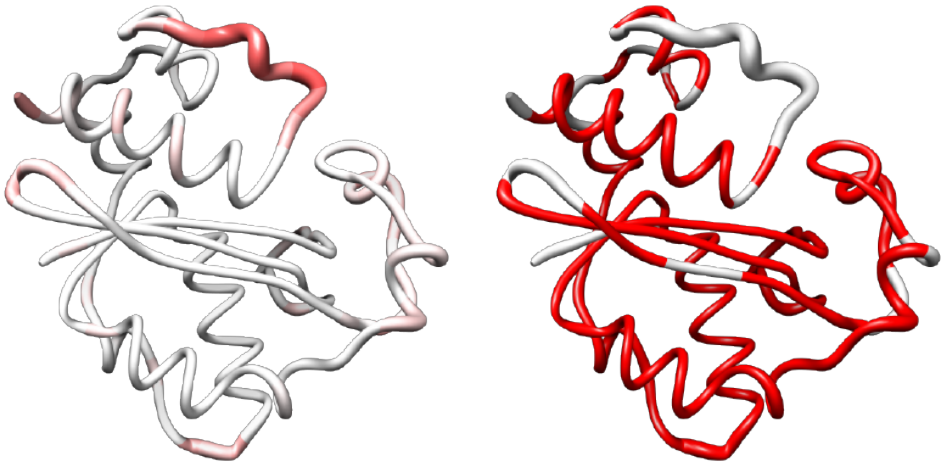

Figure 4.15: Cartoons of the X-ray single crystal structure of ϵ_{186} (PDB code 1J53), coloured according to B-factors (left, from white to red for increasing B-factor), and by assigned residues (right, unassigned residues in white).

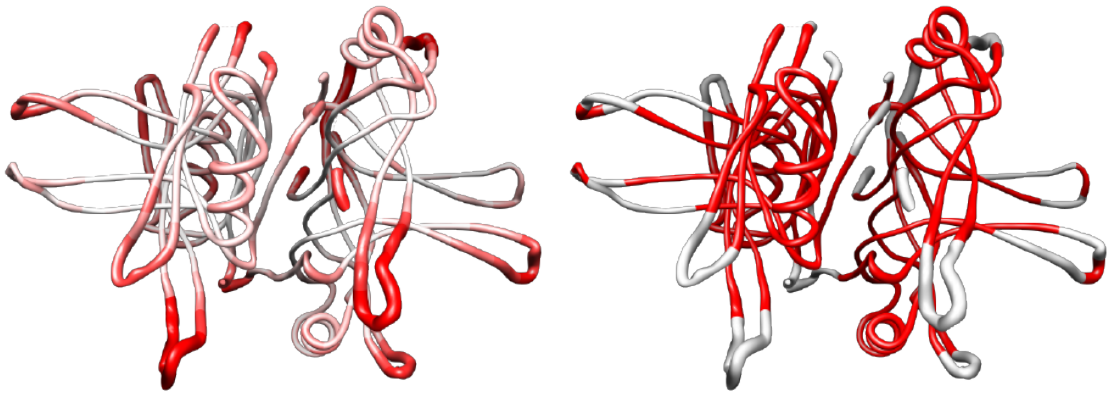

Figure 4.16: Cartoons of the X-ray single crystal structure of tetrameric SSB (PDB code 1EYG), coloured according to B-factors (left, from white to red for increasing B-factor), and by assigned residues (right, unassigned residues in white).

proteins.

Moreover, we have introduced a new NMR experiment, which performs sensitive and resolved through-bond correlations in solids under ultra-fast MAS. This is expected to become an important tool for the study of challenging biological systems in the solid-state, for which obtaining resolved fingerprints is a key step for any structural and biophysical characterization.

Finally, we have shown that narrow ^{1}H NMR line widths can be obtained for fully protonated

protein samples in the solid state under ultra-fast magic-angle spinning (60 kHz) for medium-size microcrystalline and non-crystalline proteins, without any need for dilution against a deuterated background. We demonstrate that this provides extensive, robust and expeditious assignments of the backbone ^{1}H, ^{15}N, ^{13}CA and ^{15}CO resonances of two proteins in different aggregation states, without the need of deuteration. The increased sensitivity afforded by ^{1}H spins at ultrafast MAS permitted acquisition of the complete set of experiments for backbone assignment using only 3 mg of [^{15}N,^{13}C]-labeled protein in less than a week in either study, which is considerably faster than conventional ^{13}C-detected experiments [119, 120]. Labor-intensive and often unaffordable or unsuccessful strategies for deuteration and back-exchange of protons are thus no longer a pre-requisite for useful ^{1}H-detected solid-state NMR spectra. This presents a major advance for biomolecular solid-state NMR, since constructive use of ^{1}H chemical shifts has so far been limited to samples where the ^{1}H spin bath was diluted through sparse ^{1}H labeling against a perdeuterated background. We believe that the approach outlined here will significantly increase the impact of solid-state NMR in structural biology by extending ^{1}H-detected experiments to samples that cannot be easily deuterated and/or can only be obtained in small quantities. In addition, sensitive ^{1}H-detected NMR experiments of non-crystalline samples open new opportunities for the detection of ligand binding in solid-state samples that cannot be studied by X-ray crystallography or high-resolution NMR.

Part II

Liquid crystals

Chapter 5

Thermotropic liquid crystal mesophases

This chapter aims to introduce readers who are not familiar with liquid crystals to the terminology and the necessary basic conceptual framework. We will define the director and order parameter concepts, discuss the structure of fluid smectic phases, and describe the remarkable effects of chirality observed in these phases.

5.1 Structural definitions

The word Liquid Crystals (often abbreviated in LCs or LXs) is used to encompass a class of phases of matter presenting, under given thermodynamic conditions, properties intermediate between the disordered liquid and crystalline solid. This introduction is in any case incomplete and misleading, since it is not based on a microscopic basis, but rather on a macroscopic and phenomenological one, which may apply also to other classes of soft matter material. To describe the peculiarity of LX phases, a short introduction to the types of order and their description is required.

5.1.1 Ordered and disordered phases

In nature many aggregation states can occur, and they are part of two main classes

- **Disordered phases:** characterized by a short or middle range order that has no macroscopic relevance for the sample. They encompasse isotropic phases of pure substances, as well as solutions, glasses or amorphous solids. In case of homogenous phases, physico-chemical properties show often scalar nature.

- **Ordered phases:** characterized by a long-range order, that can affect small clusters as well the whole sample. In case of homogenous phases physico-chemical properties are anisotropic and expressed by tensors.

The order that can characterize anisotropic mesophases is statistic (there is always movement except than close to 0 K), and can be positional or orientational.

Positional or translational order concerns the distibution of the centers of mass of the molecules or the aggregates of the phase (it is related to Cartesian coordinates). Positional order is the most important feature of the crystalline state, and mesophases that have this type of order are usually more viscous.

Orientational order concerns the azimuthal coordinates of the units that form the mesophase: molecules can be alligned along a preferential direction in the space that is called the director and is represented with the symbols $\overrightarrow{n}$ or **n**. The director is the principal symmetry axis of the orientational distribution function (ODF), which describes mathematically the long-range orientational order of the phase.

In the common uniaxial case, the ODF f(β) is expanded in terms of the even Legendre polynomials $P_{2L}\cos(\beta)$:

$$f(\beta) = \sum_{L=0}^{\infty} (2L+1)\, S_{2L} P_{2L}\cos(\beta) \tag{5.1.1}$$

where β defines the angle between the long axis of the unit (molecule or aggregate) and the tilt director **n**. The expansion coefficients S_{2L} in Eq. 5.1.2 are the scalar orientational order parameters, the first nontrivial of which is the Hermans-Tsvetkov orientational order parameter $S \equiv S_2$:

$$S = \left\langle P_2 \cos^2(\beta) \right\rangle = \frac{3\left\langle \cos^2(\beta) \right\rangle - 1}{2} \tag{5.1.2}$$

This parameter defines a simple measure of axial orientational order, that is, S=1 in the case of perfect orientational order and S=0 in an isotropic liquid phase. The higher is the value, the more the molecules tend to point to the same direction.

5.1.2 Liquid crystals and plastic crystals

Beside the crystalline state, two other aggregation phases show a certain degree of internal order, and they are:

- **Plastic crystals**
  In plastic crystals the centers of mass of the molecules form a regular crystalline lattice but the molecules are dynamically disordered with respect to the orientational degrees of freedom. Orientationally disordered crystals are often considered as model systems for structural glasses.

- **Liquid crystals**
  liquid-crystalline states of matter are anisotropic fluidic thermodynamically stable phases

Phases	**Positional Order**	**Orientational order**
solid crystal	yes (3D)	yes
plastic crystal	yes (3D)	no
liquid crystal		
columnar	yes (2D)	yes
smectic E	yes (2D)	yes
smectic C	yes (1D)	yes
smectic B	yes (1D)	yes
smectic A	yes (1D)	yes
nematic	no	yes

Table 5.1: Classification of the most important state of condensed matter possesing degree of order

charcaterized by orientational order (and, optionally, also positional order). They can be observed for a given set of thermodynamical variables (usually temperature, composition, pressure) between the crystalline state(s) and the state of the ordinary isotropic liquid state. They are often referred as mesophases, a term that reflect their intermediate position between the solid and the isotropic liquid state.

In Tab. 5.1 a short summary of the possible phases characterized by a certain degree of order is reported.

5.1.3 Classification of liquid crystals

In liquid crystalline phases the molecular distribution ot the aggregates retains a certain level of order, which is typical of solid crystalline phases, namely orientational order and a partial translational order. As a result of that, we can imagine that molecules or aggregates composing a LX can freely diffuse within the phase similarly as in isotropic liquids, although, unlike the latter ones, they remain surrounded by an anisotropic molecular environment (originated for example by the common preferential orientation), which implies that the physical properties of a liquid crystal are generally described by tensorial quantity. For such a reason, LX can be also defined as a fluid phase with strong anisotropic properties.

Liquid crystalline mesophases (abbreviated often in LCs) can be classified on the basis of:

The positional and orientational order that characterizes them macroscopically, as explained in the following paragraphs and summarized in Tab. 5.1.

The thermodinamic factor(s) that induce the appearance of the liquid crystalline behaviour. Phases can be thermotropic, in which the formation of the liquid-crystalline state essentially depends on the temperature T, or lyotropic, formed by anisometric aggregates of, for example, amphiphilic molecules dissolved in a nonmesogenic solvent. In lyotropic liquid crystals, the concentration of the solution is another essential variable of state.

The nature of the the mesogenic unit. Lyotropic liquid crystalline phases form various types of aggregates (micelles, layers...). Thermotropic liquid crystalline phases are composed of pure substances or mixtures of shape-anisotropic (anisometric) molecules, usually called "mesogens".

5.2 Thermotropic liquid crystals

Thermotropic phases are liquid crystalline mesophases that occur in a certain temperature range. If the temperature increases, thermal motion will destroy the delicate cooperative ordering of the LC phase, pushing the material into a conventional isotropic liquid phase. At too low temperature, most LC materials will form a conventional crystal. Many thermotropic LCs exhibit a variety of phases as temperature is changed

Thermotropic liquid crystals are today an essential part of our everyday life. With mobile telephones and then the digital camera revolution, liquid-crystal displays (LCDs) have become every person's property. Large-screen LCDs are rapidly increasing their share of the television market, and among computer displays they have become standard equipment within a few years. While inspired by this rapid progress, research on thermotropic liquid crystals in academia often does not deal directly with current technical developments. Instead, it focuses to a large extent on new materials, new device geometries, and new display modes (and also completely new applications of liquid crystals), as well as on the numerous, fascinating, nonapplied aspects of liquid-crystalline systems. In addition to improving our understanding of soft-matter physics and chemistry, this work paves the way for the next generation of displays to be used in, for example, high-quality, high-definition television. This work is indeed necessary, because today's commercial LCDs operate very close to the physical limits of the nematic liquid crystals on which they are based.

5.2.1 Main types of thermotropic mesogens

The mesogen is the fundamental unit of a thermotropic liquid crystal. The word "mesogen" refers to a single molecules, although examples of more sofisticated mesogenic units are possible. In the scientific literature many examples of mesogenic units of thermotropic liquid crystal are reported, which can be classified according to their shape:

- **Rod-like**.
  these molecules are represented by prolate rotors and show a clear elongated shape and a cylindrical symmetry. Considering the component of the inertia tensor, $I_a \gg I_b \cong I_c$.
  A typical structure is represented in figure 5.1(a).

- **Disk-like**.
  these molecule are represented by oblate rotors and are usually flat. Considering the component of the inertia tensor, $I_a \ll I_b \cong I_c$.

- **Lath-shaped** or **Board-shaped**
  One of the latest type to be discovered, they are usually dimers of molecule that interact mainly trough H-bonds.

- **Banana-shaped**.
  Shaped as a boomerang, they are one of the more intriguing class of mesogen, forming very exotic and peculiar mesophases very different from those of the other standard rod-like mesogens.

5.2.2 Rod-like mesogens

Rod-like mesogens have been studied for years. They consist tipically of a rigid moiety, the core, and one or more flexible parts. The rigid part aligns molecules in one direction, whereas the flexible parts induce fluidity in the liquid crystal. The optimum balance of these two parts is essential to form liquid-crystalline materials, as illustrated in figure 5.1(a). The rigid core can have additional lateral substituents, like methyl groups or charged or polar substituents to the aromatic core. Those residues are small enough not to alter the rod-like shape of the molecule but they may have in many case huge effects on the packing ability of the molecule. Linking units between the components of the mesogen are introduced during organic synthesis but can also play a key role in the characterization of the mesogen.

5.3 Thermotropic mesophases of rod-like mesogens

Mesophases formed by rod-like mesogens are the best characterized phases of liquid crystalline materials, described for the first time almost a century ago. In figure 5.2 they are briefly described, together with their common structural features and their mathematical representation.

5.3.1 Nematic liquid crystalline phases

Nematic phases, indicated by the letter N, are the most common synthetic LX mesophases. the word comes from Greek $\nu\eta\mu\alpha$ meaning "thread" and was created because of the appearance at the optic microscope of their topological defects, formally called disclinations.

In a nematic phase mesogens are usually calamitic or rod-shaped organic molecules that have no positional order, but self-align to have long-range directional order with their long axes roughly parallel. Thus, the molecules are free to flow and their center of mass positions are randomly distributed as in a liquid, but still maintain their long-range directional order.

Traditional nematic phases are represented as uniaxial: they have one axis that is longer and preferred, with the other two being equivalent (so they can be approximated as cylinders or rods). However, some nematic liquid crystalline phases are biaxial, meaning that in addition to orienting their long axis, they also orient along a secondary axis.

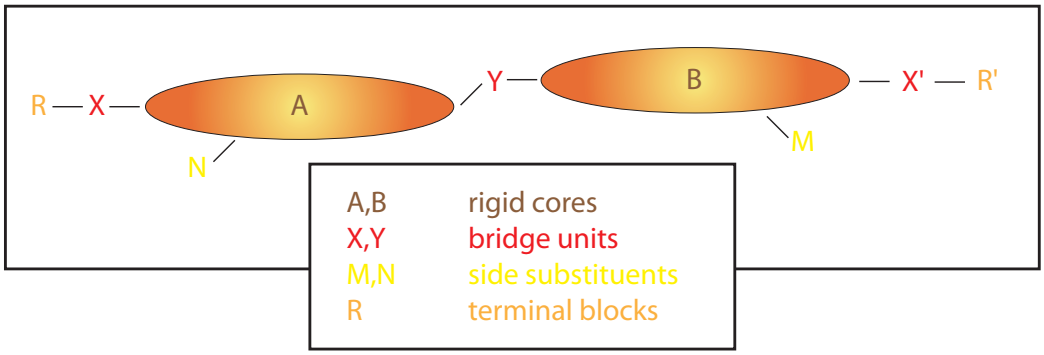

(a) General scheme.

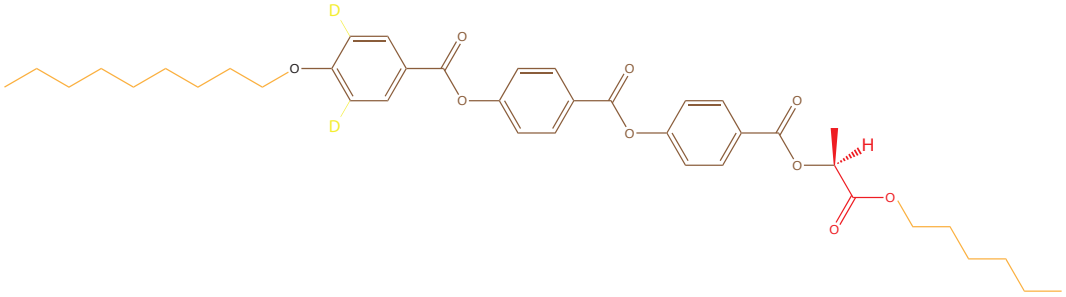

(b) A natural example.

Figure 5.1: (a) the mesogen of a calamitic liquid crystalline phase is a rod-like structure with a core usually composed of two or more rigid rings (usually of aromatic nature). (b) the structural formula of 9HL, an example of calamitic smectogen, is also shown.

Nematics have fluidity similar to that of ordinary (isotropic) liquids but they can be easily aligned by an external magnetic or electric field. Aligned nematics have the optical properties of uniaxial crystals and this makes them extremely useful in liquid crystal displays (LCD).

5.3.2 Smectic liquid crystalline phases

The word smectic is derived from the Greek word $\sigma\mu\eta\gamma\mu\alpha$, meaning "soap". This seemingly ambiguous origin is explained by the fact that the thick, slippery substance often found at the bottom of a soap dish is actually a type of smectic liquid crystal.

In the family of smectic phases the long-range orientational order is preserved but the full translational symmetry of the nematic state is broken in at least one direction. The various types of smectic mesophases are thus all signified by some translational order in one dimension (not present in the nematic) where the molecules are arranged on average in equidistant planes, which constitute a layered structure of a certain period d (usually referred to as the "smectic layer spacing" or "smectic layer thickness"), typically in the range of nanometers. We here denote the direction of translational order, the smectic layer normal, as k or $\overrightarrow{k}$ (See figure 5.2).

Motion is restricted to within these planes, and separate planes are observed to flow past

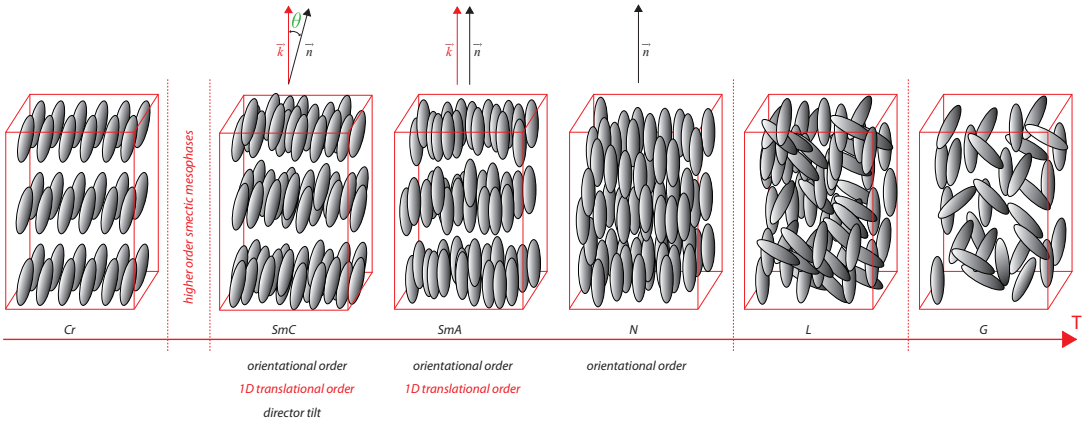

Figure 5.2: Schematic diagram of the molecular order and arrangement in the common thermotropic liquid-crystal mesophases of rod-shape mesogens, namely smectic C (SmC), smectic A (SmA), and nematic (N), between the usual crystalline (Cr) and the isotropic liquid states (L) and gaseous state (G) of matter. The director $\overrightarrow{n}$, the smectic layer normal $\overrightarrow{k}$ and the tilt angle θ are shown in black, red and green respectively.

each other. The increased order means that the smectic state is more "solid-like" than the nematic, as can be proved by their higher viscosity.

There are two main families of smectic mesophases: the most common ones are the so-called SmA and SmC that show no positional order in the planes [121] (see figure 5.2), but other phases can be found showing order inside their planes like SmB and its derivates (the so-called quasi-crystalline SmL with long-range order and the hexatic SmB with short-range order) and phases much closer to the crystalline form like SmE, SmH, SmK.

In the SmC phase, orientational and smectic translational order are observed along different axes in space. The director **n** is tilted with respect to the layer normal **k** by the tilt angle θ, **n** and **k** spanning the SmC tilt plane (see figure 5.3). The director tilt breaks the full rotational symmetry about **k**.

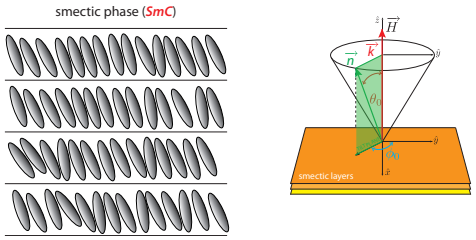

Figure 5.3: Illustration defining the basic entities used for describing the SmC geometry: tilt cone, tilt plane containing the director **n** and layer normal **k**, tilt angle θ and azimuth angle ϕ.

5.4 Chiral mesophases

The presence of chiral smectogens with one or more stereogenic carbons may induce chirality in the supramolecular structure of the mesophase. This chirality (indicated by an asterisk, *) has many striking consequences, the most common being helical superstructures which give the phases huge optical activity and an optical bandgap. Chiral macroscopic helicoidal structures can be induced by chiral smectogen (or by small quantity of chiral dopant too) only if the director of the phase has a component perpendicular to the helix's axis that rotates clockwise or counterclockwise along the mesoscopic domain. As a consequence of that, not all the thermotropic phases of chiral mesogens show helical superstructures.

5.4.1 Chiral nematic phases

Chiral nematic liquid crystalline phase (N^*) are traditionally known as cholesteric liquid crystals. The name origines from cholesteryl benzoate, the first liquid crystalline mesogen ever described [122], which is chiral and form this type of mesophases. In N^* phases the component of the director perpendicular to the helix's axis is the director itself, that varies in a continuous way along the sample inducing the helical structure (see figure 5.4). The variation of the director axis tends to be periodic in nature. The period of this variation (the distance over which a full rotation of 360° is completed) is known as the pitch, p. The pitch varies with temperature and it can also be affected by the boundary conditions when the chiral nematic liquid crystal is sandwiched between two substrate planes.

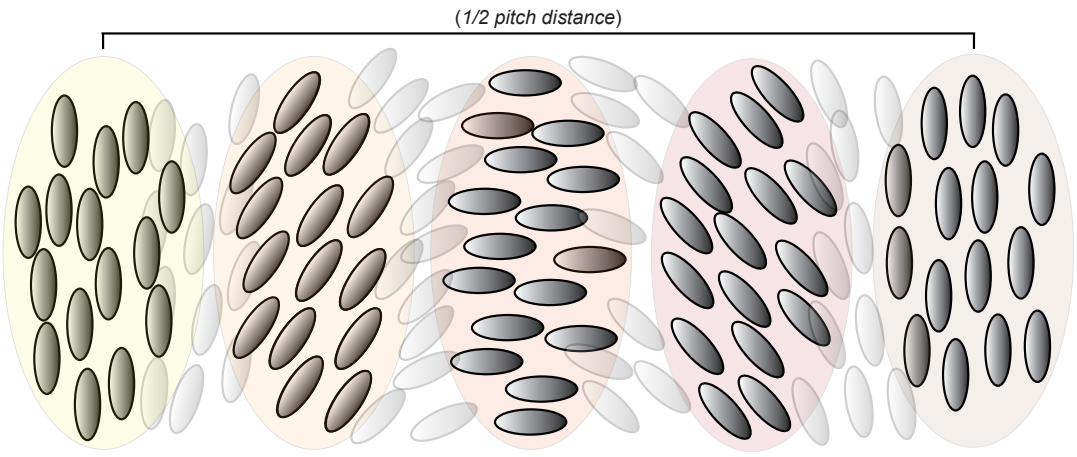

Figure 5.4: Schematic diagram of a chiral nematic mesophase. the layers shown are different from the layer induced by the positional order of smectic phases, the director varying in a continuous way.

5.4.2 Chiral smectic phases

In smectic phases the component of director that rotates inducing the helical strcture is the projection of the director on the smectic layer. As a result of this, if no other external effect is applied that induce a molecular tilt, only spontaneously tilted phases may originate super-molecular helical structures. The chiral supramolecular structure of the SmC^* is represented in figure 5.5.

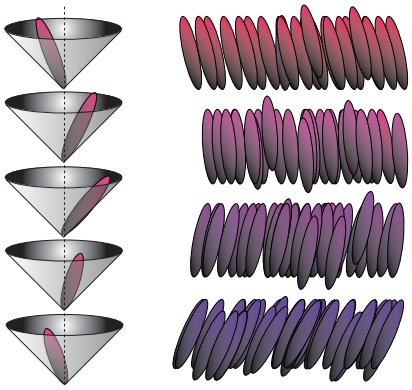

Figure 5.5: Schematics of ordering in a SmC^* phase. The portions of the helix pitches shown in the left and right figure are different.

The intriguing coupling among chirality, polarity and symmetry has very important effects on SmC^* phases. The supra-molecular structure induced by the presence of chiral smectogens with one or more stereogenic carbons and their peculiar molecular tilt yields the intriguing phenomenon of ferroelectricity of the smectic layers (figure 5.5) [121, 123].

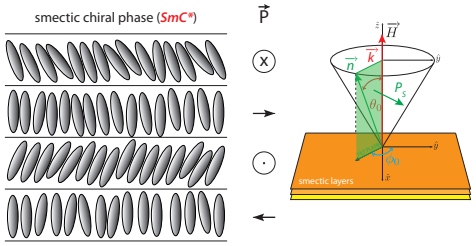

Figure 5.6: Illustration defining the basic entities used for describing the SmC^* geometry: the polarization P_s that appears in the chiral SmC^* phase is always perpendicular to the tilt plane.

Chiral tilted smectics (among which the family of SmC^* phases is by far the most important) are therefore unique in that they constitute the only known cases of spontaneously polar phases in soft matter (i.e., polar on a meso- and/or macroscopic scale). The discovery by Meyer in the mid-1970s that a chiral smectic C (SmC^*) phase exhibits a spontaneous electric polarization has induced a substantial boost in the smectic liquid-crystalline state of matter. This has

lead with the subsequent demonstration by Clark and Lagerwall of the surface-stabilized SmC^* ferroelectric liquid crystal (FLCs) at the beginning of the 1980s [124].

The presence of a polarization vector is a consequence of the simmetry of the phase. The symmetry of the SmA phases is $D_{\infty h}$, that is, they have an infinite-fold rotation axis along the director **n** and a mirror plane as well as an infinite number of twofold rotation axes perpendicular to **n**. These phases cannot be polar, because symmetry is too high to allow a polar vector in any direction. In the SmC phase, the appearance of a nonzero tilt between **n** and the layer normal **k** drastically reduces the symmetry to C_{2h}, but this still does not allows spontaneous polarization. A polarization in the tilt plane would violate the remaining twofold rotation symmetry and perpendicular to this the fact that the tilt plane is a mirror plane prohibits polarization.

As we said previously, in opposition to SmC^* phases, SmA phases composed of chiral smectogens do not show any macroscopic chiral behaviour. In any case the chirality of the mesogen induces other peculiar physico-chemical properties to the mesophase. Meyer and Garoff proved that these mesophases could undergo a reduction of their simmetry thanks to the so-called electroclinic effect: if an electric field is induced in the phases, it induces a dipole along itself, that determines a non-zero transverse polarization of the mesogens. If this polarization is high it may induce a torsion of the mesogen proportional to the intensity of the applied field. This phenomenon generates a tilted structure similar to the SmC^* phases, reducing the simmetry of the mesophase to D_∞.

Chapter 6

Analysis of de Vries mesophases through ^{2}H NMR Spectroscopy

6.1 Smectic mesophases

Some of the most interesting systems for future display devices are chiral smectic liquid crystals which, due to their reduced symmetry, can exhibit ferro- and antiferroelectric properties, thereby giving them operational speed and resolution far superior to those of the nematic technology. Interest in the smectic liquid-crystalline state of matter received a substantial boost with the discovery by Meyer in the mid-1970s that a chiral smectic C (SmC^*) phase exhibits a spontaneous electric polarization, and with the subsequent demonstration by Clark and Lagerwall of the surface-stabilized SmC^* ferroelectric liquid crystal at the beginning of the 1980s. Since then, chiral smectic phases and their plethora of polar effects have dominated the research in this field, aiding the development of new ferroelectric (FLC) and antiferroelectric (AFLC) electrooptic systems. Although the pioneering results are now about 25-30 years old (in comparison, the fundamental discoveries in the field of nematic display technology were made at the end of the 1960s), some important obstacles for large-scale commercial application of smectic liquid crystals yet remain to be solved. Nevertheless, the field has found a niche market in fast high-resolution microdisplays for near-eye applications, such as viewfinders for digital cameras and camcorders.

6.1.1 Layer shrinkage

One of the major problems to the application of common ferroelectric smectic materials is related to the shrinkage of smectic layer thickness at the transition from the not-tilted SmA phase to the polar SmC^* phase, because of the increasing tilt of the mesogenic molecules within smectic layers (see figure 6.1). This shrinking normally produces zigzag defects due to the opposite distribution of chevron configurations, thus limiting the performance and quality of electrooptic devices [124]. Essentially temperature-independent smectic layer spacing is especially important

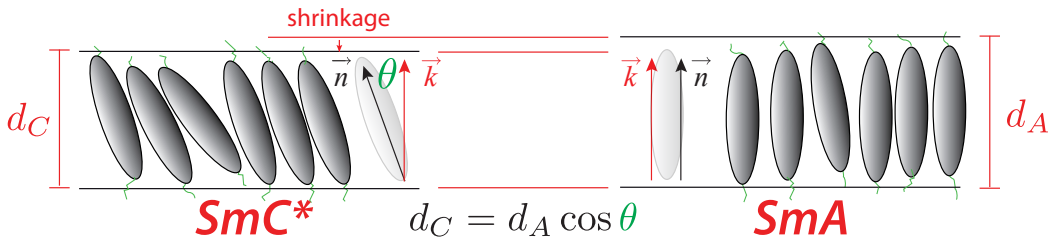

Figure 6.1: The skrinkage phenomenon at SmA-SmC^* transition. Director, layer normal and tilt angle are indicated as in chapter 5.

for possible display applications of ferroelectric liquid crystals (FLCs).

6.2 de Vries phases

In the last decades, several smectic compounds have been found to behave differently from standard ones. Their mesophases, called de Vries phases from the name of the Dutch crystallographer Adriaan de Vries, essentially do not change their smectic layer spacing at the tilting transition between the SmA and the SmC^* phases, thus excluding the occurrence of so called "Chevron" defects at the SmA-SmC^* transition, the main limit of the performance and the quality of current electro-optic devices. For this reason, these de Vries-type phase transitions of liquid crystalline (LC) smectogens [124, 125, 126, 127, 128, 129] have recently attracted the attention of both industry and academia involving many research teams [130, 131, 132, 133], due to their potential applications in the development of new ferroelectric (FLC) and antiferroelectric (AFLC) electrooptic devices. The nature of the de Vries transition remains a challenging aspect for researchers active in the material science field, especially the knowledge of the molecular peculiarity of "de Vries" liquid crystals as well as the influence of external fields on their molecular organization. However, in the recent years, fundamental progresses have been done in the comprehension of the de Vries-type materials, and many phenomenological properties have been characterized. They are:

- **layer spacing** As we said, these mesophases show indeed a substantially constant layer spacing within the SmA and the SmC^* phases, with a modest layer shrinkage (less than 5%).

- **electroclinic effect** SmA phases formed by de Vries LCs have an uncommonly large electroclinic effect [134], which is strongly connected to the presence of significant tilt of molecules. The application of external electric fields determines an increase of the induced tilt angle, often defined as "optical tilt" to distinguish it from the molecular tilt, whose temperature dependence is well described by the Landau mean field theory [135].

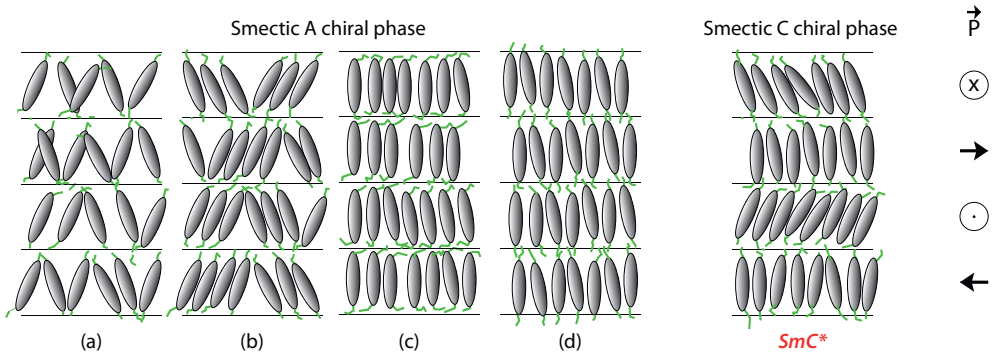

Figure 6.2: Sketch of the four proposed models for de Vries SmA phase. From left to right: (a) random diffuse cone, (b) cluster diffuse model (c) conformational change model (d) interdigitation model; at the right, a representation of the corresponding ferroelectric SmC^* phase and helical arrangement of both molecules and spontaneous polarization are also shown.

- **large soft-mode absorption** The dielectric soft-mode absorption significantly increases. Since tilt-angle fluctuations can be observed as a soft-mode absorption in the dielectric spectrum of FLCs, dielectric spectroscopy is a powerful tool to investigate correlations of these fluctuations and the extent of layer shrinkage.

- **high birefringence**

6.2.1 Models for de Vries phases

Since their first discovery, several models have been proposed to explain such an unconventional feature and the nature of the de Vries transition remains a challenging aspect. These hypotheses are shown in figure 6.2 from left to right:

- **diffuse cone model** The first interpretation, still partially valid, is the one described by the Adriaan de Vries himself [126], known as the "diffuse cone model". He proposed that in these systems smectogens are tilted (with respect to the layer normal) also in the SmA phase, but that the azimuthal angle is randomly distributed within the smectic layer. The SmA-SmC^* phase transition is thus seen as a disorder-order transition in the azimuthal directions of the molecular tilt. Several experimental works on different liquid crystals showing de Vries-type transitions, basically confirmed this hypothesis, even though this does not exclude other possible explanations.

- **cluster diffuse model** It is a variation of the "diffuse cone model". Although the presence of an average tilt is accepted, the "random" distribution in azimuthal angle is replaced with a "locally ordered" or "cluster" distribution in azimuthal directions

- **conformational change model** This model was proposed by Diele *et al.* [131]: smectogens would experience a different average conformation in the two smectic phases and the

absence of a layer shrinkage is explained in terms of different orientations of both rigid core and lateral chains passing from the SmA to the SmC^* phases

- **interdigitation model** It is a model adapted to describe nanosegregated systems, such as fluorinate or organosiloxane derivatives, that invokes a different behavior of molecules at the interface between consecutive smectic layers in the two phases. Within the "interdigitated" model [136, 137] in the SmA phase, molecules are not tilted but partially interdigitated, thus justifying a smectic layer spacing smaller than the effective molecular length. On the contrary, in the SmC^* phase, molecules are tilted, but interdigitation does not occur anymore and the measured layer spacing results similar to that in the SmA phase [138].

The combination of experimental NMR techniques and theoretical models has allowed one to get valuable information about the molecular structure, order and dynamics of various liquid crystalline mesophases. Recently this kind of studies were extended to magnetic nuclei which don't require to isotopically enrich the samples, such as ^{13}C and ^{19}F, in contrast to previous work on ^{2}H. In the last years, the interest has focused mainly on chiral calamitic smectic mesogens and banana-shaped liquid crystalline mesophases.

To our best knowledge, NMR spectroscopy has never been applied to de Vries-type LC systems, despite its great potential in the determination of both local and molecular properties, namely orientational and conformational ones [139, 140, 141].

6.3 Properties of the 9HL system

The properties of the "de Vries" smectogen, the (S)-hexyl-lactate derivative abbreviated as 9HL and the analogous LC selectively deuterated in a phenyl moiety of the aromatic core, namely 9HL-d_2, shown in figure 6.3 are synthetized in tab. 6.1. Synthesis and chemical physical characterization of 9HL are reported in [142, 125, 130, 143]. The mesophase transitions of 9HL-d_2, as detected by means of DSC by cooling the sample at 5°C/min rate and by polarized optical microscopy are:

Isotropic - 128°C -SmA - 74°C - SmC^* - 35°C - crystal.

6.4 Results

6.4.1 Deuterium data

In the present work, ^{2}H-NMR measurements on a ^{2}H-labeled "de Vries" compound, namely 9HL-d_2 (see figure 6.3), were performed in the whole mesophasic temperature range at five values of the magnetic field strength, namely 4.70 T, 7.05 T, 11.75 T, 16.45 T, 18.80 T. It is worth noticing that such high magnetic fields has never been used to study LCs by NMR. This NMR

compound name	**m.p.** $\Delta H/Jg^{-1}$	**Cr**	$T_{tr}/°C$ $\Delta H/Jg^{-1}$	SmC^*	$T_{tr}/°C$ $\Delta H/Jg^{-1}$	SmA	$T_{tr}/°C$ $\Delta H/Jg^{-1}$	Iso
9HL	60 +26.8	•	39 -28.39	•	73 -0.07	•	127 -5.31	•
9HL-d_2	61 +28.9	•	35 -28.13	•	74 -0.05	•	128 -4.99	•

Table 6.1: Sequence of phases, phase transition temperatures (in °C) measured on cooling (5 K min−1), melting points and m.p. (°C), clearing points, c.p. (°C), measured on heating (5 °C min−1), and related transition enthalpies ΔH (Jg^{-1}) determined by DSC. (• - the phase exists).

Figure 6.3: Molecular structure of the 9HL-d_2 compound under investigation. Optimized geometry is displayed with the orientation of the local director of the deuterated phenyl fragment (n_p) and the layer normal (l) to the SmA planes (π).

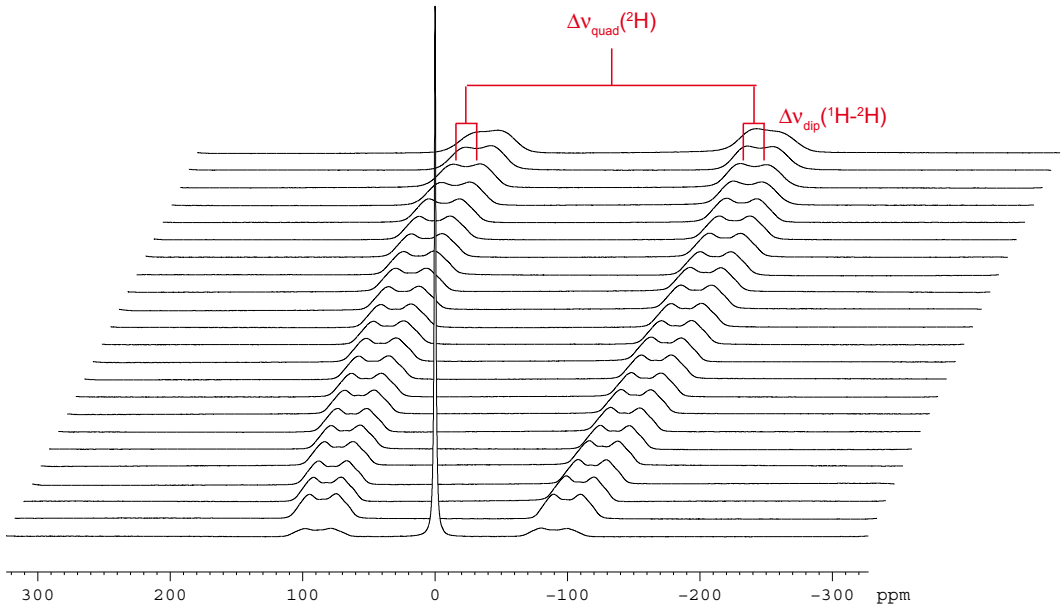

Figure 6.4: ^{2}H NMR spectra of 9HL-d$_2$ recorded from 127.5°C to 70°C every 2.5° at 11.75 T. Quadrupolar $\Delta\nu_{quad}$ (^{2}H) and dipolar $\Delta\nu_{dip}$ (^{1}H-^{2}H) splittings are shown.

technique can help in understanding basic molecular and conformational properties within the whole de Vries *SmA* mesophase and at the *SmA*-*SmC** transition, thus adding fundamental information to discriminate among the theoretical models reported in the literature.

The ^{2}H-NMR spectra are characterized by a doublet (^{2}H quadrupolar splitting) further split by the ^{1}H-^{2}H dipolar coupling between the deuterium and protons in *ortho* position on the labeled ring of 9HL-d$_2$.

6.4.2 Order parameters and biaxiality

The analysis of the variable-temperature spectra allowed us to obtain both quadrupolar ^{2}H $\Delta\nu_{quad}$ and dipolar ^{1}H-^{2}H $\Delta\nu_{dip}$ splittings. These experimental data have been analyzed through equations [144, 139]:

$$\Delta\nu_{dip}\left[T\right] = -2K_{DH}\left(\frac{S_{zz}\left[T\right]}{r_{DH}^3}\right) \tag{6.4.1}$$

$$\Delta\nu_{quad}\left[T\right] = \frac{3}{2}q_{aa}\left[S_{zz}\left[T\right]\left(\cos^2\phi - \frac{1}{2}\sin^2\phi - \frac{\eta}{6}\cos^2\phi + \frac{\eta}{6} + \frac{\eta}{3}\sin^2\phi\right) + \Delta_{biax}\left[T\right]\left(\frac{1}{2}\sin^2\phi + \frac{\eta}{6}\cos^2\phi\right) + \frac{\eta}{6}\right] \tag{6.4.2}$$

where K_{DH} = 18434.4 Hz $\cdot\mathring{A}^3$, r_{DH} = 2.5 $\mathring{A}$, η = 0.04, q_{aa}= 185 kHz. The angle ϕ can be assumed equal to 60° for the undistorted phenyl ring geometry [145, 144, 146]. The fitting variables are the order parameters (S_{zz} and Δ = S_{xx} - S_{yy}) relative to the deuterated phenyl ring (with z being along the para axis). For the three sets of measurements performed at lower magnetic fields (4.70 T, 7.05 T and 11.75 T), two separate fitting procedures have been performed for the SmA and the SmC^* phases, respectively. The reproduction of the experimental quadrupolar and dipolar splitting is good (with error less than 2%). The observed trends of both splittings from the SmA to the SmC^* phase are typical of ferroelectric LCs [145, 144, 146], in particular, the helical axes of the SmC^* domains are oriented parallel to the external magnetic field and molecular longitudinal axis (as well as the rigid aromatic cores) are tilted with respect to the magnetic field. The behavior of the splittings is different at higher magnetic fields, namely 16.45 T and 18.80 T: both quadrupolar and dipolar splitting increase continuously within the whole mesophasic temperature range without any discontinuity at the SmA to the SmC^* transition. This behavior has been observed in other "normal" ferroelectric LCs when the external magnetic field exceeds the critical value needed to unwind the SmC^* helical axis.

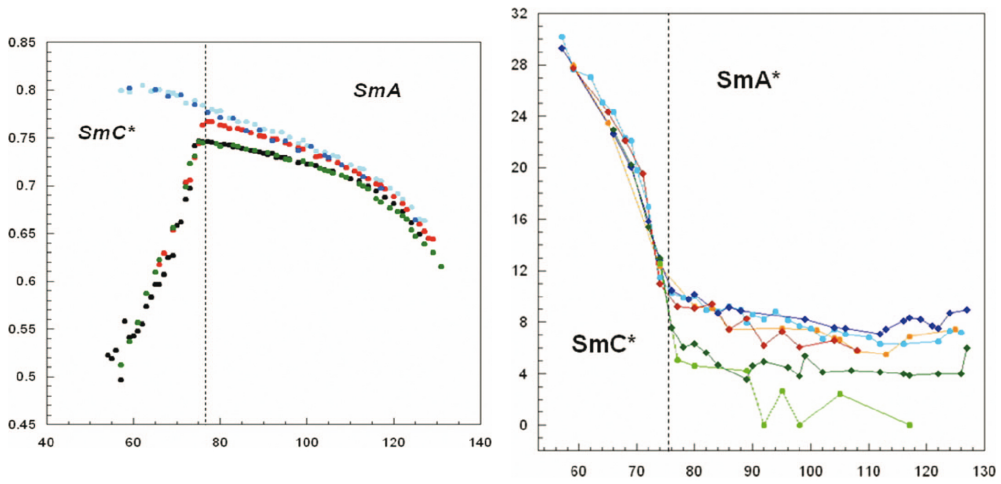

(a) S_{zz} in 9HL-d$_2$ mesophases (b) calculated tilt angle in 9HL-d$_2$ mesophases

Figure 6.5: Structural information extracted from 9HL-d$_2$ (a) Main orientational order parameter, S_{zz}, vs Temperature (°C) of the ^{2}H-labeled phenyl ring of 9HL-d$_2$ as obtained by analyzing ^{2}H-NMR spectra recorded at 4.70 (dark green •), 7.05 (black •), 11.75 (red •), 16.45 (cyan •) and 18.80 (blue •) Tesla (b) Tilt angle θ (degrees) vs Temperature (°C), directly evaluated from ^{2}H-NMR data by using Equation 6.4.3. The saturation values of S_{zz} (corresponding to data recorded at 16.45 T and 18.80 T) are compared with those obtained at low fields: 18.80 T vs 7.05 T (dark blue ⋄), 16.45 T vs 7.05 T (cyan □),18.80 T vs 4.70 T (red ⋄), 16.45 T vs 4.70 T (orange □), 18.80 T vs 11.75 T (dark green ⋄), 16.45 T vs 11.75 T (light green □).

The trends of the splitting vs temperature at various magnetic field strengths reflect in the trends of the order parameter S_{zz} obtained by fitting the experimental data, as shown in figure 6.5(a). The values of the fragment biaxiality, Δ_{biax}, in the SmA and SmC^* phases of

9HL-d_2 have been found similar to other LC smectogens, ranging between zero to 0.05. This is quite typical for deuterated phenyl moieties of LC cores. The most peculiar property concerns the value of the local order parameter S_{zz} in the SmA^* phase of 9HL-d_2. As seen in figure 6.5(a), the values of S_{zz} increase significantly by increasing the magnetic field strength. This effect, was never observed in "normal" SmA phases. Interestingly, the two trends at lower fields are almost coincident, thus indicating that values of the magnetic field lower than 7.05 T do not influence the SmA structure and molecular organization. Moreover, the two trends of S_{zz} at higher magnetic fields are also coincident, implying that the saturation of S_{zz} is reached with magnetic fields higher than 11.75 T and lower or equal to 16.45 T (namely, the critical magnetic field is in this interval). The main orientational order of the deuterated ring in the SmA^* phase at the intermediate field of 11.75 T is indeed lower than that observed at 16.45 T and higher than that observed at 7.05 T.

6.4.3 Tilt angle calculation

The strong effect of the magnetic field [147, 148, 140], on the orientational order of the aromatic fragment of 9HL-d_2 within the SmA mesophase indicates, analogously to the case of SmC^* phases, that the molecules of 9HL-d_2 are tilted with respect to the SmA layer normal. The molecular tilt, in particular the tilt of ^{2}H-labeled phenyl rings, can be determined by direct comparison between the main order parameters obtained at higher fields, S_{zz}^{hf}, (18.80 T and 16.45 T) and those obtained at lower fields, S_{zz}^{lf}, (4.70 T and 7.05 T), through Eq. 6.4.3

$$S_{zz}^{lf}(T) = S_{zz}^{hf}(T) \cdot \left(\frac{3}{2}\cos^2\theta - \frac{1}{2}\right) \tag{6.4.3}$$

The values of the tilt angle θ found by comparing the orientational order parameter S_{zz} at various fields are reported in figure 6.5(b). The tilt angle θ ranges between 5° and 12° in the SmA phase (see blue, cyan, red and orange symbols in figure 6.5(b)), while it increases by decreasing the temperature within the SmC^* phase reaching the higher value of about 30°.

In the case of intermediate fields, such as 11.75 T, the "not complete alignment" of molecules is responsible for the lower value of the tilt (see green symbol in figure 6.5(b)).

6.5 Discussion

The main points arising from the present NMR study can be summarized as follows:

- the molecules of 9HL-d_2 are tilted also in the SmA phase. The tilt angle determined directly herein refers to the aromatic ring but we expect that it is similar to the tilt angle of the whole molecule (long molecular axis). In fact, the aromatic fragment closer to the achiral and longer terminal chain is usually the most aligned moiety of this type of mesogens, and its orientational order is usually taken as representative of the whole molecular orientational order [139, 140].

- The jump of the tilt angle observed at the *SmA*-*SmC** transition is more likely due to a conformational change - this point could be further verified by solid-state ^{13}C NMR methods and *ab initio* conformational investigations.

- As depicted in figure 6.5(a), the orientational order of the phenyl fragment in the 9HL-d_2 sample is relatively high. This result seems to be in contrast with what suggested either by theoretical or experimental studies on several de Vries materials [136, 124]. However, it should be noticed that the present compound, 9HL, has been indicated as being unconventional in the contest of de Vries-type LC materials, since, due to its molecular formula [124], it is rather similar to common ferroelectric LCs.

- As observed in figure 6.5(a), the high magnetic field used herein is able to make significant changes in the orientational order of the aromatic core not only in the *SmC** phase, but also in the *SmA* phase. If this effect is now well understood in the case of the *SmC** phase [147, 149], since it is associated with a complete unwinding of the helical supramolecular structure, it is not the same for the *SmA* phase. In order to explain the large magnetic effect in the *SmA* phase of 9HL, not observed so far in any other LC smectogens, a discussion about the theoretical models proposed to describe the structure of the *SmA* phase in de Vries-type LCs is needed. Indeed, the effect of the magnetic field reported in figure 6.5(a) is not consistent with a completely random or uncorrelated diffuse cone model of the *SmA* phase. The reason is that, even though the magnetic field of 16.45 T is high, it is not strong enough to orient single molecules. The contribution of the magnetic energy of single, isolated molecules is indeed negligible with respect to other contributions [135] because of the low molecular susceptibility anisotropy of LCs. The interaction energy due to cooperative molecular ordering is, on the contrary, crucial [150, 151, 140] and could be the only possible explanation of the observed behaviour. In fact, organized structures, such as ordered aggregates or clusters of molecules, for which the mesophase susceptibility anisotropy becomes relevant, can further align the phase director along a strong enough magnetic field, analogously to *SmC* phases [140]. Herein, the observed effect of the high magnetic field in the *SmA* phase can be justified by the presence of spatial modulations or local periodicities in the azimuthal angle distribution, which would imply a significant interaction energy contribution. This picture agrees with a recent work by Prasad *et al.* [137], where a nanoscale correlation length was found in the SmA phase formed by de Vries-type LCs. Their estimation of the dimensions of clusters, about few tens of nanometers, is consistent with the hypothesis of clusters of molecules with the same azimuthal angle within the same smectic layer, or in other words, with local periodicities in the azimuthal angle distribution associated to the molecular tilt.

6.6 Conclusions

To conclude, herein we report for the first time a NMR study of a de Vries compound, namely 9 HL, with a SmA phase stable in a large temperature range. This study shows that the SmA phase formed by this de Vries compound sensibly differs from conventional SmA phases. Measurements performed at a relatively high magnetic field allowed us to obtain an estimation the tilt angle of the deuterated phenyl moiety in the SmA and SmC^* phases as well as the trend of the local orientational order, which reasonably mimics that of the whole molecules. The values of the tilt angle observed in the SmA phase of 9HL-d_2 confirm the peculiarity of the SmA phase formed by de Vries materials, also envisaging an alternative way of evaluating the tilt angle in these phases by recurring to a comparison of NMR measurements acquired at different magnetic field intensities. The jump in the trend of the tilt angle at the SmA-SmC^* transition provides an additional information on molecular properties of de Vries LCs. An explanation of this result is that NMR spectroscopy is able to better determine molecular features than other experimental methods used so far to investigate de Vries LCs, which are indeed specific to detect macroscopic properties, that is, the large electroclinic effect and the absence of layer spacing shrinking. Another important point of this work is the large magnetic field effect observed in the SmA phase as well, which induced us to propose a picture alternative to the completely random diffuse cone model. Indeed, this large effect suggests the presence of a spatial modulation of the azimuthal angle within the SmA layers, and probably the presence of local clusters of molecules with the same tilt and azimuthal angles. Further NMR studies at different magnetic field strengths as well as by detecting different nuclei are expected to give additional insights on this topic.

Conclusions

During the experimental work for this thesis a broad range of topics has been addressed. All the results previously reported fall within the framework of Nuclear Magnetic Resonance Spectroscopy, in particular of Nuclear Magnetic Resonance of systems characterized by a certain degree of anisotropy, namely protein crystals or thermotropic liquid crystalline mesophases. These variety of targets may be seen as a proof of the key role of this technique, which allows gathering of atomic level information from various systems, ranging from physics via chemistry to biology.

In the first part of this work some key aspects concerning solid-state NMR as an emerging tool in the field of structural biology have been addressed. Implementation of solid-state NMR as biophysical technique requires development of new strategies in hardware and instrumentation, in sample preparation and in experiment design. New model systems more many-sided than simple small globular proteins are required.

The N-terminal domain of the ϵ subunit of DNA polymerase III from *E. Coli* (ϵ_{186}) has been selected as a system of interest due to its complete structural characterization with previous X-ray and liquid NMR studies, its relatively large size and also its multifaceted biophysical role both as metalloenzyme and as units interacting with other proteins.

Since samples containing high salt-concentration suffer from heating during ^{13}C detected solid-state NMR experiments, as a first step ϵ_{186} has been crystallized at low-salt conditions suitable for reducing heating phenomena during spectra acquisition. Crystallization conditions at low and high pH have been found respectively via refining of published crystallographic protocols or via *de novo* automatized screening. This result shows the great potentiality of the integration of solid-state NMR with methods developed for high-throughput crystallography.

Complete resonance assignment of backbone and side-chain of ϵ_{186} have been obtained using well-established 2D homonuclear and 3D heteronuclear NCOCX and NCACX experiments, rendering the system suitable for further structural or biophysical studies with solid-state NMR or method development.

In particular, on ϵ_{186} and other systems a broad range of new techniques have been applied that show the great potentiality of the new emerging field of so-called ultra-fast (60 kHz) magic-angle spinning (MAS) solid state NMR. In this regime efficient bandselective CP experiments and heteronuclear decoupling are efficiently performed with low-power irradiation. This enables both an increase in resolution, by allowing longer acquisition times in direct and indirect dimensions

of multidimensional correlations, and in sensitivity, by shortening the interscan delays, without unwanted heating and subsequent deterioration of the sample.

In addition, in this MAS regime, correlation experiments based on J-transfers become competitive alternatives to dipolar transfer schemes. J-based experiments require long evolution delays for the creation and the refocusing of coherences between neighboring spins, and can therefore take advantage from the low-power irradiation regime, that allows long coherence lifetimes to be obtained without the negative effects of strong rf fields. A new NMR experiment that detects sensitive and resolved through-bond correlation in solid, has been implemented.

Finally, we have shown that narrow ^{1}H NMR line widths can be obtained for fully protonated protein samples in the solid state under ultra-fast magic-angle spinning for medium-size microcrystalline and non-crystalline proteins, without any need for dilution against a deuterated background. We demonstrated that this provides extensive, robust and expeditious assignments of the backbone ^{1}H, ^{15}N, ^{13}Cα and ^{15}CO resonances of fully protonated ϵ_{186}, and similar results have been obtained on the gel-like precipitate of fully protonated SSB, the tetrameric single-stranded DNA-binding protein, proving that this strategy may be effective not only on well-ordered crystalline systems.

In parallel to this work of methods development, other well-established NMR technique have been applied to discriminate among possible models of phase transition in very peculiar thermotropic liquid crystal phases, called de Vries, that show a substantially constant layer spacing in the transition between smectic C and smectic A. A complete ^{2}H-NMR study on the chiral smectogen 9HL has allowed the discrimination of the possible hypothesis, showing the importance of NMR not only as complementary technique but as a key protagonist in the study of material science.

In summary, in the course of this work new methods for biological solid-state NMR spectroscopy have been developed, making further steps in the implementation of this emerging technique. We have indeed demonstrated that "totally low power" experiments are feasible and are ideal candidate for the study of biological molecules. Thanks to these new methods, solid-state NMR is in good position to strongly support in the future the advancement of the field of structural biology, but its potential success as biophysical technique relies however on the perspective to access systems that are difficult to crystallize or that form large heterogeneous complexes and insoluble aggregates. For these reason new model system like ϵ_{186} easy to express and crystallize that can mimic various physiological problem are important, in particular its role in the formation of aggregates.

Bibliography

[1] Christian Boehmer Anfinsen. Principles that govern the folding of protein chains. *Science (New York, N.Y.)*, 181(4096):223–30, July 1973.

[2] Cyrus Levinthal. Are there pathways for protein folding? *Journal of Medical Physics*, 65(1):44–45, 1968.

[3] Udo Heinemann, Konrad Büssow, Uwe Mueller, and Patrick Umbach. Facilities and methods for the high-throughput crystal structural analysis of human proteins. *Accounts of chemical research*, 36(3):157–63, March 2003.

[4] Bernhard Rupp. *A guide to automation and data handling in protein crystallization, in Crystallization Strategies for Structural Genomics.* International University Line, San Diego, CA, 2006.

[5] Martin Hammarström, Niklas Hellgren, Susanne van Den Berg, Helena Berglund, and Torleif Härd. Rapid screening for improved solubility of small human proteins produced as fusion proteins in Escherichia coli. *Protein science : a publication of the Protein Society*, 11(2):313–21, February 2002.

[6] Marcel Dekker. *Protein Structure. Determination, Analysis, and Applications for Drug Discovery.* New York-Basel, 2003.

[7] Xiao Dong Wang, Michael Gleaves, David Meredith, Rob Allan, and Colin Nave. e-Science Technologies in Synchrotron Radiation Beamline - Remote Access and Automation (A Case Study for High Throughput Protein Crystallography). *Macromolecular Research*, 14(2):140–145, 2006.

[8] Raymond Hui and Aled Edwards. High-throughput protein crystallization. *Journal of Structural Biology*, 142(1):154–161, April 2003.

[9] Marie Renault, Abhishek Cukkemane, and Marc Baldus. Solid-state NMR spectroscopy on complex biomolecules. *Angewandte Chemie (International ed. in English)*, 49(45):8346–57, November 2010.

[10] Martin Caffrey. Membrane protein crystallization. *Journal of Structural Biology*, 142(1):108–132, April 2003.

[11] Christopher P Jaroniec, Cait E MacPhee, Vikram S Bajaj, Michael T McMahon, Christopher M Dobson, and Robert G Griffin. High-resolution molecular structure of a peptide in an amyloid fibril determined by magic angle spinning NMR spectroscopy. *Proceedings of the National Academy of Sciences of the United States of America*, 101(3):711–6, January 2004.

[12] Robert Tycko. Molecular structure of amyloid fibrils: insights from solid-state NMR. *Quarterly reviews of biophysics*, 39(1):1–55, February 2006.

[13] David L. Jakeman, Dan J. Mitchell, Wendy A. Shuttleworth, and Jeremy N. S. Evans. Effects of sample preparation conditions on biomolecular solid-state NMR lineshapes. *Journal of biomolecular NMR*, 12(3):417–21, October 1998.

[14] Danforth P. Miller, Rebeccah E. Anderson, and Juan J. de Pablo. Stabilization of lactate dehydrogenase following freeze thawing and vacuum-drying in the presence of trehalose and borate. *Pharmaceutical research*, 15(8):1215–21, August 1998.

[15] Rachel W. Martin and Kurt W. Zilm. Preparation of protein nanocrystals and their characterization by solid state NMR. *Journal of Magnetic Resonance*, 165(1):162–174, November 2003.

[16] S K Straus, T Bremi, and R R Ernst. Experiments and strategies for the assignment of fully 13C/15N-labelled polypeptides by solid state NMR. *Journal of biomolecular NMR*, 12(1):39–50, July 1998.

[17] M Hong. Resonance assignment of 13C/15N labeled solid proteins by two- and three-dimensional magic-angle-spinning NMR. *Journal of biomolecular NMR*, 15(1):1–14, September 1999.

[18] Ann E. McDermott, Tatyana Polenova, Anja Bockmann, Kurt W. Zilm, Eric K. Paulson, Rachel W. Martin, Gaetano T. Montelione, and Erin K. Paulsen. Partial NMR assignments for uniformly (13C, 15N)-enriched BPTI in the solid state. *Journal of biomolecular NMR*, 16(3):209–19, March 2000.

[19] A Detken, E H Hardy, M Ernst, M Kainosho, T Kawakami, S Aimoto, and B H Meier. Methods for sequential resonance assignment in solid, uniformly 13C, 15N labelled peptides: quantification and application to antamanide. *Journal of biomolecular NMR*, 20(3):203–21, July 2001.

[20] Anja Böckmann, Adam Lange, Anne Galinier, Sorin Luca, Nicolas Giraud, Michel Juy, Henrike Heise, Roland Montserret, François Penin, and Marc Baldus. Solid state NMR sequential resonance assignments and conformational analysis of the 2x10.4 kDa dimeric form of the Bacillus subtilis protein Crh. *Journal of biomolecular NMR*, 27(4):323–39, December 2003.

[21] Jutta Pauli, Marc Baldus, Barth-Jan van Rossum, Huub J. M. de Groot, and Hartmut Oschkinat. Backbone and side-chain 13C and 15N signal assignments of the alpha-spectrin SH3 domain by magic angle spinning solid-state NMR at 17.6 Tesla. *Chembiochem : a European journal of chemical biology*, 2(4):272–81, April 2001.

[22] Chad M Rienstra, Lisa Tucker-Kellogg, Christopher P Jaroniec, Morten Hohwy, Bernd Reif, Michael T McMahon, Bruce Tidor, Tomas Lozano-Pérez, and Robert G Griffin. De novo determination of peptide structure with solid-state magic-angle spinning NMR spectroscopy. *Proceedings of the National Academy of Sciences of the United States of America*, 99(16):10260–5, August 2002.

[23] Federica Castellani, Barth van Rossum, Annette Diehl, Mario Schubert, Kristina Rehbein, and Hartmut Oschkinat. Structure of a protein determined by solid-state magic-angle-spinning NMR spectroscopy. *Nature*, 420(6911):98–102, November 2002.

[24] Federica Castellani, Barth-Jan van Rossum, Annette Diehl, Kristina Rehbein, and Hartmut Oschkinat. Determination of solid-state NMR structures of proteins by means of three-dimensional 15N-13C-13C dipolar correlation spectroscopy and chemical shift analysis. *Biochemistry*, 42(39):11476–83, October 2003.

[25] Adam Lange, Karin Giller, Soenke Hornig, Marie-F. Martin-Eauclaire, Stefan Becker, and Marc Baldus. Toxin-induced conformational changes in a potassium channel revealed by solid-state NMR. *Nature*, 440(April):959–962, 2006.

[26] Stephan G. Zech, A. Joshua Wand, and Ann E. McDermott. Protein structure determination by high-resolution solid-state NMR spectroscopy: application to microcrystalline ubiquitin. *Journal of the American Chemical Society*, 127(24):8618–26, June 2005.

[27] Kentaro Iwata, Toshimichi Fujiwara, Yoh Matsuki, Hideo Akutsu, Satoshi Takahashi, Hironobu Naiki, and Yuji Goto. 3D structure of amyloid protofilaments of beta2-microglobulin fragment probed by solid-state NMR. *Proceedings of the National Academy of Sciences of the United States of America*, 103(48):18119–24, November 2006.

[28] Swapna Ganapathy, Adriaan J. van Gammeren, Frans B. Hulsbergen, and Huub J. M. de Groot. Probing secondary, tertiary, and quaternary structure along with protein-cofactor interactions for a helical transmembrane protein complex through 1H spin diffusion with MAS NMR spectroscopy. *Journal of the American Chemical Society*, 129(6):1504–5, February 2007.

[29] Donghua H. Zhou, John J. Shea, Andrew J. Nieuwkoop, W. Trent Franks, Benjamin J. Wylie, Charles Mullen, Dennis Sandoz, and Chad M. Rienstra. Solid-State Protein-Structure Determination with Proton-Detected Triple-Resonance 3D Magic-Angle-Spinning NMR Spectroscopy. *Angewandte Chemie International Edition*, 46(44):8380–8383, November 2007.

[30] Antoine Loquet, Benjamin Bardiaux, Carole Gardiennet, Christophe Blanchet, Marc Baldus, Michael Nilges, Thérèse Malliavin, and Anja Böckmann. 3D structure determination of the Crh protein from highly ambiguous solid-state NMR restraints. *Journal of the American Chemical Society*, 130(11):3579–89, March 2008.

[31] Theofanis Manolikas, Torsten Herrmann, and Beat H. Meier. Protein Structure Determination from 13 C Spin-Diffusion Solid-State NMR Spectroscopy. *Journal of the American Chemical Society*, 130(12):3959–3966, March 2008.

[32] Christian Wasmer, Adam Lange, Hélène Van Melckebeke, Ansgar B Siemer, Roland Riek, and Beat H Meier. Amyloid fibrils of the HET-s(218-289) prion form a beta solenoid with a triangular hydrophobic core. *Science (New York, N.Y.)*, 319(5869):1523–6, March 2008.

[33] Anne Lesage, Michel Bardet, and Lyndon Emsley. Through-Bond Carbon-Carbon Connectivities in Disordered Solids by NMR. *Journal of the American Chemical Society*, 121(47):10987–10993, December 1999.

[34] Sylvian Cadars, Julien Sein, Luminita Duma, Anne Lesage, Tran N Pham, Jay H Baltisberger, Steven P Brown, and Lyndon Emsley. The refocused INADEQUATE MAS NMR experiment in multiple spin-systems: interpreting observed correlation peaks and optimising lineshapes. *Journal of magnetic resonance (San Diego, Calif. : 1997)*, 188(1):24–34, September 2007.

[35] W. Trent Franks, Donghua H. Zhou, Benjamin J. Wylie, Brian G. Money, Daniel T. Graesser, Heather L. Frericks, Gurmukh Sahota, and Chad M Rienstra. Magic-angle spinning solid-state NMR spectroscopy of the beta1 immunoglobulin binding domain of protein G (GB1): 15N and 13C chemical shift assignments and conformational analysis. *Journal of the American Chemical Society*, 127(35):12291–305, September 2005.

[36] Józef R Lewandowski, Julien Sein, Hans Jürgen Sass, Stephan Grzesiek, Martin Blackledge, and Lyndon Emsley. Measurement of site-specific 13C spin-lattice relaxation in a crystalline protein. *Journal of the American Chemical Society*, 132(24):8252–4, June 2010.

[37] B M Fung, A K Khitrin, and K Ermolaev. An improved broadband decoupling sequence for liquid crystals and solids. *Journal of magnetic resonance (San Diego, Calif. : 1997)*, 142(1):97–101, January 2000.

[38] Paul Schanda, Matthias Huber, René Verel, Matthias Ernst, and Beat H. Meier. Direct Detection of 3h JNC' Hydrogen-Bond Scalar Couplings in Proteins by Solid-State NMR Spectroscopy. *Angewandte Chemie International Edition*, 48(49):9322–9325, November 2009.

[39] Wolfgang Bermel, Ivano Bertini, Isabella C Felli, Manolis Matzapetakis, Roberta Pierattelli, Elizabeth C Theil, and Paola Turano. A method for C(alpha) direct-detection in

protonless NMR. *Journal of magnetic resonance (San Diego, Calif. : 1997)*, 188(2):301–10, October 2007.

[40] Wolfgang Bermel, Isabella C. Felli, Rainer Kümmerle, and Roberta Pierattelli. 13C Direct-detection biomolecular NMR. *Concepts in Magnetic Resonance Part A*, 32A(3):183–200, May 2008.

[41] Ovidiu C. Andronesi, Stefan Becker, Karsten Seidel, Henrike Heise, Howard S. Young, and Marc Baldus. Determination of membrane protein structure and dynamics by magic-angle-spinning solid-state NMR spectroscopy. *Journal of the American Chemical Society*, 127(37):12965–74, September 2005.

[42] E. Purcell, H. Torrey, and R. Pound. Resonance Absorption by Nuclear Magnetic Moments in a Solid. *Physical Review*, 69(1-2):37–38, January 1946.

[43] F. Bloch. Nuclear Induction. *Physical Review*, 70(7-8):460–474, October 1946.

[44] Clare P Grey and Robert Tycko. Solid-State NMR in biological and materials physics. *Physics Today*, (September):44—-49, 2009.

[45] A Bockmann. Structural and dynamic studies of proteins by high-resolution solid-state NMR. *Comptes Rendus Chimie*, 9(3-4):381–392, March 2006.

[46] Thomas J. Offerdahl. Solid-state nuclear magnetic resonance spectroscopy for analyzing polymorphic drug forms and formulations. *Pharm. Technol*, 30(2):s24—-s42, 2006.

[47] David L. Bryce, Guy M. Bernard, Myrlene Gee, Michael D. Lumsden, Klaus Eichele, and Roderick E. Wasylishen. ChemInform Abstract: Practical Aspects of Modern Routine Solid-State Multinuclear Magnetic Resonance Spectroscopy: One-Dimensional Experiments. *ChemInform*, 33(20):no–no, May 2010.

[48] Chad M. Rienstra, Morten Hohwy, Mei Hong, and Robert G. Griffin. 2D and 3D 15N-13C-13C NMR Chemical Shift Correlation Spectroscopy of Solids: Assignment of MAS Spectra of Peptides. *Journal of the American Chemical Society*, 122(44):10979–10990, November 2000.

[49] Kurt Wüthrich. *NMR of Proteins and Nucleic Acids*. John Wiley & Sons, New York, 1st edition, 1986.

[50] Beverly R. Seavey, Elizabeth A. Farr, William M. Westler, and John L. Markley. A relational database for sequence-specific protein NMR data. *Journal of Biomolecular NMR*, 1(3):217–236, September 1991.

[51] Patrick M Schaeffer, Madeleine J Headlam, and Nicholas E Dixon. Protein–protein interactions in the eubacterial replisome. *IUBMB life*, 57(1):5–12, January 2005.

[52] Eugene F DeRose, Dawei Li, Thomas Darden, Scott Harvey, Fred W Perrino, Roel M Schaaper, and Robert E London. Model for the catalytic domain of the proofreading epsilon subunit of Escherichia coli DNA polymerase III based on NMR structural data. *Biochemistry*, 41(1):94–110, January 2002.

[53] Samir Hamdan, Esther M Bulloch, Phillip R Thompson, Jennifer L Beck, Ji Yeon Yang, Jeffrey a Crowther, Penelope E Lilley, Paul D Carr, David L Ollis, Susan E Brown, and Nicholas E Dixon. Hydrolysis of the 5'-p-nitrophenyl ester of TMP by the proofreading exonuclease (epsilon) subunit of Escherichia coli DNA polymerase III. *Biochemistry*, 41(16):5266–5275, April 2002.

[54] Samir Hamdan, Paul D Carr, Susan E Brown, David L Ollis, and Nicholas E Dixon. Structural basis for proofreading during replication of the Escherichia coli chromosome. *Structure (London, England : 1993)*, 10(4):535–546, April 2002.

[55] Guido Pintacuda, Ah Young Park, Max a Keniry, Nicholas E Dixon, and Gottfried Otting. Lanthanide labeling offers fast NMR approach to 3D structure determinations of protein-protein complexes. *Journal of the American Chemical Society*, 128(11):3696–3702, March 2006.

[56] John A. Stringer, Charles E. Bronnimann, Charles G. Mullen, Donghua H. Zhou, Sara A. Stellfox, Ying Li, Evan H. Williams, and Chad M. Rienstra. Reduction of RF-induced sample heating with a scroll coil resonator structure for solid-state NMR probes. *Journal of magnetic resonance (San Diego, Calif. : 1997)*, 173(1):40–8, March 2005.

[57] Donghua H. Zhou, Gautam Shah, Mircea Cormos, Charles Mullen, Dennis Sandoz, and Chad M. Rienstra. Proton-detected solid-state NMR spectroscopy of fully protonated proteins at 40 kHz magic-angle spinning. *Journal of the American Chemical Society*, 129(38):11791–801, September 2007.

[58] Ségolène Laage, Joseph R Sachleben, Stefan Steuernagel, Roberta Pierattelli, Guido Pintacuda, and Lyndon Emsley. Fast acquisition of multi-dimensional spectra in solid-state NMR enabled by ultra-fast MAS. *Journal of magnetic resonance (San Diego, Calif. : 1997)*, 196(2):133–41, February 2009.

[59] Ségolène Laage, Alessandro Marchetti, Julien Sein, Roberta Pierattelli, Hans Juergen Sass, Stephan Grzesiek, Anne Lesage, Guido Pintacuda, and Lyndon Emsley. Band-selective 1H-13C cross-polarization in fast magic angle spinning solid-state NMR spectroscopy. *Journal of the American Chemical Society*, 130(51):17216–7, December 2008.

[60] Ivano Bertini, Lyndon Emsley, Moreno Lelli, Claudio Luchinat, Jiafei Mao, and Guido Pintacuda. Ultrafast MAS Solid-State NMR Permits Extensive 13 C and 1 H Detection in Paramagnetic Metalloproteins. *Journal of the American Chemical Society*, 132(16):5558–5559, April 2010.

[61] Vinesh Vijayan, Jean-Philippe Demers, Jacek Biernat, Eckhard Mandelkow, Stefan Becker, and Adam Lange. Low-power solid-state NMR experiments for resonance assignment under fast magic-angle spinning. *Chemphyschem : a European journal of chemical physics and physical chemistry*, 10(13):2205–8, September 2009.

[62] Donghua H. Zhou, Gautam Shah, Charles Mullen, Dennis Sandoz, and Chad M. Rienstra. Proton-detected solid-state NMR spectroscopy of natural-abundance peptide and protein pharmaceuticals. *Angewandte Chemie (International ed. in English)*, 48(7):1253–6, January 2009.

[63] Jean-Philippe Demers, Veniamin Chevelkov, and Adam Lange. Progress in correlation spectroscopy at ultra-fast magic-angle spinning: basic building blocks and complex experiments for the study of protein structure and dynamics. *Solid state nuclear magnetic resonance*, 40(3):101–13, October 2011.

[64] Sarah D Cady, Klaus Schmidt-Rohr, Jun Wang, Cinque S Soto, William F Degrado, and Mei Hong. Structure of the amantadine binding site of influenza M2 proton channels in lipid bilayers. *Nature*, 463(7281):689–92, February 2010.

[65] Emeline Barbet-Massin, Stefano Ricagno, Józef R. Lewandowski, Sofia Giorgetti, Vittorio Bellotti, Martino Bolognesi, Lyndon Emsley, and Guido Pintacuda. Fibrillar vs Crystalline Full-Length β-2-Microglobulin Studied by High-Resolution Solid-State NMR Spectroscopy. *Journal of the American Chemical Society*, 132(16):5556–5557, April 2010.

[66] Matthias Ernst, Ago Samoson, and Beat H Meier. Low-power decoupling in fast magic-angle spinning NMR. *Chemical Physics Letters*, 348(3-4):293–302, November 2001.

[67] Matthias Ernst, Ago Samoson, and Beat H Meier. Low-power XiX decoupling in MAS NMR experiments. *Journal of Magnetic Resonance*, 163(2):332–339, August 2003.

[68] Matthias Ernst, Marcel A. Meier, Tiit Tuherm, Ago Samoson, and Beat H. Meier. Low-Power High-Resolution Solid-State NMR of Peptides and Proteins. *Journal of the American Chemical Society*, 126(15):4764–4765, April 2004.

[69] Mrignayani Kotecha, Nalinda P. Wickramasinghe, and Yoshitaka Ishii. Efficient low-power heteronuclear decoupling in13C high-resolution solid-state NMR under fast magic angle spinning. *Magnetic Resonance in Chemistry*, 45(S1):S221–S230, December 2007.

[70] Lingling Chen, J Michael Kaiser, Tatyana Polenova, Jun Yang, Chad M Rienstra, and Leonard J Mueller. Backbone assignments in solid-state proteins using J-based 3D heteronuclear correlation spectroscopy. *Journal of the American Chemical Society*, 129(35):10650–1, September 2007.

[71] Lingling Chen, J. Michael Kaiser, Jinfeng Lai, Tatyana Polenova, Jun Yang, Chad M. Rienstra, and Leonard J. Mueller. J-based 2D homonuclear and heteronuclear correlation

in solid-state proteins. *Magnetic Resonance in Chemistry*, 45(S1):S84–S92, December 2007.

[72] Sorin Luca, Henrike Heise, and Marc Baldus. High-resolution solid-state NMR applied to polypeptides and membrane proteins. *Accounts of chemical research*, 36(11):858–65, December 2003.

[73] Marc Baldus and Beat H. Meier. Total Correlation Spectroscopy in the Solid State. The Use of Scalar Couplings to Determine the Through-Bond Connectivity. *Journal of Magnetic Resonance, Series A*, 121(1):65–69, July 1996.

[74] Anne Lesage, Céline Auger, Stefano Caldarelli, and Lyndon Emsley. Determination of Through-Bond Carbon-Carbon Connectivities in Solid-State NMR Using the INADEQUATE Experiment. *Journal of the American Chemical Society*, 119(33):7867–7868, August 1997.

[75] Anne Lesage and Lyndon Emsley. Through-bond heteronuclear single-quantum correlation spectroscopy in solid-state NMR, and comparison to other through-bond and through-space experiments. *Journal of magnetic resonance (San Diego, Calif. : 1997)*, 148(2):449–54, February 2001.

[76] Edme H Hardy, Andreas Detken, and Beat H Meier. Fast-MAS total through-bond correlation spectroscopy using adiabatic pulses. *Journal of magnetic resonance (San Diego, Calif. : 1997)*, 165(2):208–18, December 2003.

[77] Bénédicte Elena, Anne Lesage, Stefan Steuernagel, Anja Böckmann, and Lyndon Emsley. Proton to carbon-13 INEPT in solid-state NMR spectroscopy. *Journal of the American Chemical Society*, 127(49):17296–302, December 2005.

[78] Lingling Chen, Ryan A. Olsen, Douglas W. Elliott, John M. Boettcher, Donghua H. Zhou, Chad M. Rienstra, and Leonard J. Mueller. Constant-Time Through-Bond 13 C Correlation Spectroscopy for Assigning Protein Resonances with Solid-State NMR Spectroscopy. *Journal of the American Chemical Society*, 128(31):9992–9993, August 2006.

[79] Antoine Loquet, Ségolène Laage, Carole Gardiennet, Bénédicte Elena, Lyndon Emsley, Anja Böckmann, and Anne Lesage. Methyl proton contacts obtained using heteronuclear through-bond transfers in solid-state NMR spectroscopy. *Journal of the American Chemical Society*, 130(32):10625–32, August 2008.

[80] Marc Baldus, Aneta T Petkova, Judith Herzfeld, and Robert G. Griffin. Cross polarization in the tilted frame: assignment and spectral simplification in heteronuclear spin systems. *Molecular Physics*, 95(6):1197–1207, December 1998.

[81] Donghua H. Zhou, Kathryn D. Kloepper, Kem A. Winter, and Chad M. Rienstra. Band-selective 13C homonuclear 3D spectroscopy for solid proteins at high field with rotor-synchronized soft pulses. *Journal of biomolecular NMR*, 34(4):245–57, April 2006.

[82] Guido Pintacuda, Nicolas Giraud, Roberta Pierattelli, Anja Böckmann, Ivano Bertini, and Lyndon Emsley. Solid-state NMR spectroscopy of a paramagnetic protein: assignment and study of human dimeric oxidized CuII-ZnII superoxide dismutase (SOD). *Angewandte Chemie (International ed. in English)*, 46(7):1079–1082, January 2007.

[83] Marc Baldus, M. Tomaselli, Beat H. Meier, and Richard R. Ernst. Broadband polarization-transfer experiments for rotating solids. *Chemical Physics Letters*, 230(4-5):329–336, December 1994.

[84] Edward O. Stejskal, Jacob Schaefer, and John S. Waugh. Magic-angle spinning and polarization transfer in proton-enhanced NMR. *Journal of Magnetic Resonance (1969)*, 28(1):105–112, October 1977.

[85] Elisabetta Chiarparin, Philippe Pelupessy, and Geoffrey Bodenhausen. Selective cross-polarization in solution state NMR. *Molecular Physics*, 95(5):759–767, December 1998.

[86] Beat H. Meier. Cross polarization under fast magic angle spinning: thermodynamical considerations. *Chemical Physics Letters*, 188(3-4):201–207, January 1992.

[87] David Marks and Shimon Vega. A Theory for Cross-Polarization NMR of Nonspinning and Spinning Samples. *Journal of Magnetic Resonance, Series A*, 118(2):157–172, February 1996.

[88] René Verel, Marc Baldus, Matthias Ernst, and Beat H. Meier. A homonuclear spin-pair filter for solid-state NMR based on adiabatic-passage techniques. *Chemical Physics Letters*, 287(3-4):421–428, May 1998.

[89] Andreas Detken, Edme H. Hardy, Matthias Ernst, and Beat H. Meier. Simple and efficient decoupling in magic-angle spinning solid-state NMR: the XiX scheme. *Chemical Physics Letters*, 356(3-4):298–304, April 2002.

[90] Nalinda P. Wickramasinghe, Mrignayani Kotecha, Ago Samoson, Jaan Past, and Yoshitaka Ishii. Sensitivity enhancement in (13)C solid-state NMR of protein microcrystals by use of paramagnetic metal ions for optimizing (1)H T(1) relaxation. *Journal of magnetic resonance (San Diego, Calif. : 1997)*, 184(2):350–6, February 2007.

[91] Anne Lesage. Indirect Coupling and Connectivity. In R.K. Harris and R.˜E.: Wasylishen, editors, *Encyclopedia of Magnetic Resonanc*. John Wiley {&} Sons Inc., Chichester, 2008.

[92] René Verel, Jacco D. van Beek, and Beat H. Meier. INADEQUATE-CR experiments in the solid state. *Journal of magnetic resonance (San Diego, Calif. : 1997)*, 140(1):300–3, September 1999.

[93] Gaël De Paëpe, Nicolas Giraud, Anne Lesage, Paul Hodgkinson, Anja Böckmann, and Lyndon Emsley. Transverse dephasing optimized solid-state NMR spectroscopy. *Journal of the American Chemical Society*, 125(46):13938–9, November 2003.

[94] René Verel, Theofanis Manolikas, Ansgar B Siemer, and Beat H Meier. Improved resolution in (13)C solid-state spectra through spin-state-selection. *Journal of magnetic resonance (San Diego, Calif. : 1997)*, 184(2):322–9, February 2007.

[95] Rasmus Linser, Uwe Fink, and Bernd Reif. Proton-detected scalar coupling based assignment strategies in MAS solid-state NMR spectroscopy applied to perdeuterated proteins. *Journal of Magnetic Resonance*, 193(1):89–93, July 2008.

[96] Daniel Lee, Jochem Struppe, Douglas W Elliott, Leonard J Mueller, and Jeremy J Titman. Sensitive absorptive refocused scalar correlation NMR spectroscopy in solids. *Physical chemistry chemical physics : PCCP*, 11(18):3547–53, May 2009.

[97] Ye Tian, Lingling Chen, Dimitri Niks, J Michael Kaiser, Jinfeng Lai, Chad M Rienstra, Michael F Dunn, and Leonard J Mueller. J-Based 3D sidechain correlation in solid-state proteins. *Physical chemistry chemical physics : PCCP*, 11(32):7078–86, August 2009.

[98] Anne Lesage. Recent advances in solid-state NMR spectroscopy of spin I=1/2 nuclei. *Physical chemistry chemical physics : PCCP*, 11(32):6876–91, August 2009.

[99] Luminita Duma, Sabine Hediger, Bernhard Brutscher, Anja Böckmann, and Lyndon Emsley. Resolution Enhancement in Multidimensional Solid-State NMR Spectroscopy of Proteins Using Spin-State Selection. *Journal of the American Chemical Society*, 125(39):11816–11817, October 2003.

[100] Veniamin Chevelkov, Zhongjing Chen, Wolfgang Bermel, and Bernd Reif. Resolution enhancement in MAS solid-state NMR by application of 13C homonuclear scalar decoupling during acquisition. *Journal of magnetic resonance (San Diego, Calif. : 1997)*, 172(1):56–62, January 2005.

[101] Tatyana I. Igumenova and Ann E. McDermott. Homo-nuclear 13C J-decoupling in uniformly 13C-enriched solid proteins. *Journal of Magnetic Resonance (San Diego, Calif. : 1997)*, 175(1):11–20, July 2005.

[102] Ingo Scholz, Stefan Jehle, Peter Schmieder, Matthias Hiller, Frank Eisenmenger, Hartmut Oschkinat, and Barth-Jan van Rossum. J-deconvolution using maximum entropy reconstruction applied to 13C-13C solid-state cross-polarization magic-angle-spinning NMR of proteins. *Journal of the American Chemical Society*, 129(21):6682–3, May 2007.

[103] Ségolène Laage, Anne Lesage, Lyndon Emsley, Ivano Bertini, Isabella C Felli, Roberta Pierattelli, and Guido Pintacuda. Transverse-dephasing optimized homonuclear j-

decoupling in solid-state NMR spectroscopy of uniformly 13C-labeled proteins. *Journal of the American Chemical Society*, 131(31):10816–7, August 2009.

[104] Yoshitaka Ishii, James P. Yesinowski, and Robert Tycko. Sensitivity Enhancement in Solid-State 13 C NMR of Synthetic Polymers and Biopolymers by 1 H NMR Detection with High-Speed Magic Angle Spinning. *Journal of the American Chemical Society*, 123(12):2921–2922, March 2001.

[105] Eric K. Paulson, Corey R. Morcombe, Vadim Gaponenko, Barbara Dancheck, R. Andrew Byrd, and Kurt W. Zilm. Sensitive high resolution inverse detection NMR spectroscopy of proteins in the solid state. *Journal of the American Chemical Society*, 125(51):15831–15836, December 2003.

[106] Veniamin Chevelkov, Kristina Rehbein, Anne Diehl, and Bernd Reif. Ultrahigh resolution in proton solid-state NMR spectroscopy at high levels of deuteration. *Angewandte Chemie (International ed. in English)*, 45(23):3878–81, June 2006.

[107] Bernd Reif, Christopher P. Jaroniec, Chad M. Rienstra, Morten Hohwy, and Robert G. Griffin. 1H-1H MAS correlation spectroscopy and distance measurements in a deuterated peptide. *Journal of magnetic resonance (San Diego, Calif. : 1997)*, 151(2):320–7, August 2001.

[108] Rasmus Linser, Benjamin Bardiaux, Victoria Higman, Uwe Fink, and Bernd Reif. Structure calculation from unambiguous long-range amide and methyl 1H-1H distance restraints for a microcrystalline protein with MAS solid-state NMR spectroscopy. *Journal of the American Chemical Society*, 133(15):5905–12, April 2011.

[109] Matthias Huber, Sebastian Hiller, Paul Schanda, Matthias Ernst, Anja Böckmann, René Verel, and Beat H Meier. A proton-detected 4D solid-state NMR experiment for protein structure determination. *Chemphyschem : a European journal of chemical physics and physical chemistry*, 12(5):915–8, April 2011.

[110] Michael J Knight, Amy L Webber, Andrew J Pell, Paul Guerry, Emeline Barbet-Massin, Ivano Bertini, Isabella C Felli, Leonardo Gonnelli, Roberta Pierattelli, Lyndon Emsley, Anne Lesage, Torsten Herrmann, and Guido Pintacuda. Fast resonance assignment and fold determination of human superoxide dismutase by high-resolution proton-detected solid-state MAS NMR spectroscopy. *Angewandte Chemie (International ed. in English)*, 50(49):11697–701, December 2011.

[111] Jozef R. Lewandowski, Jean-Nicolas Dumez, Umit Akbey, Sascha Lange, Lyndon Emsley, and Hartmut Oschkinat. Enhanced Resolution and Coherence Lifetimes in the Solid-State NMR Spectroscopy of Perdeuterated Proteins under Ultrafast Magic-Angle Spinning. *The Journal of Physical Chemistry Letters*, 2(17):2205–2211, September 2011.

[112] Michael J Knight, Andrew J Pell, Ivano Bertini, Isabella C. Felli, Leonardo Gonnelli, Roberta Pierattelli, Torsten Herrmann, Lyndon Emsley, and Guido Pintacuda. Structure and site-specific backbone dynamics of a paramagnetic metalloprotein. *Proc. Natl. Acad. Sci. USA*, page in press, 2012.

[113] Lu-Yun Lian and David A Middleton. Labelling approaches for protein structural studies by solution-state and solid-state NMR. *Progress in Nuclear Magnetic Resonance Spectroscopy*, 39(3):171–190, October 2001.

[114] K H Gardner and L E Kay. The use of 2H, 13C, 15N multidimensional NMR to study the structure and dynamics of proteins. *Annual review of biophysics and biomolecular structure*, 27:357–406, January 1998.

[115] Savvas N. Savvides, Srinivasan Raghunathan, Klaus Fütterer, Alex G. Kozlov, Timothy M. Lohman, and Gabriel Waksman. The C-terminal domain of full-length E. coli SSB is disordered even when bound to DNA. *Protein science : a publication of the Protein Society*, 13(7):1942–7, July 2004.

[116] Gregory Metz, Xueli Wu, and Steven O. Smith. Ramped-Amplitude Cross Polarization in Magic-Angle-Spinning NMR. *Journal of Magnetic Resonance, Series A*, 110(2):219–227, October 1994.

[117] Ivano Bertini, Lyndon Emsley, Isabella C. Felli, Ségolène Laage, Anne Lesage, Józef R. Lewandowski, Alessandro Marchetti, Roberta Pierattelli, and Guido Pintacuda. High-resolution and sensitivity through-bond correlations in ultra-fast magic angle spinning (MAS) solid-state NMR. *Chemical Science*, 2(2):345, 2011.

[118] Amy L Webber, Andrew J Pell, Emeline Barbet-Massin, Michael J Knight, Ivano Bertini, Isabella C Felli, Roberta Pierattelli, Lyndon Emsley, Anne Lesage, and Guido Pintacuda. Combination of DQ and ZQ Coherences for Sensitive Through-Bond NMR Correlation Experiments in Biosolids under Ultra-Fast MAS. *Chemphyschem : a European journal of chemical physics and physical chemistry*, April 2012.

[119] Tatyana I. Igumenova, A. Joshua Wand, and Ann E. McDermott. Assignment of the backbone resonances for microcrystalline ubiquitin. *Journal of the American Chemical Society*, 126(16):5323–31, April 2004.

[120] Anja Böckmann. 3D protein structures by solid-state NMR spectroscopy: ready for high resolution. *Angewandte Chemie (International ed. in English)*, 47(33):6110–3, January 2008.

[121] D. Demus, J. Goodby, G. W. Gray, H.-W. Spiess, and V. Vill, editors. *Handbook of Liquid Crystals Set*. Wiley-VCH Verlag GmbH, Weinheim, Germany, February 1998.

[122] F. Reinitzer. History of Liquid Crystals. *Ann. Phys. (Leipzig)*, pages 213–224, 1909.

[123] Sven T Lagerwall. *Ferroelectric and Antiferroelectric Liquid Crystals*. Wiley-VCH, 1999.

[124] Jan P F Lagerwall and Frank Giesselmann. Current topics in smectic liquid crystal research. *Chemphyschem : a European journal of chemical physics and physical chemistry*, 7(1):20–45, January 2006.

[125] Michael Krueger and Frank Giesselmann. Dielectric spectroscopy of de Vries-type smectic-A* -smectic-C* transitions. *Physical review. E, Statistical, nonlinear, and soft matter physics*, 71(4 Pt 1):041704, April 2005.

[126] Adriaan De Vries. The description of the smectic A and C phases and the smectic A-C phase transition of TCOOB with a diffuse-cone model. *J. Chem. Phys.*, 25:71–78, 1979.

[127] Adriaan De Vries. Experimental Evidence Concerning Two Different Kinds of Smectic C to Smectic A Transitions. *Molecular Crystals and Liquid Crystals*, 41(2):27–31, September 1977.

[128] Adriaan De Vries. X-Ray Photographic Studies of Liquid Crystals: II. Apparent Molecular Length and Thickness in Three Phases of Ethyl- p -ethoxybenzal- p -aminobenzoate. *Molecular Crystals and Liquid Crystals*, 11(4):361–383, November 1970.

[129] Karl Saunders. de Vries behavior of the electroclinic effect in the smectic-A* phase near a biaxiality-induced smectic-A*-smectic-C* tricritical point. *Physical Review E*, 80(1), July 2009.

[130] Miroslav Kaspar, Vera Hamplova, Sergiy A. Pakhomov, Alexej M. Bubnov, Frederic Guittard, Helmut Sverenyak, Ivan Stibor, Premysl Vanek, and Milada Glogarova. New series of ferroelectric liquid crystals with four ester groups. *Liquid Crystals*, 24(4):599–605, April 1998.

[131] S. Diele, P. Brand, and H. Sackmann. X-ray Diffraction and Polymorphism of Smectic Liquid Crystals 1. A-, B- and C-modifications. *Molecular Crystals and Liquid Crystals*, 16(1-2):105–116, February 1972.

[132] Alessandro Marchetti, Valentina Domenici, Vladimira Novotna, Moreno Lelli, and Mario Cifelli. Direct Measure of the Tilt Angle in de Vries-Type Liquid Crystals through NMR Spectroscopy. *ChemPhysChem*, pages 1641–1645, 2010.

[133] U. Manna, Jang-Kun Song, J. Vij, and J. Naciri. Electric-field-dependent dielectric response in the de Vries-type smectic-A* phase possessing local orientational order with nanoscale correlation length. *Physical Review E*, 78(4), October 2008.

[134] Stephen Garoff and Robert B. Meyer. Electroclinic Effect at the A-C Phase Change in a Chiral Smectic Liquid Crystal. *Phys. Rev. Lett.*, 38(15):848–851, April 1977.

[135] P G De Gennes and J Prost, editors. *The Physics of Liquid Crystals*. Clarendon Press, New York, 2nd edition, 1994.

[136] Jeffrey C. Roberts, Nadia Kapernaum, Qingxiang Song, Dorothee Nonnenmacher, Khurshid Ayub, Frank Giesselmann, and Robert P. Lemieux. Design of liquid crystals with "de Vries-like" properties: frustration between SmA- and SmC-promoting elements. *Journal of the American Chemical Society*, 132(1):364–70, January 2010.

[137] S. Krishna Prasad, D. S. Shankar Rao, Srivatsa Sridevi, Chethan Lobo, Banahalli R. Ratna, Jawad Naciri, and Ranganathan Shashidhar. Unusual Dielectric and Electrical Switching Behavior in the de Vries Smectic A Phase of Two Organosiloxane Derivatives. *Physical Review Letters*, 102(14):147802, April 2009.

[138] R. Bartolino, J. Doucet, and G. Durand. Molecular Tilt in Smectic-C Phase - Zigzag Model. *Ann. Phys. (Paris)*, 3:389–395, 1978.

[139] Valentina Domenici, Mario Geppi, and Carlo Alberto Veracini. NMR in chiral and achiral smectic phases: Structure, orientational order and dynamics. *Prog. Nucl. Magn. Reson. Spectrosc.*, 50:1, 2007.

[140] Valentina Domenici, Alberto Marini, Carlo Alberto Veracini, Jing Zhang, and Ronald Y Dong. Effect of the magnetic field on the supramolecular structure of chiral smectic C phases: (2)H NMR studies. *Chemphyschem : a European journal of chemical physics and physical chemistry*, 8(18):2575–87, December 2007.

[141] Valentina Domenici. *Orentational Order and Dynamics by means of 2H-NMR on rod-like and banana-shaped liquid crystals: new developments*. PhD thesis, Universitá degli Studi di Pisa, 2004.

[142] Samuel Bezner, Michael Krueger, Vera Hamplová, Milada Glogarová, and Frank Giesselmann. Nature of smectic A$ˆ{*}$-C$ˆ{*}$ phase transitions in a series of ferroelectric liquid crystals with little smectic layer shrinkage. *The Journal of chemical physics*, 126(5):054902, February 2007.

[143] F. Giesselmann, P. Zugenmaier, I. Dierking, S. Lagerwall, B. Stebler, M. Kašpar, V. Hamplová, and M. Glogarová. Smectic-Aˆ{*}-smectic-Cˆ{*} transition in a ferroelectric liquid crystal without smectic layer shrinkage. *Physical Review E*, 60(1):598–602, July 1999.

[144] Valentina Domenici. Order and dynamics of rod-like and banana-shaped liquid crystals by 2H NMR. *Pure Appl. Chem.*, 79(1):21–37, 2007.

[145] Alberto Marini and Valentina Domenici. 2 H, 13 C NMR and Ab Initio Calculations Applied to the SmC* Phase: Methodology and Case Studies. *Ferroelectrics*, 395(1):46–59, April 2010.

[146] Mario Cifelli, Valentina Domenici, Alberto Marini, and Carlo Alberto Veracini. NMR studies of ferroelectric liquid crystals. *Liquid Crystals*, 37:935 – 948, 2010.

[147] Donata Catalano, Mario Cifelli, Valentina Domenici, Katalin Fodor-Csorba, Robert M. Richardson, and Carlo Alberto Veracini. 2H-NMR and SAXS of a ferroelectric liquid crystal: unwinding of the ferroelectric chiral helix by high magnetic fields. *Chemical Physics Letters*, 346(3-4):259–266, October 2001.

[148] Valentina Domenici, Carlo Alberto Veracini, Vladimira Novotná, and Ronald Y Dong. Twist grain boundary liquid-crystalline phases under the effect of the magnetic field: a complete 2H and 13C NMR study. *Chemphyschem : a European journal of chemical physics and physical chemistry*, 9(4):556–66, March 2008.

[149] Valentina Domenici, Carlo Alberto Veracini, Katalin Fodor-Csorba, Giacomo Prampolini, Ivo Cacelli, Andrjia Lebar, and Bostjan Zalar. Banana-shaped molecules peculiarly oriented in a magnetic field: (2)H NMR spectroscopy and quantum mechanical calculations. *Chemphyschem : a European journal of chemical physics and physical chemistry*, 8(16):2321–30, November 2007.

[150] Valentina Domenici, Carlo Alberto Veracini, and Bostjan Zalar. How do banana-shaped molecules get oriented (if they do) in the magnetic field? *Soft Matter*, 1(6):408, 2005.

[151] Valentina Domenici, Lou Madsen, E. J. Choi, Edward T. Samulski, and Carlo Alberto Veracini. Investigating the core moiety of banana-shaped liquid crystals using 2H NMR coupled with quantum simulations. *Chemical Physics Letters*, 402(4-6):318–323, February 2005.

[152] Robin K. Harris, Edwin D. Becker, Sonia M. Cabral de Menezes, Pierre Granger, Roy E. Hoffman, and Kurt W. Zilm. Further conventions for NMR shielding and chemical shifts (IUPAC Recommendations 2008). *Pure and Applied Chemistry*, 80(1):59–84, 2008.

[153] Corey R. Morcombe and Kurt W. Zilm. Chemical shift referencing in MAS solid state NMR. *Journal of Magnetic Resonance*, 162(2):479–486, June 2003.

Appendix A

Chemical Shift Assignments

This appendix lists the values of chemical shifts resonances of the two form of microcrystalline ϵ_{186} subunits assigned at pH 6.0 and 9.0 respectively. These values will be deposited in the BioMagResBank (BMRB).

A.1 calibration

In order to be deposited on BMRB database, DSS calibration is used. ^{13}C resonance of on the high-frequency (methylene) carbon of adamantane in solid phase under MAS rotation is fixed to $\delta_{MAS}^{solid\ adamantane} = 40.49$ ppm. Referencing of ^{13}C chemical shifts to ^{1}H and ^{15}N shifts in MAS experiments can be done using Ξ values, as reported by IUPAC [152, 153].

A.2 Form at pH 6.0

Experiments performed on triple-resonance 3.2mm probe are listed in tables A.1, A.2 A.3, A.4.

A.3 Form at pH 9.0

Experiments performed on triple-resonance 1.3mm probe are listed in tables A.5, A.6,A.7

ϵ_{186}, 3.2 mm rotor, pH 6.0 - residues 1 to 51								
Res.	^{15}N	^{13}CO	$^{13}C\alpha$	$^{13}C\beta$	$^{13}C\gamma$	$^{13}C\delta$	$^{13}C\epsilon$	$^{13}C\zeta$
Q8		175.9	55.22	32.11				
I9	117.0	174.4	57.29	39.26	15.97	13.54		
					28.87			
V10	130.3	175	61.33	30.83	20.61			
					22.59			
L11	130.6	173.1	54.35	47.60	25.76	28.00		
					27.37			
D12	124.0	173.7	54.50	45.77				
T13	110.7	174.8	60.67	72.44	22.14			
E14	116.9	177.4	53.70	29.75				
T15	112.0	174.1	60.54	73.79	20.24			
T16	106.7	172.1	63.93	69.47	23.07			
G17	105.0	170.8	44.43					
M18	113.5	172.9	55.07	33.82	30.27		18.48	
N19	117.0	176.5	51.80	41.06				
Q20	122.4	177.7	57.33	26.74	34.91	179.9		
I21	115.4	175.7	60.00	41.03	17.36			
G22	112.2	172.8	43.79					
A23	123.0	181.7	52.35	17.26				
H24	122.8	173.9	59.42	30.83	136.5	119.0	138.8	
Y25	111.7	175.0	53.27	36.87	126.3			
E26	121.7	177.4	59.05	29.61	183.8	36.69		
G27	112.6	173.2	45.98					
H28	120.5	173.9	57.16	36.15			138.3	
K29	113.8	176.7	55.03	33.41				
I30	120.2	175.7	63.20	38.82	18.93	13.59		
I31	117.6			38.74	18.56	15.38		
					25.18			
E32	123.8	174.6	55.15	33.35	182.3			
I33	124.5	174.2	60.97	41.31	17.40	12.57		
					27.65			
G34	115.7	169.6	43.74					
A35	126.8	174.5	50.68	22.36				
V36	120.7	173.2	59.30	35.25	19.87			
					21.80			
E37	121.2	175.0	55.14	33.71		179.8		
V38	130.7	174.9	61.32	33.94	20.62			
					21.95			
V39	125.9	175.5	60.92	34.39	21.73			
N40	126.1	174.0	53.86	35.11				
R41	105.7	173.1	58.49					
R42	117.1	173.6	54.24	32.70				
L43	124.2	178.9	55.77	39.92				
T44	114.6	177.5	62.54	69.25	22.41			
G45	112.1	173.0	45.61					
N46	123.8	173.4	52.20	37.53				
N47	123.9	173.5	51.83	40.72				
F48	124.0	173.4	57.64	42.92	138.9			
H49	125.2	172.6	52.62	30.64	130.8			
V50	120.6	173.3	58.95	34.94	19.49			
Y51	121.3	178.0	57.91	41.51				

Table A.1: Solid-state chemical shift resonances (residues 1 to 51) of microcrystalline ϵ_{186}, form at pH 6.0. Crystallization condition are reported in table 3.1. Terminal residues are not assigned.
.

ϵ_{186}, 3.2 mm rotor, pH 6.0								
Res.	^{15}N	^{13}CO	^{13}Cα	^{13}Cβ	^{13}Cγ	^{13}Cδ	^{13}Cϵ	^{13}Cζ
L52	119.1	174.6	52.00	45.91	26.88			
K53	120.4	176.1	53.43	33.17	25.22			
P54	139.9	180.1	63.63	31.68		50.01		
D55	107.5			37.99				
R56	110.3	174.7	54.77	29.99				158.0
L57	119.3	178.3	54.61	42.40				
V58	124.8	175.3	63.15	33.44	20.49			
					23.33			
D59	130.4	175.7	53.57	41.26	179.5			
P60	138.2	179.5	65.66	32.09	27.80	50.65		
E61	119.1	178.6	59.47	29.79				
A62	121.3	180.5	55.04	17.56				
F63	118.4	178.7	61.39	38.72	138.1			
G64	105.4	172.6	46.20					
V65	118.3	176.6	63.89	32.73	20.84			
H66	114.0	176.0	54.13	29.49	132.9			
G67	111.4	174.5	47.08					
I68	126.8	173.9	62.48	35.98	19.21	13.02		
					27.23			
A69	127.8	178.4	51.15	20.23				
D70	119.2	179.8	58.31	41.26				
E71	116.2	178.0	59.28	29.15	36.52	181.5		
F72	118.9	175.1	59.57	39.32				
L73	115.6	177.4	54.58	41.59				
L74	114.4	177.5	57.51	42.26		22.40		
D75	115.4	176.2	52.35	39.77	180.9			
K76	120.4	173.0	52.47	27.02			38.30	
P77	132.1	176.0	61.95	32.39	26.91	49.73		
T78	107.6	177.1	60.27	71.93	22.79			
F79	121.7	177.6	62.28	38.32	139.3			
A80	117.1	179.8	55.23	19.15				
E81	115.2	177.7	58.21	30.78	37.83	184.4		
V82	110.1	176.1	60.16	32.95	20.44			
A83	123.6	178.1	56.03	19.77				
D84	116.4	177.1	58.46	39.55	180.8			
E85	122.0							
F86		177.9	59.37					
M87	118.9	177.4	60.38	33.60				
D88	118.7		57.70	39.97				
Y89								
I90		176.5	62.29	37.99	24.42			
R91	120.6	177.3	59.03	29.57				
G92	112.6	173.6	45.69					
A93	123.7	176.1	51.37	20.82				
E94	118.3	174.8	54.37	30.96	34.70	182.7		

Table A.2: Solid-state chemical shift table (residues 51 to 94) of microcrystalline ϵ_{186}, form at pH 6.0. Crystallization condition are reported in table 3.1.

.

ϵ_{186}, 3.2 mm rotor, pH 6.0								
Res.	^{15}N	^{13}CO	$^{13}C\alpha$	$^{13}C\beta$	$^{13}C\gamma$	$^{13}C\delta$	$^{13}C\epsilon$	$^{13}C\zeta$
L95	129.2	175.0	52.81	43.01	27.18	21.79		
V96	125.9	174.5	61.64	32.96	18.80			
					19.23			
I97	123.4	175.1	59.53	44.18	19.79	15.68		
					26.51			
H98	131.4	175.8	58.32	30.49	139.0			
N99	127.0	173.5	54.00	35.83				
A100	119.7	176.9	54.84	19.61				
A101	116.6	181.1	55.28	18.34				
F102	118.3	178.6	60.22					
D103	121.3	57.58	41.15					
I104	118.7	177.9	61.96	34.86	17.89	10.01		
					27.25			
G105	104.4	175.5	47.76					
F106	118.8	177.6	64.00	39.42				
M107	118.9	175.8	58.39	32.33				
D108	117.1	174.9	56.72	39.24				
Y109	121.6	179.5	59.42	38.42				
E110	120.5	181.0	59.99	26.04	34.72	181.9		
F111	118.1	180.7	60.38	37.88	139.3	131.3		
S112	119.0	177.4	61.72	62.31				
L113	124.3	178.4	56.29	41.09		21.43		
L114	114.9							
K115								
R116								
D117								
I118	120.6	174.7	59.67	39.23	15.93	13.46		
					29.04			
P119	140.1	175.5	62.01	32.88		50.78		
K120	116.3							
T121	125.0	175.3	67.70	68.42	21.38			
N122	116.4	176.3	54.08	36.92	179.1			
T123	108.9	175.6	62.79	70.51	22.04			
F124	116.7	174.5	56.36	39.26	137.3			
C125	122.6	173.2	58.95	31.28				
K126	121.4	174.8	55.26	33.52	25.52			
V127	124.0	176.6	63.53	32.78	21.44			
T128	130.2	171.5	61.83	70.21	22.01			
D129	125.0	178.0	51.32	41.55	180.7			
S130	122.0	177.0	62.21	62.52				
L131	123.6		57.35	39.11				
A132	123.1	181.0	55.37	18.29				
V133	118.1	177.7	66.43	31.83	21.54			
					21.86			
A134	122.2	178.5	55.65	17.79				
R135	117.8	178.1	59.39	29.35				
K136	118.7	178.4	58.66	32.25				
M137	116.6	177.8	57.15	32.43			15.85	
F138	115.5	3.00	58.46	38.05				

Table A.3: Solid-state chemical shift table (residues 95 to 138) of microcrystalline ϵ_{186}, form at pH 6.0. Crystallization condition are reported in table 3.1.

.

ϵ_{186}, 3.2 mm rotor, pH 6.0								
Res.	^{15}N	^{13}CO	^{13}Cα	^{13}Cβ	^{13}Cγ	^{13}Cδ	^{13}Cϵ	^{13}Cζ
P139			62.85	32.46	50.89	3.00	3.00	3.00
G140	106.6	173.8	46.55					
K141	117.0	177.2	55.09	32.75				
R142	119.0	176.0	60.06	30.70				
N143	116.7	176.0	53.79	39.68				
S144	111.7	173.5	58.56	64.21				
L145	121.2	178.0	58.29	41.30				
D146	118.0	175.3	54.06					
A147	125.0	181.5	54.94	18.10				
L148	120.3	179.1	58.11	42.40		24.42		
C149	118.5	177.0	65.10	25.30				
A150	119.7	173.8	46.55					
R151	119.8	175.3	59.42	30.11				
Y152	115.5	176.6	58.08	39.40				
E153	122.3	175.3	58.18	26.67				
I154				38.45	28.21			
D155			53.20	41.05				
N156		176.5	52.43					
S157	120.5	177.3	61.60	62.69				
K158								
R159								
T160	116.9	175.2	64.25	67.94	21.34			
L161	119.9	55.96	43.95					
H162		174.2	54.55	33.12			136.9	
G163	106.9	173.3	46.42					
A164	119.7	179.2	55.26	18.23				
L165	117.0	177.5	57.35	39.31	25.93			
L166	119.9	178.8	57.50	38.60		22.07		
						24.96		
D167	120.8	179.0	57.73	38.69				
A168	122.5	178.2	55.15	19.04				
Q169	119.2	177.8	57.71					
I170	120.5	177.9	65.48	38.10	18.91	13.20		
					28.93			
L171	119.2	179.4	57.44	39.31				
A172	121.2	178.6	56.09	17.65				
E173	115.6	180.2	59.93	30.02		178.6		
V174	120.8	176.6	66.33	32.40	22.88			
					24.90			
Y175	120.9	176.6	61.81	38.90		132.3	117.9	
L176	119.1	178.9	57.83	41.06				
A177	122.1	180.5	55.03	17.61				
M178	118.9	177.7	58.47	34.86	30.89			
T179	104.2	174.9	60.94	69.55	20.52			
G180	110.8	173.8	45.79					

Table A.4: Solid-state chemical shift resonances (residues 139 to 186) of microcrystalline ϵ_{186}, form at pH 6.0. Crystallization conditions are reported in table 3.1. Terminal residues are not assigned.

.

ϵ_{186}, 1.3 mm rotor, pH 9.0				
Res.	$^{1}H^{N}$	^{15}N	^{13}CO	$^{13}C\alpha$
I9	9.133	116.8	174.00	57.22
V10	9.209	130.4	175.0	61.03
L11	8.657	130.4	173.7	54.14
D12	9.291	122.8	173.0	54.56
T13	7.053	110.6		60.20
E14	8.526	116.5	177.1	53.76
T15	9.194	112.4	173.9	59.95
T16	8.709	106.8	171.8	63.43
G17	7.743	105.2	170.6	43.99
M18	7.884	113.9	172.7	54.46
N19	8.849	117.5	174.7	51.72
Q20	8.480	120.7		57.24
I21				60.18
G22	8.546	112.7	176.2	45.57
A23	8.152	123.5	181.3	51.92
H24	8.211	120.4	174.0	57.86
Y25	7.018	110.2	174.7	53.10
E26	5.238	120.4	177.0	58.62
G27	8.110	112.3	173.1	45.82
H28	8.441	120.9	173.6	56.59
K29	8.511	114.5	176.8	52.52
I30	9.442	121.2	175.4	62.74
I31	9.022	117.5	174.4	60.42
E32	7.377	122.5	174.4	55.13
I33	8.551	125.0	173.5	60.72
G34	8.476	115.0	169.5	43.41
A35	9.031	126.8	174.4	50.17
V36	8.053	120.3	174.3	59.30
E37	7.738	121.3	174.9	58.17
V38	9.418	130.7	174.4	61.14
V39	8.713	130.5		60.81
N40	8.673	125.9		52.67
R41				
R42				
L43				
T44				
G45	9.498	108.7	173.4	44.19
N46	8.142	118.5	173.0	52.11
N47	7.772	123.8		52.01
F48	8.676	122.0	172.9	57.23
H49	7.941	125.9	173.0	53.36
V50	7.408	120.8	171.8	59.52
Y51	7.511	121.5	178.3	57.65
L52	8.151	118.0	174.1	51.59
K53	8.091	120.5	176.4	53.03
P54				63.05
D55				
R56				
L57				
V58			174.9	
D59	9.556	130.4		53.28
P60		137.7	179.1	65.35
E61	9.087	118.8	178.5	59.15
A62	7.165	121.4	178.4	54.36
F63	8.393	118.4	177.7	61.83
G64	7.704	105.2	172.8	45.78
V65	6.899	118.5	176.3	63.90
H66	7.642	112.0	176.3	54.18

Table A.5: Solid-state chemical shift resonances (residues 1 to 66) of microcrystalline ϵ_{186}, form at pH 6.0. Crystallization conditions are reported in table 3.2. Terminal residues are not assigned.

ϵ_{186}, 1.3 mm rotor, pH 9.0				
Res.	$^{1}H^{N}$	^{15}N	^{13}CO	$^{13}C\alpha$
G67	8.267	111.1	174.1	46.45
I68	10.920	126.0	173.5	62.29
A69	7.769	127.2	178.3	50.71
D70	7.907	118.4	179.8	57.64
E71				59.05
F72	7.038	115.0		58.97
L73	6.920	115.3	177.2	54.24
L74	6.696	114.3	176.9	57.23
D75	7.652	115.1	175.8	52.01
K76	6.790	120.3	172.8	52.15
P77			175.9	61.61
T78	8.182	107.9	176.6	60.11
F79	9.472	122.0	177.3	62.29
A80	8.386	117.0	179.6	54.86
E81	7.501	115.1	177.2	58.00
V82	7.126	110.8	175.8	60.17
A83	7.515	124.1	178.1	55.93
D84	8.468	116.2	177.0	57.99
E85	8.114	120.9	179.3	59.17
F86	8.718	119.9	176.5	58.12
M87	8.663	118.2		60.05
D88	8.360	116.7	177.8	56.25
Y89	7.748	120.5	176.2	62.14
I90	7.335	108.5	175.8	62.15
R91	7.707	119.6	177.5	58.98
G92	8.764	113.7	172.8	45.14
A93	7.937	123.2	175.5	50.83
E94	7.659	119.0	174.7	54.00
L95	9.315	128.7	174.9	52.78
V96	8.931	125.2	174.5	61.42
I97	8.082	123.5	175.3	59.41
H98	9.286	130.5	175.2	
N99	7.927	123.8	172.4	53.83
A100	6.974	120.3	177.1	53.84
A101	8.332	116.3	181.0	54.61
F102	7.556	118.8	178.5	60.28
D103	8.444	121.1	177.8	57.75
I104	9.396	117.8	178.0	61.99
G105	7.719	104.9	175.0	46.95
F106	7.153	118.8	177.5	63.64
M107	8.737	118.8	175.5	59.81
D108	9.033	116.8	175.5	56.78
Y109	7.725	119.7	178.6	59.12
E110	8.148	120.6	180.7	59.15
F111	9.090	117.8	180.5	60.02
S112	8.437	118.8	177.4	61.51
L113	7.589	123.6	178.2	56.07
L114	7.331	114.6	177.0	54.85
K115	7.435	115.1	175.8	56.43
R116			175.1	54.55
D117	8.201	116.7	175.2	54.71
I118	7.531	119.3	174.9	60.11
P119			175.0	61.61
K120	8.127	116.4	178.3	56.53
T121	9.977	124.3	175.1	67.76
N122	8.867	116.3	175.5	53.71
T123	8.087	108.8	175.6	62.73
F124	7.318	116.2	174.1	55.98

Table A.6: Solid-state chemical shift resonances (residues 67 to 124) of microcrystalline ϵ_{186}, form at pH 6.0. Crystallization conditions are reported in table 3.1.

.

ϵ_{186}, 1.3 mm rotor, pH 9.0				
Res.	$^{1}H^{N}$	^{15}N	^{13}CO	$^{13}C\alpha$
C125	7.833	122.3	173.1	58.58
K126	7.761	121.4	174.9	55.11
V127	8.547	124.8	174.5	62.53
T128	9.713	129.9	171.2	61.45
D129	8.614	125.5	177.7	50.98
S130	9.256	122.1	177.1	62.05
L131	8.566	126.3	177.2	57.34
A132	6.697	122.3	181.1	54.56
V133	7.353	118.7	177.6	66.26
A134	8.025	122.2	178.2	55.55
R135	8.477	116.0	178.3	59.44
K136				
M137				
F138				
P139			176.2	62.84
G140	8.627	104.8		45.79
K141				
R142				
N143	7.306	116.7	175.9	54.57
S144	6.853	112.2		56.47
L145				
D146	8.141	116.0		56.62
A147	7.911	124.5		
L148	8.439	120.6		57.94
C149	8.307	117.7	177.2	63.82
A150	7.256	120.1	180.3	54.35
R151	8.535	118.6		59.21
Y152				
E153				
I154				
D155				
N156				
S157				
K158				
R159				
T160				
L161				
H162				
G163	7.696	105.0	173.5	46.37
A164				
L165	6.285	117.7	177.1	55.94
L166	8.363	120.0		57.21
D167	7.450	115.4	177.7	57.90
A168	8.065	121.6	178	54.98
Q169	7.855	119.6	177.6	59.05
I170	8.042	120.3	177.7	65.25
L171	8.341	119.6	178.4	56.87
A172	8.509	122.0	178.4	55.87
E173	7.070	115.1	179.8	59.03
V174	8.213	120.2	176.3	65.75
Y175	9.919	121.2	176.3	62.02
L176	8.279	120.4	178.9	57.10
A177	7.400	122.3	180.4	54.70
M178	8.360	118.6	178.2	58.73
T179	7.794	104.5		60.98
G180				

Table A.7: Solid-state chemical shift resonances (residues 125 to 186) of microcrystalline ϵ_{186}, form at pH 6.0. Crystallization condition are reported in table 3.1. Terminal residues not assigned.

.

Appendix B

List of Publications

Full papers in peer-reviewed journals

LAAGE Ségolène, MARCHETTI Alessandro, SEIN Julien, PIERATTELLI Roberta, SAAS J urgen, GRZESIEK Stefan, LESAGE Anne, PINTACUDA Guido, EMSLEY Lyndon
Band-Selective ^{1}H-^{13}C Cross-Polarization in Fast Magic Angle Spinning Solid-State NMR Spectroscopy.
J. Am. Chem. Soc, 2008, **130** : pp. 17216-17217

DOMENICI Valentina, MARCHETTI Alessandro, CIFELLI Mario, VERACINI Carlo Alberto
Dynamics of Partially Oriented L*-Phenylalanine-d_8 in the CsPFO/H_2O Lyotropic System via ^{2}H-NMR Relaxation Studies.*
Langmuir, 2009, **25** : pp. 13581-13590

MARCHETTI Alessandro, DOMENICI Valentina, NOVOTNA Vladimira, LELLI Moreno, CIFELLI Mario, LESAGE Anne, VERACINI Carlo Alberto
Direct Measure of the Tilt Angle in de Vries-Type liquid crystals through NMR Spectroscopy.
ChemPhysChem, 2010, **11** : pp. 1641-1645

BERTINI Ivano, EMSLEY Lyndon, FELLI Isabella C., LAAGE Ségolène, LESAGE Anne, LEWANDOWSKI Józef R., MARCHETTI Alessandro, PIERATTELLI Roberta, PINTACUDA Guido
High-Resolution and Sensitivity Through-Bond Correlations in Ultra-Fast Magic Angle Spinning (MAS) Solid-State NMR.
Chem. Sci., 2011, **3** : p. 345-348

DOMENICI Valentina, CIFELLI Mario, MARCHETTI Alessandro, LELLI Moreno, HAMPLOVA Vera, KASPAR Miroslav, VERACINI Carlo Alberto

SmA - SmC transition in a de Vries liquid crystals by ^{2}H-NMR.*
Mol. Cryst. Liq. Cryst., 2012, **553** : p. 1 - 8

MARCHETTI Alessandro, JEHLE Stefan, FELLETTI Michele, WANG Yao, XU Zhi-Qiang, OTTING Gottfried, EMSLEY Lyndon, LESAGE Anne, DIXON Nick, PINTACUDA Guido
Backbone NMR chemical shift assignment of fully protonated solid proteins by ^{1}H detection and ultra-fast magic-angle spinning
Submitted *Ang. Chem. Int. Ed.*

Oral communications

MARCHETTI Alessandro, DOMENICI Valentina, PELL Andrew James, LELLI Moreno, CIFELLI Mario, LESAGE Anne, VERACINI Carlo Alberto
New physical insights on de Vries smectic liquid crystals by means of ^{2}H-NMR and ^{13}C-NMR spectroscopy.
39th Conference of S.C.I. (Italian Chemical Society) - Division of Chemical Physics (Stresa, Italy), October 2010.

Posters

JEHLE Stefan, FELLETTI Michele, WANG Yao, MASON Claire, MARCHETTI Alessandro, EMSLEY Lyndon, DIXON Nick, LESAGE Anne, PINTACUDA Guido
Protein-Protein Interactions in the Bacterial Replisome Studied by Solid-State NMR.
53rd E. N. C. (Miami, Florida, U.S.A.), April 2012.

MARCHETTI Alessandro, LEWANDOWSKI Józef R., DUPEUX Florine, BLACKLEDGE Martin, PINTACUDA Guido, MARQUEZ José A., EMSLEY Lyndon
Solid-state NMR investigation of the hormone binding receptor PYR1.
52nd E. N. C. (Asilomar, California, U.S.A.), March 2011.

MARCHETTI Alessandro, LEWANDOWSKI Józef R., DUPEUX Florine, BLACKLEDGE Martin, PINTACUDA Guido, MARQUEZ José A., EMSLEY Lyndon
Solid-state NMR investigation of the hormone binding receptor PYR1.
Bio-NMR and EAST-NMR Annual User Meeting (Brno, Czech Republic), January 2011

MARCHETTI Alessandro, LEWANDOWSKI Józef R., BARBET-MASSIN Emeline, LESAGE Anne, PINTACUDA Guido, EMSLEY Lyndon
Large scale crystallization methods to address the bottleneck of sample availability in solid state NMR of proteins.

PCUBE Workshop, (Grenoble, France), September 2010.

MARCHETTI Alessandro, POINTOIZEAU Clément, LELLI Moreno, HERRMANN Torsten, LESAGE Anne, EMSLEY Lyndon, PINTACUDA Guido
Improved resolution in muldimensional Solid State NMR Spectra of protein through 2D projections of 3D spectra.
Euromar (2010, Florence, Italy), July 2010.

HERRMANN Torsten, GUERY Paul, LEWANDOWSKI Józef R., MARCHETTI Alessandro, LESAGE Anne, PINTACUDA Guido, EMSLEY Lyndon
Computational data analysis concepts for solid state NMR structure determination of protein and protein complexes.
6th Alpine Conference on Solid state NMR (Chamonix, France), September 2011.

Popularization (in Italian)

MARCHETTI Alessandro
Le immagini per la didattica e la divulgazione: ricerca on-line e copyright.
Images for didactics and popularisation: on-line search and copyright.
La Chimica nella Scuola, 2011, **Anno XXXIV** (1) : accepted
Abstract. *In the current "image society" we are living, oral or written communication is often enacted with the aide of suitable visual supports. Thanks to the advancement of digital photographic equipment, the new handy and customized image editing programs and the wealth of possibilities offered by the Internet, people make massive use of images in everyday's life. Despite this well-established reality and this diffuse know-how, the use of images for the drafting of an editorial product remains a more delicate matter, way more delicate than the their simple insertion in a public presentation or in some lecture notes. For semi-professional contributors, a basic knowledge of the on-line search engines, of the most important media databases and the main concepts of copyright should be desirable (and useful).*

MICHELI Marco, MARCHETTI Alessandro
Un normalista alle Hawaii
An SNS alumnus in Hawaii
Normale, 2011, **Anno XIV** (1-2) : pp. 26-32
Abstract. *The perspective of near-earth objects astronomic research as seen from Manua Kea.*

MARCHETTI Alessandro, DOMENICI Valentina
Il laboratorio scientifico come infrastruttura. Un fotoracconto esemplificativo.
The scientific laboratory as an infrastructure. An explanatory picture-history.

La Chimica nella Scuola, 2011, **Anno XXXIII** (5) : pp. 263 - 264

Abstract. *The concept of scientific laboratory as infrastructure or facility can be proposed to the students through a simple but satisfactory example: the installation of a new spectrometer for nuclear magnetic resonance spectroscopy, the 1GHz recently installed in Lyon, at the Centre RMN à Très Hauts Champs. Here, we propose a picture-history of the event.*

MARCHETTI Alessandro, DOMENICI Valentina

I cristalli liquidi: un'introduzione critica - Parte I e Parte II.

Liquid Crystals: a crytical introduction - Part I and Part II.

La Chimica nella Scuola, 2010, **Anno XXXII** (3) : pp. 131-141

La Chimica nella Scuola, 2011, **Anno XXXIII** (1) : pp. 3-17

Abstract. *In a very competitive world where the push for discovery of new and versatile liquid cristalline phases is a key target of basic and applied research, it is very important to provide a sound base on which to hierarchize all the aspects that can charcterize mesophases, discriminating microscopic aspects to macroscopic ones and understanding the limits of the models that describe them. Firstly, because oversimplified or phenomenological-based explanations can be hard to overcome in a deeper understanding of the subject, secondly, because these concepts are relevant also in the understanding and the modelisation of all the possible aggregated phases composing soft matter (colloids, foams, emulsions ...), i.e. most part of living beings world: the more critical way they are introduced, the more they can be extended to other fields in a versatile way.*

COBBE Alessandro, MARCHETTI Alessandro

Quanti colori servono per colorare una cartina geografica?

How many colors are necessary to draw a gepographic map?

Abstract. *The key concepts and early steps of graph theory are presented to high-school students.*

Normale , 2009, **Anno XIII** (1) : pp. 24-31.